COAXIALLY ELECTROSPUN HEPARIN-ELUTING SCAFFOLDS FOR VASCULAR GRAFT APPLICATION

Gerhard Jaco Krause

Submitted for the degree: MSc in Biomedical Engineering (Diss)

University of Cape Town

Department of Human Biology

Division of Biomedical Engineering

in association with

Cardiovascular Research Unit

and

Chris Barnard Division of Cardiothoracic Surgery

Supervisor: Prof Deon Bezuidenhout

February 2022

To my parents and grandparents.

Declaration

I, *Gerhard Jaco Krause*, hereby declare that the work on which this dissertation/thesis is based is my original work (except where acknowledgements indicate otherwise) and that neither the whole work nor any part of it has been, is being, or is to be submitted for another degree in this or any other university.

I empower the university to reproduce for the purpose of research either the whole or any portion of the contents in any manner whatsoever.

Signature: | Signed by candidate |

Date: 10 February 2022

Abstract

The use of electrospun scaffolds for small diameter vascular grafts (< 6 mm) has shown promise in the search for alternative solutions, as current synthetic grafts have high failure rates. The inclusion of heparin into such scaffolds can be beneficial for vascular graft applications as it could prevent mid-graft thrombosis, stabilise and potentiate growth factors as well as subdue undue proliferation of smooth muscle cells. Previous attempts at including heparin by chemical modification or inclusion into the bulk of the electrospun fibres (blend or emulsion electrospinning) were successful but resulted in burst release, reduced bioactivity and rapid elution of the heparin due to bulk degradation of the polymers. This project aimed to develop scaffolds comprising electrospun degradable polyurethane fibres with coaxially incorporated heparin sodium (HepNa$^+$) with improved release kinetics and heparin activity for application in the tissue engineering of blood vessel substitutes.

Scaffold sheets were cut from tubes (ID = 25 mm) produced on a rotating mandrel by coaxial, conventional and blend electrospinning of a degradable polyurethane, DegraPol® (DP30). Three coaxially electrospun groups were produced with DP30 (CHCl$_3$) shells and polyethylene oxide, PEO (H$_2$O/EtOH) cores containing either low (0.3 wt%), high (0.6 wt%) or no HepNa$^+$. Blend electrospinning was achieved by incorporating heparin (after modification to its tributylamine (TBA) salt for solubility) into DP30 solution (in CHCl$_3$). Lastly, a control group was produced by conventional electrospinning of DP30 (CHCl$_3$).

The morphological (fibre diameter, fibre orientation, pore size and porosity), mechanical (tensile stress and strain, suture retention) and thermal (glass transition, melting and crystallization temperature) properties of the scaffolds were characterised and the corresponding in vitro drug release (heparin quantification and activity) and degradation response over 6 weeks in PBS (37 °C) were determined. Subsequently, conditions were optimised in a pilot study to electrospun small diameter (ID = 2.6 mm) tubular grafts and their morphological and mechanical properties (hoop stress, burst pressure and compliance) were determined.

Coaxial electrospinning of DP30 with a water core and especially the addition of HepNa$^+$ resulted in a decrease in fibre diameter (40 %), OI (23 %), pore size (39 %) and porosity (20 %) (all P < 0.05), most likely due to increased conductivity and dielectric constant.

With one exception, there was no difference in the directional tensile properties between scaffold groups (ultimate tensile stress > 0.9 MPa, maximum strain > 100 %, suture retention > 2.4 N) or within groups between the longitudinal and circumferential tensile properties. After 6 weeks of in vitro degradation, all groups exhibited similar mechanical losses of approximately 40 % in ultimate tensile stress and 80 % in maximum elongation in circumferential and longitudinal directions. The smaller vascular grafts had burst pressures superior to native vasculature and compliances approximating those of healthy arteries.

Thermal analyses (DSC) of the different groups showed similar thermograms with little intergroup variation and indicated that the electrospinning process did not unduly affect the thermal properties or crystallinity, of DP30. There was also no major variations in thermograms of degraded samples.

Blend electrospun scaffolds showed the expected initial burst release of HepTBA (47.7 %, 3 days) followed by a sustained release (56.1 %, 6 weeks). Coaxially incorporated HepNa$^+$ also exhibited initial burst release (67.5-69.7 %, 3 days) for both the low and high heparin content groups followed by improved sustained release (81.9 - 97.7%, 6 weeks). Coaxial incorporation had a 2× higher heparin encapsulation efficiency than blend incorporation (approaching 100 %). Heparin, post-TBA-modification, did not fully retain its antithrombotic properties (54.9 % reduction), which was further reduced after incorporation and release (24.2 % reduction). HepNa$^+$, however, retained its full antithrombotic activity post coaxial incorporation and elution.

Coaxial electrospinning of heparin in DP30 shows potential for producing small diameter vascular grafts with mechanical properties comparable to small blood vessels. Although some initial burst release occurred, the sustained release over 6 weeks, incorporation of heparin without the need for modification at improved efficiency, and the retained activity of the heparin after electrospinning incorporation and elution; holds promise for vascular graft applications.

Future work should aim for the production of continuous cores within fibre morphology and evaluating graft performance in an in vivo model to determine whether an appropriate and sufficient amount of heparin has been included to affect the desired response.

Graphical abstract

Fibre cross sections

Conventionally electrospun **Blend electrospun** **Coaxially electrospun**

HepNa⁺
HepTBA
DegraPol® 30
PEO (400 kDa)

Morphological characterisation

- Scanning electron microscopy
  - Fibre diameter
  - Pore size
  - Orientation index
  - Core-shell validation
- Porosity

Polymer swelling

Cast DP30 film
Water

Vacular grafts (Pilot study

ID = 2.6 mm

Morphology Mechanical testing
- UTS, ε$_{max}$,E
- Compliance
- Burst pressure

DP30 Control *DP30/PEO/HepNa⁺ Coaxial*

Water contact angle

θ

Mechanical testing

- Ultimate tensile stress
- Maximum elongation
- Youngs modulus
- Suture retention strength

Differential scanning caliometery (DSC)

heat flow

temperature

T_g T_c T_m

- Samples
- Raw DP30, PEO, HepNa
- Quenched DP30

Degradation 6 Weeks (PBS @ 37°C)

PBS

Week 1, 2, 3, 6
- Mechanical loss
- Mass loss
- Thermal properties (DSC)

Drug elution – 6 Weeks (PBS @ 37°C)

Heparin quantification
Days 1-4, 7, 14, 21, 42
- MBTH assay

Heparin activity @ *Day 2*
- TEG®

Acknowledgements

Table of contents

List of abbreviations

ANOVA	analysis of variance
ANSI	American National Standards Institute
bpm	beats per minute
BSA	bovine serum albumin
CA	coronary artery
CAD	coronary artery disease
CABG	coronary artery bypass graft
CVD	cardiovascular disease
$CHCl_3$	chloroform
COL	collagen
DEX	dextran
DI	de-ionised
DSC	differential scanning calorimetry
DP	DegraPol®
CVD	cardiovascular disease
ePTFE	expanded polytetrafluoroethylene
EC	endothelial cell
ECM	extracellular matrix
EtOH	ethanol
FA	femoral artery
FE_3O_4	iron (II,III) oxide (/superparamagnetic magnetite)
G	gauge
GF	growth factor
HAEC	human aortic endothelial cell
$HepNa^+$	heparin sodium
HepTBA	heparin tributylamine
HFIP / HFP	hexafluoroisopropanol
HREC	Human Research Ethics Committee
HUVEC	human umbilical vein endothelial cell
ID	Inner diameter
IH	intimal hyperplasia
IMA	internal mammary artery
IT	isothermal
KH_2PO_4	monopotassium phosphate
LAD	left anterior descending
LB-ADSA	low-bond axisymmetric drop shape
LN2	liquid nitrogen
MBTH	3-methyl-2-benzothiazolinone hydrazone hydrochloride
MeOH	methanol
MSN	mesoporous silica nanoparticles

NaCl	sodium chloride
NaH$_2$PO$_4$	sodium dihydrogen phosphate
NMR	nuclear magnetic resonance
NS	not significant
OD	outer diameter
OI	orientation index
PA	popliteal artery
PA-6	polyamide-6
PAA	polyacrylic acid
PAD	peripheral artery disease
PBS	phosphate-buffered saline
PCL	polycaprolactone
PDGF-BB	platelet-derived growth factor-BB
PEG	polyethylene glycol
PEO	polyethylene oxide
PET	polyethylene terephthalate
PGA	poly(glycolic acid)
PLA	poly(lactic acid)
PLCL	poly(L-lactide-co-caprolactone)
PLGA	poly(lactide-co-glycolide)
P(LLA-CL)	poly(L-lactic acid-co-ε-caprolactone)
PTFE	polytetrafluoroethylene
PU	polyurethane
PVA	polyvinyl alcohol
PVP	polyvinylpyrrolidone
rH	relative humidity
Ros-Ca	rosuvastatin calcium
RPM	revolutions per minute
RSA	Republic of South Africa
RT	room temperature
SAB	Salvianolic Acid B
SD	Sprague Dawley
SEM	scanning electron microscope(/microscopy)
SMC	smooth muscle cells
SR	suture retention
SV	saphenous vein
TA	transanastomotic
TBA	tributylamine
TCD	tip-to-collector distance
TE	tissue engineering
TEG®	thromboelastograph(y)
TEM	transmission electron microscope
TERM	Tissue Engineering and Regenerative Medicine

TESA	tissue engineering by self assembly
TEVG	tissue engineered vascular graft
TFA	trifluoroacetic acid
TFE	2,2,2-trifluoroethanol
TM	transmural
TS	thermal scan
VEGF	vascular endothelial growth factor
VSMC	vascular smooth muscle cell
USA	United States of America
UTS	ultimate tensile stress
UV	ultraviolet
%wt/wt	weight-by-weight percentage

Sample group abbreviations

DP30CTRL	DP30 control, conventionally electrospun (ID = 25 mm)
HTBlend	0.6wt% HepTBA/DP30 blend electrospun (ID = 25 mm)
HiHepCA	high $HepNa^+$ content coaxially electrospun (ID = 25 mm)
LoHepCA	low $HepNa^+$ content coaxially electrospun (ID = 25 mm)
NoHepCA	no $HepNa^+$ content coaxially electrospun (ID = 25 mm)
DP30CVG	DP30 control, conventionally electrospun (ID = 2.6 mm)
HepCAVG	low HepNa+ containing coaxially electrospun (ID = 2.6 mm)

List of symbols

P	probability
n	sample size
K	TEG kinetic time
MA	TEG maximum amplitude
m	mass
F	force
P_i	internal pressure
R	TEG reaction time
C_e	entanglement concentration
C_0	solution concentration
C_d	diametral compliance
k	release constant
W	the amount of drug dissolved
V	volume
V	volumetric flow rate
$\bar{x}$	mean
ε_{max}	maximum elongation
σ	tensile stress
η	viscosity
ΔH	enthalpy change
r	radius
d	diameter
θ	Contact angle
°	degrees
$\omega_{rotational}$	mandrel rotational velocity
Φ	porosity
α	TEG angle

List of figures

List of tables

1 Introduction

This chapter provides background information on the demand for vascular graft solutions as interventions for vascular disease. The subsections cover a literature review on topics related to the development of tissue engineered scaffolds for vascular graft applications using synthetic and biomaterials as well as the incorporation of drugs into these scaffolds. It concludes with a research proposal stating the aims and objectives of the proposed study.

1.1 Background

1.1.1 Cardiovascular disease

Annually, cardiovascular disease (CVD) is responsible for 17.79 million mortalities worldwide [1]. This accounts for 31.8 % of all deaths, making it the number one cause of death globally. Even though CVD used to be considered a disease only of the wealthy western nations, it is increasingly affecting populations in emerging and developing economies due to the change in lifestyle and diet. Currently, 80 % of CVD related deaths occur in low- and middle-income countries [2]. South Africa demonstrates this change as more South Africans die from CVD than all cancers combined and a 41 % increase in the number of premature deaths caused by CVD is expected by 2030 [3, 4]. From a global standpoint, CVD creates a substantial economic burden. Europe is confronted with more than 11.3 million new cases of CVD per year and 3.9 million annual CVD related deaths (45 % of all death), bringing about €169 billion in healthcare costs [5, 6]. Moreover, in the USA, CVD prevalence is on the rise with more than 655,000 CVD related deaths per year and direct treatment costs of $213.8 billion, with more than 400,000 bypass surgeries performed annually [7].

CVD constitutes a broad range of pathological and structural disorders of the cardiovascular system i.e. the heart and blood vessels [8]. The most common CVDs are vascular diseases, rheumatic heart disease, cardiomyopathy and congenital heart disease [9]. Risk factors are amplified by the modern way of living such as prolonged working hours, increased stress levels, physical inactivity and smoking, therefore new and better treatment options are still of utmost importance as CVDs will remain a major problem in the future.

1.1.2 Vascular disease

Vascular diseases are brought about by abnormal vasculature caused by either (i) narrowing or obstruction of vessel lumens or (ii) weakening of the blood vessel walls [10]. The former can occur either progressively (e.g. by atherosclerosis) or suddenly (e.g. by embolism or thrombosis) while the latter leads to dilation, rupture or dissection. Diseases of the arteries are notably more prevalent compared to those of veins, which is ascribed to the fact that arteries have more variations among different parts of the vascular tree, leaving them more vulnerable to pathological and structural changes. Leading vascular diseases are cerebrovascular disease, coronary artery disease and peripheral artery disease. However, before delving into the particulars of specific vascular diseases, it is important to first understand the architecture and cellular composition of blood vessels.

1.1.2.1 Blood vessel anatomy

All blood vessels of the cardiovascular system are qualitatively similar but quantitive features differ with location and they reflect distinct location-specific required functions [10]. Arteries, for instance, usually have thicker walls compared to veins since they are subjected to higher blood pressures and must be able to endure pulsative flow, while veins (unlike arteries) in lower-extremities have valves to prevent reverse flow (with gravity) in venous return.

Blood vessels comprise of endothelial and smooth muscle cells and an extracellular matrix (ECM) composed of collagen (COL), elastin and glycosaminoglycans [11]. Blood vessels consist of three concentric layers i.e. the intima (inner), media (middle) and adventitia (outer), which are most distinguishable in larger blood vessels, especially in arteries [12]. In most healthy arteries, the intima constitutes of a monolayer of endothelial cells, the media constitutes of smooth muscle cell (SMC) layers and the adventitia constitutes of connective tissue and nerve fibres. The media is separated from the intima and adventitia by the internal and external elastic lamina (elastic membrane), respectively. The layers of SMCs of the media closest to the lumen are oxygenated and nourished via diffusion, while diffusion is insufficient for the outer layers and they are nourished by vasa vasorum, small arterioles that penetrate the adventitia and media from the abluminal side. The general architecture of blood vessels are illustrated in Figure 1.
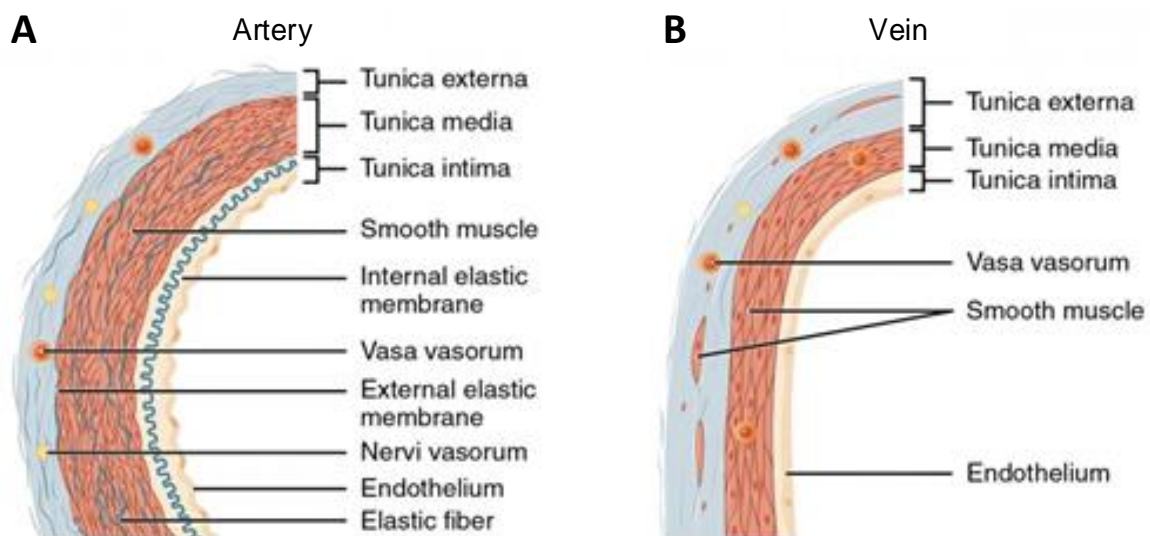
Figure 1: General architecture of an A) artery and B) vein [13].

Vital location-specific structural specialisations of arteries occur to meet the required need (pressure, flow, diffusion etc.) and variations are mainly found in the media with respect to the relative proportions of the cell types and ECM [10]. The media of large arteries (e.g. aorta) have abundant, well-arranged elastin to allow storing of energy during the expansion of the vessel wall enabling elastic recoil during diastole (causing blood flow), while the media of smaller muscular arteries such as coronary and renal arteries holds collagen and densely packed SMCs, with the media of further smaller branches and arterioles consisting of only SMCs to enable calibre adjustment (vasoconstriction and vasodilation) for regulating flow to capillary beds and the smallest branches i.e. capillaries having no media at all, optimising diffusion across the single endothelial cell layer.

<u>The role of the confluent endothelium</u>

The presence of an intact and functional monolayer of endothelial cells (ECs) covering the lumen of all blood vessels is of substantial importance as it, most importantly, maintains a non-thrombogenic interface between circulating blood and the blood vessel wall. Furthermore, ECs also play a role in blood flow and vascular resistance modulation, hormone metabolism, regulation of immune and inflammatory responses by preserving structural integrity; and the regulation of certain cell types' growth (especially SMCs) [14, 15]. ECs adapt to local and mechanical cues by modifying their fundamental functions and through inducing the expression of new properties. This can include expressing platelet adhesion molecules (procoagulants/anticoagulants), growth factors, histocompatibility complex molecules and production and release of chemokines and cytokines as well vasoreactive products (responsibly for vasoconstriction and vasodilation), to just name a few [10].

1.1.2.2 Atherosclerosis

Atherosclerosis, the most common vascular disease, used to be considered a cholesterol storage disease but is now defined as an inflammatory response of the arterial wall resulting from an injury to the endothelial layer which leads to thickening of the intimal layer, deposition of lipids, calcification and inflammation. It is distinguished by plaques – lesions protruding into and obstructing the lumen and weakening the underlying medial layer [16]. The plaque builds up through a collection of mural lipids, complex interaction with monocytes as well as inflammation [17, 18]. Even though atherosclerosis can develop in any artery, the disease development is augmented with dynamic flow conditions and disruptions (e.g. at bifurcations), therefore it usually occurs in elastic arteries such the carotid artery and the aorta; and in large- and medium-sized muscular arteries such as the popliteal and coronary arteries. The effects are however less severe for larger arteries due to the size of plaque compared to the calibre of the artery. As a result, coronary artery disease is the leading cause of atherosclerotic cardiovascular morbidity, followed by stroke and then lower-extremity peripheral artery disease [19].

1.1.2.3 Coronary artery disease

Coronary artery disease (CAD), also known as coronary heart disease, is caused by atherosclerosis or atherosclerotic occlusion of the coronary arteries and it can be chronic or acute [20]. This results in a supply-demand mismatch for heart muscles, impairing normal functionality which manifests as stable angina (chronic) or acutely as unstable angina or myocardial infarction caused by plaque rupture [21].

1.1.2.4 Peripheral artery disease

Peripheral artery disease (PAD) is a widespread arteriopathy that involves all medium and small arteries excluding the intracranial vessels and coronary arteries, generally resulting in sporadic claudication due to obstructed blood supply to lower limbs [22]. The femoropopliteal segment is the most intervened region for PAD. Even though PAD is an indication of diffuse arteriopathy and usually accompanies coronary artery disease, it seldomly results in death. Therefore, interventions are centred around pain relief and improving quality of life, but in severe cases, limb amputation might be required [23].

1.1.2.5 Interventions

A wide variety of effective treatments for these vascular diseases exist such as changes in lifestyle- and dietary habits, administration of chronic and/or acute pharmaceutics (e.g. anticoagulants and beta-blockers), as well as surgical interventions. Vascular surgical approaches include endovascular methods like balloon angioplasty, stent insertion and atherectomy [24]. Angioplasty (Figure 2A) is a procedure where a balloon, guided by a wire to the site of narrowing, is inflated to flatten the plaque against the wall of the artery, opening the lumen and restoring blood flow. This is normally followed by the insertion of a stent (plastic or metal) to ensure that the artery remains open (Figure 2B). Atherectomy takes a different approach and aims to remove the plaque from the artery by shaving or vaporising it away with minuscule rotating blades or a laser placed on a catheter tip [25]. In situations of severe disease progression where the abovementioned approaches deem insufficient, the damaged or occluded blood vessels are replaced or bypassed using vascular grafts (Figure 2C) [26, 27]. Coronary artery bypass grafting (CABG) is suggested for triple-vessel coronary artery disease, double-vessel coronary artery disease with proximal left anterior descending (LAD) stenosis and survivors of sudden cardiac death that is presumed to be ischemia related [28].
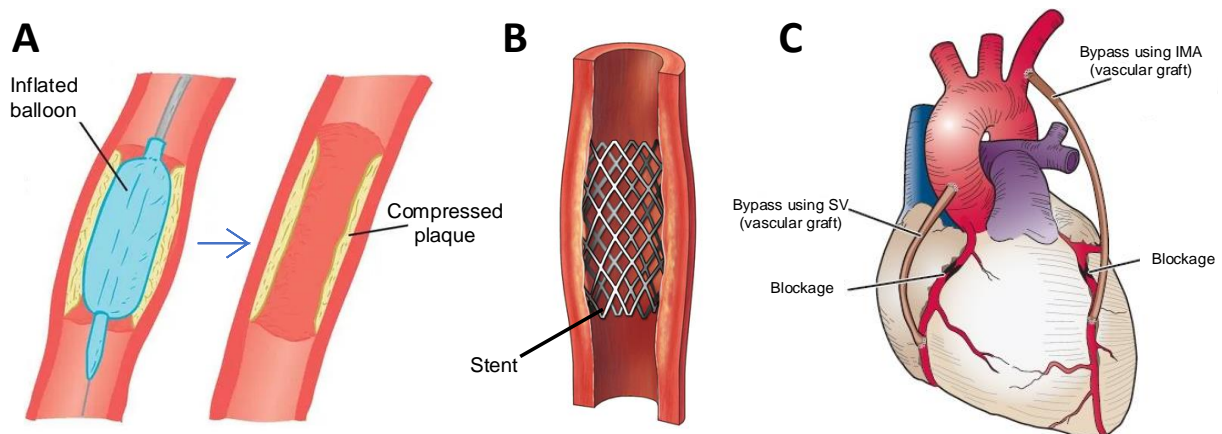
Figure 2: Vascular disease interventions. A) Balloon angioplasty [29]. B) Stent insertion [30]. C) Vascular graft – internal mammary artery (IMA) & saphenous veins (SV) for CABG [31].

1.1.3 A short discourse on vascular grafts

The demand for vascular grafts is increasing, with the global market expecting an annual growth rate of 6.4 % from 2019 to 2026 [32]. A vascular graft is used to replace or bypass an arterial or venous segment that is incapable of transporting sufficient oxygenated blood to the tissue surrounding it. This can be due to trauma, congenital malformation or, as discussed above, diseased vessels (mainly as a result of atherosclerosis) that lead to stenosis or occlusion [33]. Large- and medium-diameter grafts (> 6 mm) are utilised in thoracic and abdominal cavities while small-diameter grafts (< 6 mm) are mainly used for coronary artery bypass grafting (CABG), vascular access and lower-limb ischemia relief [34]. Current artificial prostheses provide good long-term outcomes in large- and medium-diameter applications but small-diameter grafts, however, have high 5-year failure rates [35].

Grafts may be classified into (i) bioprosthetic, (ii) synthetic, (iii) in vitro tissue engineered and (iv) in vivo tissue engineered grafts [36-38].

1.1.3.1 Bioprosthetic vascular grafts

Bioprosthetic vascular grafts are of biological origin and include autografts, allografts and xenografts.

Autografts, autologous (patients' own) arteries and veins, are the current gold standard for the replacement of damaged small-diameter blood vessels [39]. Autologous saphenous veins (SV) are the conduit of choice to replace or bypass femoral/popliteal arteries, yet in approximately 20-30 % of patients, these are unavailable (compromised) due to previous harvesting or PAD, in which case synthetic grafts are used which, as will be discussed later, often fail [37, 38, 40]. On the other hand, autologous arteries (radial or internal mammary) and veins (saphenous) are not only preferred but exclusively used in the case of CABG [41]. Even though the internal mammary artery is approximately 90 % patent at 10 years postoperatively, it is reserved only for bypassing the LAD artery, leaving the SV as the most frequently used conduit for lateral and posterior wall revascularization [10, 22]. Therefore, the major concerns regarding the use of autologous grafts are the low long-term patency rates of some vessels (especially the SV) and the limited availability of usable (non-diseased) vessels while sparing some harvestable vasculature for potential future use.

Allografts, also known as homografts or homologous grafts, are arteries and veins of human origin other than the receiving patient and are one of the oldest vascular graft solutions. Even though Carrel and Guthrie demonstrated that homologous and heterologous arteries and veins can serve as arterial grafts in animal models, more than 40 years passed before the first human implantation [42, 43]. In 1948, Gross et al. used segments of arteries acquired from recently deceased humans as aortopulmonary shunts [44]. In 1951, Kunlin was the first to utilise the SV as a bypass graft [45]. In 1952, Duborst et al. replaced an abdominal aorta with an arterial allograft (thoracic aorta of a 20-year-old female) [46]. But as more studies using allografts were performed, it became evident that the clinical need for vascular grafts far outweighed the availability of allografts as researchers realised that donors needed to be young and not have died from arteriopathies or infections. Moreover, allografts were unable to provide the desired durability and grafts failed frequently due to aneurysms, resulting in a loss of interest among scholars for this as a feasible solution.

Xenografts (heterologous/xenogeneic grafts) are arteries and veins of non-human biological origin. Although the concept of xenotransplantation has been investigated for more than 300 years, xenografts were only widely introduced in the 1970s, the most common being bovine carotid artery used in lower extremity revascularization [47, 48]. Significant superiority over other solutions have not been shown but xenografts do present promising advantages for use in infected spaces [49, 50]. Major obstacles include high immunogenicity resulting in infection and inflammation. Modifications through cross-linking of collagen, in an attempt to reduce antigenicity, which inherently increases degradation, results in poor clinical outcomes [51]. Currently, the only commercially available valved xenograft is the Contegra® bovine jugular graft marketed by Medtronic Inc which is widely used as the substitute for the right ventricular outflow (RVOT) in congenital cardiac surgery [52].

1.1.3.2 Synthetic vascular grafts

In 1952, Voorhees et al. successfully used synthetic cloth, Vinyon-N tubes, as arterial grafts for canine aortas and shortly thereafter, in 1954, implanted the grafts into 18 patients [53, 54]. Afterwards, interest grew exponentially with numerous research groups determined to develop textiles for synthetic grafts, but all failed due to poor mechanical properties. That was until the introduction of PET and PTFE in this application – two crystalline hydrophobic materials with superior bio-durability. They have dominated the market ever since.

Polyethylene terephthalate (PET), a linear semi-crystalline polyester, was developed by J.T. Dickinson and J.R. Whinfield and patented in 1950 by DuPont as **Dacron®** [22, 51, 55]. After several refinements, these grafts are today's standard for intervention in large diameter vessel applications [56, 57]. Currently, Dacron® grafts are fabricated in either woven (Figure 3A) or knitted (Figure 3B) forms and recent attempts at making these grafts more biocompatible include heparin coating and porosity enhancement [10, 58].

Polytetrafluoroethylene (PTFE), a non-biodegradable fluorocarbon polymer, was accidentally discovered by Dr Roy Plunckett in 1945 and marketed by DuPont as Teflon® [22, 59, 60]. W.L. Gore & Associates developed the expanded version, **ePTFE**, which is currently the synthetic graft most frequently used for bypassing small diameter vessels (arteriovenous, coronary and lower-extremity) which has mostly remained unchanged since first being documented for use in human circulation in 1972 [60, 61]. These synthetic vascular grafts (Figure 3C) generally achieve low pantencies of less than 50 % after 5 years [10].
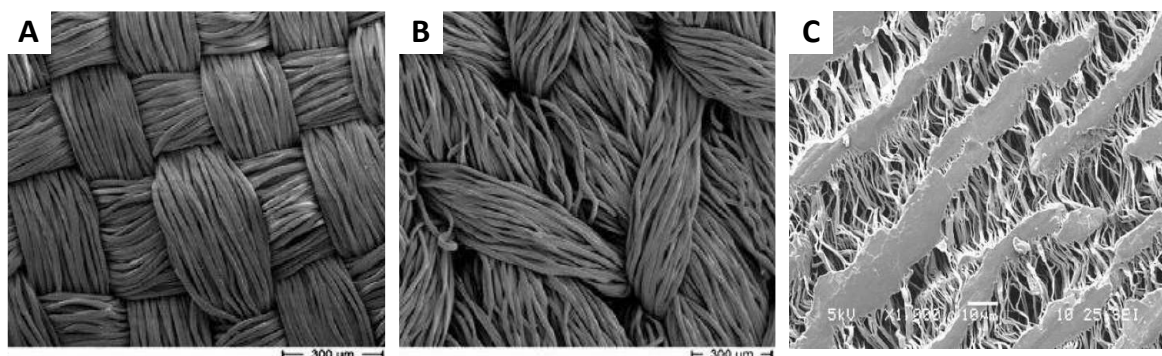
Figure 3: Scanning electron microscope images of synthetic vascular grafts. A) Woven and B) knitted PET [62]. C) ePTFE [63].

In general, Dacron and ePTFE have lower patency rates than autologous grafts, irrespective of the site of implantation, with neither of the synthetic materials showing any evidence of an advantage over the other [64-68]. The general opinion is that the probable underlying reason for failure in these grafts is their non-compliant nature which results in unusually high stresses at the anastomosis of the graft and the more compliant blood vessel i.e. compliance mismatch [66, 69].

The relatively poor performance of currently available synthetic grafts and the limited availability of autologous grafts have brought about the search for alternative materials and structures [70]. Among these are **polyurethanes (PUs)**, elastic polymers with a urethane [-NH-(CO)-O-] group and this polymer family has some of the highest elasticities among existing polymers [71]. In the 1980s, PUs became popular as a possible synthetic material for

vascular reconstruction and despite being used extensively in the medical devices field today, it has not gained much commercial interest in use as vascular grafts due to structural failure [22, 72]. Many researchers however still focus on the potential use of PUs due to the improved compliance and elasticity they present as well as their ability to be moulded or manipulated into a desired shape with interconnected pores and permeability [66, 73, 74].

1.1.3.3 Tissue engineering of vascular grafts

The first account of tissue engineered vascular grafts (TEVG) was documented by Weinberg and Bell in the 1980s, who fabricated blood vessels by seeding cells (bovine ECs and fibroblasts) on thin Dacron and collagen mesh scaffolds [75]. The concept of tissue engineering for tissue repair and replacement was however only introduced by Langer and Vacanti in the 1990s [76, 77]. The discipline of Tissue Engineering and Regenerative Medicine (TERM) originated from the realisation that implanted materials should positively interact with the body rather than formerly focusing on impossible to attain inertness [78]. Tissue engineering (TE) of vascular grafts entails the growing of living vessels, either by using cells/tissue alone or by using a combination of synthetic materials in combination with living cells/tissue and may be performed in vitro or in vivo [76].

For *in vitro* TE (Figure 4A) the patient's own cells (usually stem cells) are harvested, cultured and seeded onto or moulded into a scaffold prior to implantation and matured outside the body, typically within a bioreactor [79]. *In vivo* TE (Figure 4B) entails graft scaffolds that are directly implanted into the patient, that are designed to prompt graft regeneration and cell proliferation within the body, resulting in the formation of a neo-artery with full morphologic, functional, growth and remodelling properties [22, 80].
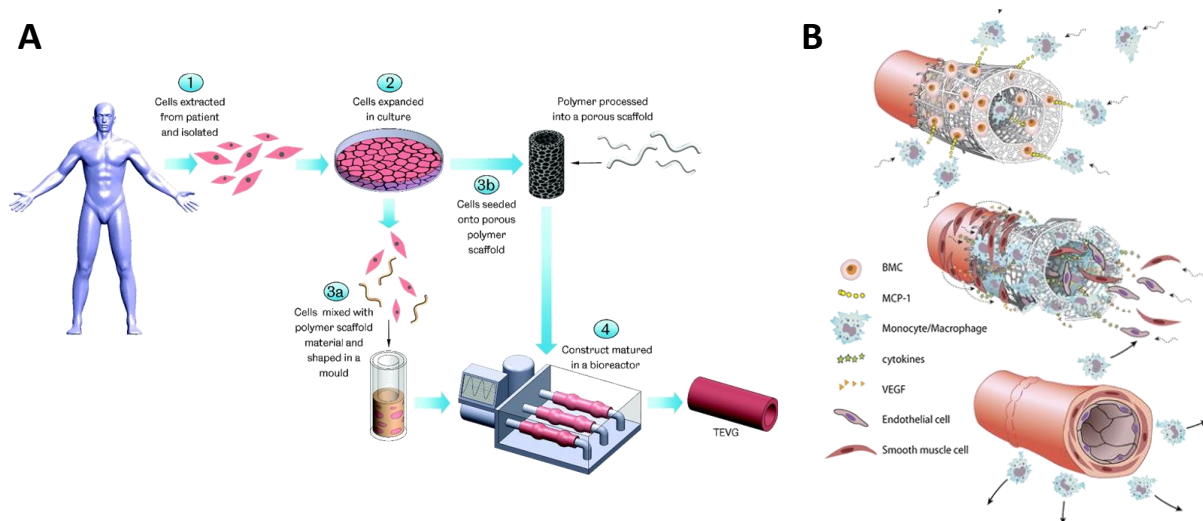
Figure 4: Tissue engineering of blood vessels. A) In vitro approach [27]. B) In vivo approach [81].

One of the major drawbacks of the in vitro approach limiting its application is the long lead times and high cost required to grow and manipulate cells harvested from the graft recipient [79]. Therefore, a strong case can be made for the in vivo tissue engineering or regenerative approach, where a ready-to-use graft scaffold (available "off-the-shelf") is immediately capable of re-establishing blood flow and contains the signals required for healing that will result in the formation of a neo-artery providing long-term patency [22].

1.1.3.4 TEVG development approaches

Various approaches have been utilised to fabricate vascular grafts. According to Walpoth et al., these methods for producing in vivo TEVGs can be clustered into five groups [82]:

Synthetic/natural scaffolds made from biodegradable or non-biodegradable synthetic and/or natural polymers can be implanted directly into the host as a vascular graft and promote the in vivo remodelling of the scaffold via endogenous cell recruitment and ECM deposition [83, 84]. A broad range of fabrication techniques is used to produce the types of scaffolds such as electrospinning, 3D bioprinting, polymer casting [85, 86].

Dellularisation of allogenic or xenogenic arteries/veins leave behind matrixes that serve as scaffolds that elicit in vivo remodelling [87, 88]. This method however frequently gives rise to recurrent immune responses (due to foreign-body rejection) and aneurysm formation is also evident due to the late degradation of these grafts [89, 90].

Autologous mandril-based vascular grafts is a novel approach to synthesise a vascular graft by subcutaneously implanting a compact rod which prompts a foreign body reaction leading to the development of connective tissue covering the rod, which is then removed and serves as an autologous cylindrical vascular graft [91-93].

Tissue engineering by self-assembly (TESA) entails using cell sheets to produce vascular grafts with vessel walls that consist of both polymers and stem, allogeneic or autologous cells [94-96]. This can alternatively be attained by 3D bioprinting and these vascular grafts are typically matured within bioreactors prior to implantation. The motivation behind this architecture is to produce different cell layers mimicking the native structure of blood vessels.

Decellularised bioreactor engineered vessels can be fabricated by combining the idea of synthetic/natural scaffolds and decellularisation. A neo-artery is fabricated in a bioreactor through human cells seeded on a fast degrading scaffold and once matured, it is completely decellularised [70, 97-99]. This construct is implanted as an acellular human vessel.

1.1.3.5 Vascular graft requirements

A graft suitable for implantation should, amongst other things, prove adequate compliance, burst pressure, suture retention strength and stress-strain response [26, 27, 100]. Native vasculature such as the internal mammary artery and saphenous vein is commonly used as design targets to establish whether these criteria are met [27]. Table 1 summarised the mechanical properties documented for human vasculature including the saphenous vein (SV), internal mammary artery (IMA), coronary artery (CA), femoral artery (FA) and popliteal artery (PA). To date, no research group has succeeded in achieving this goal together with appropriate in vivo graft remodelling and hemodynamics [27].

A vascular graft must have dimensions suitable for its intended purpose. According to a study by Van Andel et al., the external diameter of a human CA and IMA is 3.54±0.51 mm and 3.28 ±0.07 mm with respective wall thicknesses of 0.89±0.21 mm and 0.71±0.06 mm [101]. Another study recorded a thinner wall thickness for CAs of 0.32±0.06 mm (left anterior descending artery) and a wall thickness of 0.53±0.05 mm for the human radial artery [102]. Human saphenous veins have wall thicknesses of approximately 0.25 mm [103, 104].

Table 1: Mechanical properties of native vasculature.

Human vessel	UTS (MPa)	Elongation at failure (%)	Youngs Modulus (MPa)	Suture retention strength (N)	Burst pressure (mmHg)	Compliance (%/100 mmHg, unless stated as %/mmHg)
SV (circ.)	1.8±0.8 [105] 3.01±1.91[106]	242±89 [105] 11±5 [106]	4.2±3.3 [105] 42.6±27.8 [106]	1.92±0.02 [107] 1.92 [27]	1680-3900 [105] 3905- 4887[108] 1680±307 [94] 1680–2273 [107] 2134 [27]	0.7–1.5 [109] 0.7–1.5 %/mmHg [107] 25.6 [27] 4.2±0.4 [51]
SV (long.)	6.3±4.0 [105] 13.22±5.73 [106]	83±19 [105] 17±10 [106]	23.7±15 [105] 130.2±56.4 [106]			
IMA (circ.)	4.1±0.9 [105]	134±28 [105]	8.0±3.0 [105]	1.72 [27]	2000 [105] 3196 [110] 3073 [27]	11.5% [27]
IMA (long.)	4.3±1.8 [105]	59±15 [105]	16.8±7.1 [105]			
Arteries (general)	-	-	-	1.96±1.7 [107]	2,031–4,225 [107]	4.5–6.2 %/mmHg [107]
FA (circ.)	1-2 [40]	63-76 [40] 155 [111]	9-12 [40]	-	-	-
FA & PA	-	-	-	-	-	12 [112]
CA (circ.)	0.39±0.07 [113] 0.45±0.19 [114]	-	-	-	-	-

SV: saphenous vein, IMA: internal mammary artery, FA: femoral artery, PA: popliteal artery, CA: coronary artery.

Ideally, the remodelling/regeneration speed of the graft in vivo must be equal to the speed of polymer degradation to ensure that the graft always provides sufficient mechanical support [82, 115]. Furthermore, grafts must have sufficient porosity and large enough pore sizes to allow cell infiltration and an appropriate surface area for cell adhesion with the required amount of leakage without causing haemorrhage [115].

There are three possible sources for the development of an endothelium (EC lining) on the blood-contacting surface of a vascular graft implanted in vivo: 1) *transanastomotic* – overgrowth across the anastomotic sites from the host vessel, 2) *transmural* – ingrowth of fibrovascular elements through sufficiently large interstices permit from the inside to the outside of the graft allowing migration of ECs to the luminal surface, and 3) *fall-out* – deposition of multipotential stem cells and/or functional ECs from circulating blood [10]. Even though studies using animal models are able to attain a confluent endothelium through transanastomotic endothelilialisation alone, research indicates that in humans, endothelialisation from the adjacent vessel is limited to approximately 10-15 mm from the point of anastomosis [10]. Therefore it is critical for a vascular graft to allow transmural (TM) endothelialisation to meet the clinical need for human use [80].

1.1.3.6 Reasons for graft failure

The two main reasons for failure of artificial blood vessel substitutes are anastomotic intimal hyperplasia (IH) and mid-graft thrombosis. Anastomotic IH (Figure 5A) is a thickening of the tunica intima layer of the blood vessel due to excessive proliferation of SMCs [80]. Mid-graft thrombosis (Figure 5B) is the build-up of plaque along the graft wall resulting in the formation of blood clots [100]. Another indirect cause of failure is improper endothelialisation (Figure 5C) caused by insufficient pore sizes and the absence of cell-binding sites, preventing complete regeneration of the graft [27, 116].
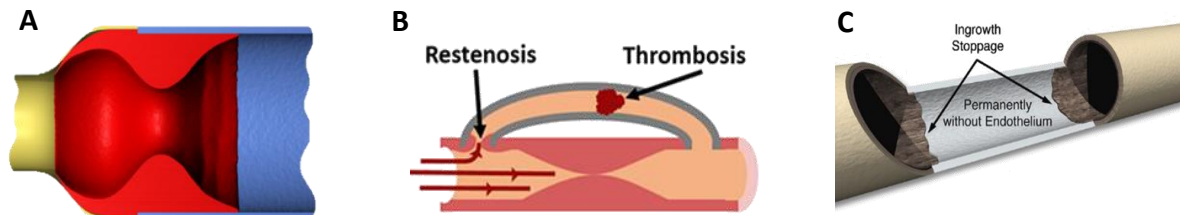
Figure 5: Reasons for vascular graft failure. A) Intimal hyperplasia [80]. B) Midgraft-thrombosis [117]. C) Improper endothelialisation [80].

1.2 Electrospinning

Electrospinning is a versatile technique for the production of tissue engineering scaffolds where fibres are made from polymers [118]. The electrospinning process offers many advantages for the production of fibrous scaffolds for biomedical use compared to other manufacturing processes. It is cost-effective, straightforward, efficient and allows for control of fibre morphology and diameter ranging from nanometer to micrometer scale [119-121]. Moreover, it enables synthesising porous scaffolds, with similarity to the ECM, that can facilitate cell adhesion and tissue ingrowth and it also allows drug incorporation into the scaffolds for controlled release [115, 122-124].

1.2.1 Overview of the electrospinning process

Electrospinning, first patented in 1902 by John Francis Cooley, is a spinning process that uses electrostatic force to draw fibres (µm to nm scale) from a liquid polymer solution or polymer melt [125]. The polymer solution is fed through a needle, used as a spinneret, and the produced fibres are deposited onto a collector as illustrated in Figure 6A. A voltage (in the range of kVs) is applied to the needle resulting in an accumulation of electric charge on the free surface of the solution within the needle and once the solution reaches the same polarity, electrical repulsion occurs [126]. Once the force of electrical repulsion exceeds the surface tension of the droplet formed at the needle tip, a Taylor cone (the initiating drop, Figure 6B) is formed and a liquid jet is ejected from the needle [127]. The ejected fibre will pass through different stages, starting with a straight jet stage and subsequently progressing into a whipping cone stage of bending instability, causing random deposition of the fibres. During the electrospinning process, the solvent evaporates and Coulombic forces exerted on the jet causes it to stretch until collected [128].
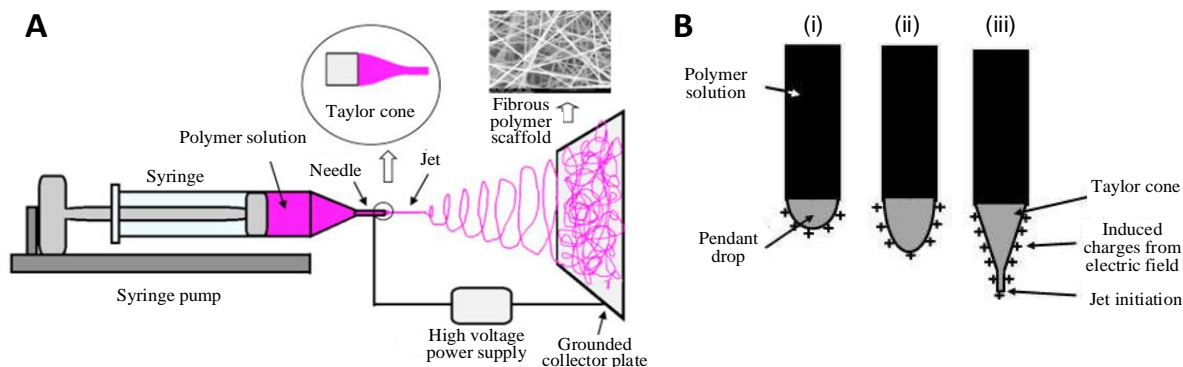
Figure 6: A) Electrospinning setup [129]. B) Taylor cone formation [130] - (i) The electric field induces surface charges in the polymer solution. (ii) Elongation of the pendant drop. (iii) Deformation of the pendant drop to the shape of the Taylor cone due to the charge-charge repulsion and a fine jet initiates from the cone.

In 1971, Baumgarten showed that the shape of the Taylor cone changes with spinning conditions such as viscosity, voltage and feed rate [131]. Since then it has become evident that several parameters influence the electrospinning process and that the morphology and diameter of fibres can be controlled by manipulating these parameters [132]. They can be grouped as the solution, processing and environmental parameters.

1.2.1.1 Solution parameters

Molecular weight

The molecular weight of a polymer mirrors the number of entanglements of the polymer chains in a solution and therefore also reflects the viscosity. It strongly affects electrical and rheological properties such as conductivity, dielectric strength, surface tension, and as mentioned, viscosity which all, in turn, influences fibre morphology [133]. Too low molecular weight results in bead formation, while higher molecular weight tends to produce larger fibre diameters. Tan et al. found that while electrospinning with a low concentration of HM-PLLA (high molecular weight poly-L-lactic acid) it is still possible to maintain a continuous jet resulting in uniform fibres if the molecular weight is high enough to ensure enough entanglement despite the low concentration [134]. On the contrary, it has been established that high molecular weight is not a prerequisite for successful electrospinning as adequate intermolecular interactions can substitute for the interchain connectivity provided by chain entanglements [135].

Concentration

A minimum concentration of polymer in a solution is required for fibres to form during electrospinning because if the concentration is too low, electrospinning results in a mixture of beads and fibres [136]. Increasing the solution concentration changes the beads' shape from spherical to spindle-shaped and finally removes beading completely, resulting in uniform fibres with increasing diameters (due to higher viscosity resistance), while too high concentrations inhibit the sustained flow of the solution at the needle tip which prohibits continuous fibre formation [133, 137-140]. A power-law relationship has been defined to describe the relationship between solution concentration and fibre diameter as it was found that for gelatin, increased concentration resulted in increased fibre diameters [141]. The concentration is closely tied to the surface tension and viscosity of the solution which also determines continuous fibre formation [137].

Viscosity

Viscosity is closely related to polymer concentration and molecular weight and is a critical parameter for controlling fibre morphology and size. Very low viscosities inhibit the continuous production of fibres (resulting in drop formation or beading) while very high viscosities reduce the ease at which the polymer jet is ejected. An optimal viscosity range, therefore, exists for successful electrospinning, but this range is polymer specific, with viscosities ranging anywhere from 0.1 to 215 P (Poise) documented in past research [142-144]. Polymer solutions with very high viscosity tend to exhibit longer stress relaxation times, avoiding jet fracture and larger, more uniform fibre diameters are observed with an increase in viscosity [137]. A polymer solution can generally be electrospun when the concentration exceeds the entanglement concentration, C_e.

Solution surface tension

The surface tension fulfils a vital role in electrospinning and is predominantly dependent on the solvent components with different solvents influencing surface tension uniquely. Hohman et al. established that beading can be avoided via a reduction of the solution's surface tension as high surface tension leads to jet instability and tends to result in electrospraying of droplets [145]. Lower surface tension also aids in successful electrospinning at lower electric fields [133].

Solution conductivity/ surface charge density

Most polymers are conductive materials (with a minority being dielectric) [136]. Jet formation during electrospinning is greatly influenced by the charged ions of the polymer solution. The type of polymer and solvents used, along with the availability of ionisable salts, determine the electrical conductivity of a solution. Initially, it was observed that an increase in a solution's electrical conductivity resulted in a noteworthy decrease in fibre diameter, with the smallest fibres, generally attained from solutions with the highest electrical conductivity [131, 143]. Further investigation confirmed that the jet radius was inversely proportional to the cube root of a solution's electrical conductivity [136, 143, 146, 147].

Researchers have struggled to yield uniform fibres from solutions with low electrical conductivity due to inadequate electrical forces resulting in insufficient jet elongation, whereas solutions with very high electrical conductivity are extremely unstable in the presence of strong electric fields, resulting in excessive bend instability and irregular fibre diameters [148]. Natural polymers (e.g. gelatin) are usually polyelectrolytic (they have less ability to form fibres) than synthetic polymers because they are subjected to higher tension in an applied electric field since the ions increase the jet's charge carrying capacity. It was established that the addition of ionic salts (such as NaCl, KH_2PO_4 and NaH_2PO_4) to natural polymers increased the electrical conductivity which resulted in more uniform fibres and the absence of beads [149].

Solvent properties

The type of solvent chosen for a polymeric solution greatly influences the electrical and physical properties of the solution [150]. The solvent should be capable of completely dissolving the polymer, creating a homogenous solution and should also present a moderate volatility and boiling point [59, 147, 151]. Ideally, the solvent should evaporate completely from the jet during movement from the needle to the collector, i.e. the solvent volatility should match the jet travelling time. A highly volatile solvent possesses a low boiling point

and so the solvent might dry at the needle, clogging the tip [150]. On the other hand, non-volatile solvents result in insufficient evaporation, causing fibres to land before completely dry and fuse together or bead [152, 153].

The dielectric constant of a solvent strongly influences the available 'free' charge in the solution which determines the onset of the bending instability [154, 155]. It directly affects the degree of whipping experienced during electrospinning, with solutions with solvents of high dielectric constants producing smaller, dryer and more randomly oriented fibres due to increased jet whipping and instability [136, 151]. Solutions containing solvents with higher dielectric constants also require lower applied voltages to acquire a Taylor cone compared to lower dielectric constants.

1.2.1.2   Processing parameters

<u>Applied voltage</u>

The voltage applied to the solution is one of the most important and controllable processing parameters in electrospinning [137]. The applied voltage controls the electric field strength between the needle and collector and therefore also the drawing force strength [150]. Fibre formation will only commence once the applied voltage has reached a threshold voltage, inducing enough charge on the solution to pull it along the electric field. Although some studies show no relation between applied voltage and fibre diameter [136], numerous accounts have been recorded of higher applied voltages resulting in reduced fibre diameters due to increased electrostatic repulsive forces on the ejected jet, also causing solvents to evaporate faster and reducing bead formation [152, 156-158].

<u>Solution flow rate</u>

The rate at which the polymer solution flows out of the needle (typically from a syringe) directly impacts the material transfer rate, as well as the velocity of the jet [127, 159]. Lower flow rates are beneficial as they provide sufficient time for the solvent to evaporate but a minimum flow rate is however required to ensure continuous jet formation. A study investigating the role of flow rate in the electrospinning of polystyrene fibres established that the fibre morphology can be altered by changing the flow rate since increased flow resulted in larger fibres and increased pore diameters [160]. Other studies have shown that high flow rates induced beading and wet landing as there was insufficient drying of the jets before landing [147, 161].

<u>Collector type</u>

The collector serves as a conductive substrate where the fibres deposit and the type of collector used is another easily controlled process parameter [159]. Over the past few decades, the range of collector types used has evolved significantly from flat aluminium foil (which used to be the standard) to conductive cloths, conductive paper, grided or parallel bars, rotating mandrels or wheels, wire meshes and liquid non-solvent coagulation baths to just name a few [136, 162, 163]. The use of less conductive collectors negatively influences fibre collection, while collectors with small deposition areas can result in fused and beaded fibres. Under normal conditions, fibres are randomly distributed onto the collector because of the instability of the highly charged jet but numerous research groups found that the alignment of fibres can be altered to be more parallel or more random by using a rotating collector and altering the rotational speed [127, 137]. Split electrodes have also been used at the collector to align fibres [164, 165].

<u>Tip-to-collector distance (TCD)</u>

The distance between the needle tip and the collector also affects fibre morphology and diameter during electrospinning. A minimum distance is required to give the ejected jet enough time to dry or else beads and wet landing would be observed [141]. Several studies have found that the effect of TCD is not as significant as other parameters but shorter distances tended to result in flatter fibres while further distances yielded rounder fibres for certain polymers and smaller diameters for others (e.g. polysulfone) [141, 147, 166, 167]. The optimal TCD for a specific solution should therefore favour the evaporation rate of the solvent to ensure dryness of the fibres.

1.2.1.3   Environmental parameters

Environmental (also referred to as ambient) parameters include the temperature and humidity at which electrospinning is conducted and has a major influence on the jet formation and fibre morphology [136].

<u>Temperature</u>

Solvent volatility and evaporation are closely linked to temperature and moreover, temperature affects the surface tension and viscosity of polymeric solutions [168, 169]. A temperature increase is known to result in both an increased solvent evaporation rate and a decrease in viscosity, which in turn leads to reduced fibre diameters [169-171].

<u>Humidity</u>

Humidity has a direct impact on fibre morphology. Numerous studies have documented that increasing humidity results in the formation of pores on the surface of fibres [172-175]. Humidity also influences fibre diameter with some researchers observing an increase in fibre diameter (cellulose acetate) with increased humidity, while others observed a decrease in fibre diameter (PVP) [59, 176, 177]. The needle tip may clog during electrospinning if the humidity is very low when a highly volatile solvent is used [150]. It was also found that high humidities may aid in the discharge of fibres, while others showed that above a certain threshold, proper fibre formation is inhibited [178, 179].

1.2.2   Coaxial electrospinning

Coaxial electrospinning was first introduced in 2002 [180]. This process entails electrospinning with a needle (core) placed (typically concentrically) within a larger needle (shell), each fed with their own polymer solution, which enables the fabrication of a distinct core-shell nanofibre structure as depicted in Figure 7A. The produced fibres are suitable for a wider range of applications as more diverse morphologies with multiple polymer solutions are allowed. Therefore, coaxial electrospinning has been adopted by the biomedical (e.g. drug release), environmental and electrochemical (energy harvesting) fields.

A core-shell interface is present since a shear force caused by contact friction and viscous dragging is produced between the core solution and the shell solution [181]. This shear force at the core-shell interface enables the core solution to be entrained in the compound jet (Figure 7B) and stable core-shell fibres are formed when the surface tension at the interface is overcome by the shear stress caused by the shell solution's viscosity [128].
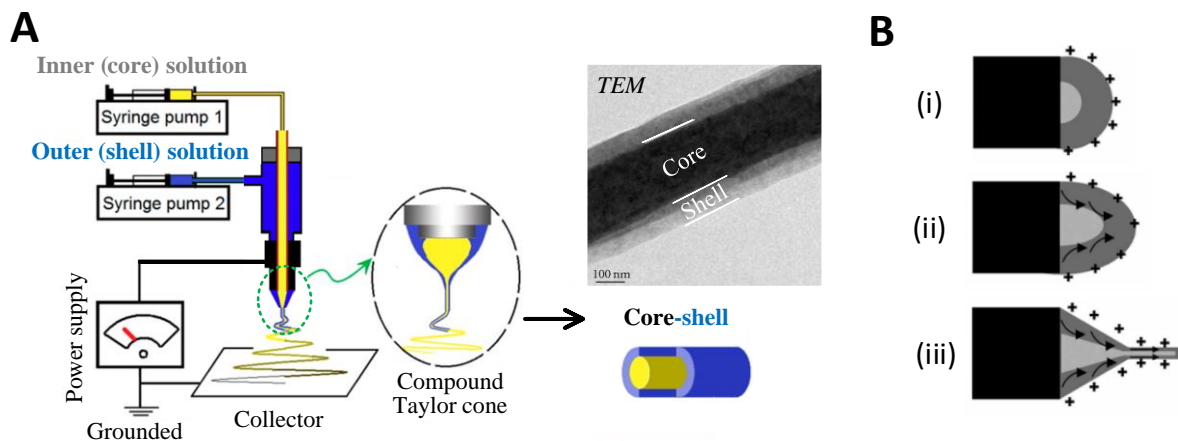
Figure 7: A) Coaxial electrospinning setup and the resulting core-shell fibres structure, adapted from [182, 183]. B) Compound Taylor cone formation (i) Electric charges on the shell solution, (ii) Viscous drag force exerted on the core by the deformed shell droplet, (iii) Core-shell Taylor cone is formed [184].

1.2.2.1 Coaxial electrospinning as a drug-release method

The coaxial electrospinning process enables electrospinning of non-polymeric solutions (as long as one of the solutions is conductive) such as bioactive molecules e.g. drugs and growth factors. Therefore, coaxial electrospinning introduced a new generation of tissue engineering scaffolds as it can be used to achieve sustained, local and efficient delivery of biomolecules by incorporating them into the core of fibres (Figure 8) [185]. Extensive research over the past decade has shown that coaxial nanofibres can be used as a delivery system for various genes, growth factors (GFs) and pharmaceutical compounds including antioxidant, antibiotic, anti-inflammatory and anticoagulation drugs [186-188].
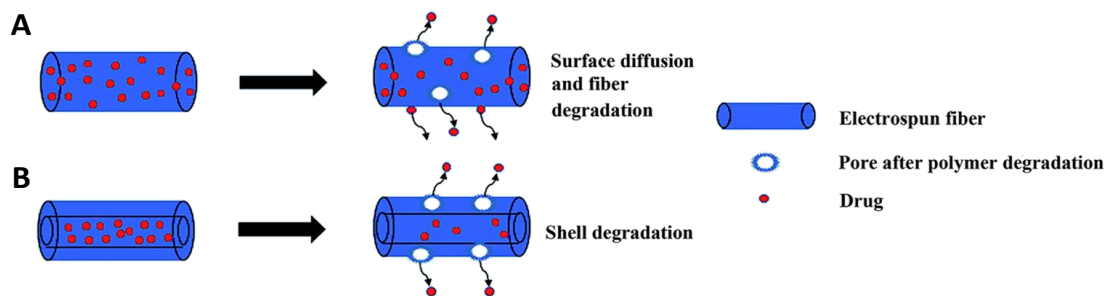
Figure 8: Drug released from electrospun fibres loaded through A) bulk incorporation and B) coaxial incorporation [189].

Liao et al. demonstrated that coaxial electrospinning with a biomolecule solution (in this case viral genes) as the core solution and a polymer shell, improved the functionality of the biomolecules compared to conventional electrospinning [190]. They found that the shell polymer protected the core from direct exposure to the electrospinning environment as well as the in vivo biological surroundings after implantation and that it contributed to the sustained and prolonged release of the biomolecule. The use of two separate solutions further retained bioactivity and prevented modification processes by circumventing direct contact between the aqueous-based biomolecule and the organic solvent of the shell solution [124]. A subsequent study demonstrated that GFs released from coaxial fibres had the same bioactivity as fresh GFs [191].

When coaxially incorporating drugs into the core of nanofibres, the encapsulation efficiency is determined by various parameters of which the relative flow rate of the core and shell solutions is one of the most important. Various other methods have been used to further manipulate the drug release. For example, Liao et al. showed that adjusting the morphology of the fibres, e.g. by including low-molecular-weight polyethylene glycol (PEG) as a porogen into the shell, affected the drug release rate as it resulted in accelerated transport of the core molecules into the environment [190]. They further demonstrated that incorporating certain molecules into the shell solution can also aid in delivering core molecules.

1.2.2.2 Parameters for coaxial electrospinning

The processing, solution and environmental parameters affecting conventional electrospinning are all also applicable to coaxial electrospinning. The addition of a second polymer solution, however, makes electrospinning significantly more complex as more parameters arise. Parameters that have been established to influence coaxial electrospinning include the compatibility of the solutions and the properties of the driving solution [128].

In order for stable Taylor cone formation to occur at the nozzle tip during coaxial electrospinning, the core and shell solutions should be immiscible or semi-miscible. Miscible or incompatible solutions will mix, precipitate or solidify when coming into contact. Traditionally, it was thought that a shell solution with a higher viscosity and flow rate was required for sufficient shear forces to completely entrain the core solution along into a compound jet [128]. This would mean that the shell solution acts as the driving solution and that the core solution does not need to be electrospinnable. It has since been shown that both the shell and core solution can act as the driving solution. To ensure the continuity of the jet and the presence of enough Coulombic repulsion during jet stretching, the driving solution should present sufficient viscosity and electrical conductivity.

Further parameters have emerged over the past decade that were shown to affect coaxial electrospinning, but their relationships have not been fully established as the results from various studies are often contradictory. These parameters include the nozzle geometry and electrical field distribution, the viscosity ratio of the solutions, the evaporation rate of the solvents and the electrical properties of the solutions.

Nozzle geometry and electric field distribution
The diameters of the core and shell nozzle (ratio) and their geometry (length difference and the separation distance) influence the morphology of coaxially electrospun fibres [192, 193].

The length that the inner nozzle protrudes from the outer nozzle has been varied (from protruding to indented) in studies to determine its effect on electrospinning. Rahimi et al. found that slight protrusion is beneficial for core-shell fibre production when the core solution has low viscosity and is non-conducting [193]. On the other hand, Lee et al. introduced a core-cut nozzle, a coaxial assembly with the exit pipe of the core needle completely removed, which was able to produce stable core-shell fibres with a conducting polymer, and observed that jet instability was reduced as the exit of the nozzle was shortened [194].

Tong et al. found that changes in nozzle diameter had an effect on the electric field distribution. Larger nozzle diameters resulted in an increased electric field envelope, which in turn increased the jet whipping angle enabling the production of stable core-shell fibres,

whereas smaller diameter nozzles produced fibres without distinct solution boundaries [195]. According to Wu et al., the core nozzle's position also affects the electrical field generated [196]. If the core nozzle is placed eccentrically, an asymmetric electric field is generated which enhances viscous dragging at the core-shell interface and promotes the formation of helical nanofibres, while a side-by-side needle arrangement results in the lowest electric field.

Viscosity ratio

Apart from the critical role viscosity plays in the formation of a core-shell interface, the ratio of the core and shell solutions' viscosity is also an important parameter. For coaxial electrospinning, both solutions need to meet the viscosity criterion and additionally satisfy the viscosity ratio (η_{core}/η_{shell}) threshold. The viscosity ratio is an important factor in controlling fibre morphology, with an example illustrated in Figure 9.
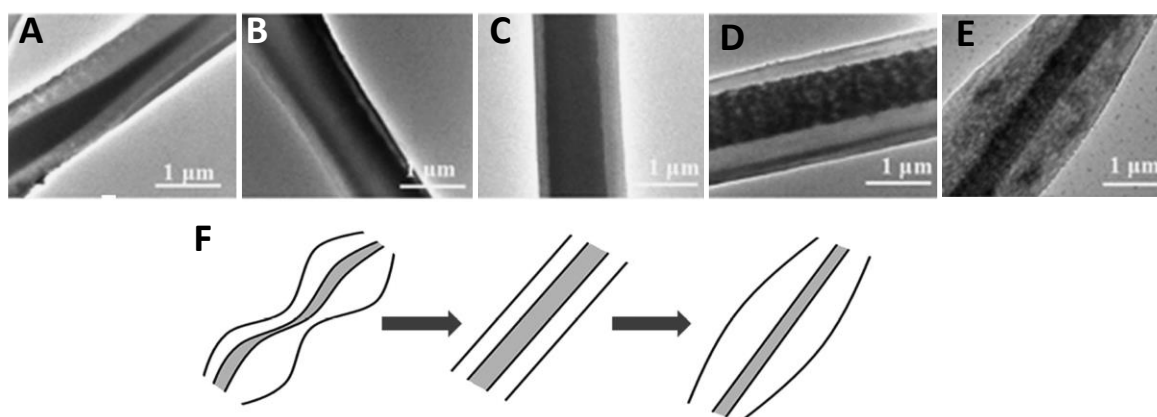
Figure 9: Transmission electron microscopy (TEM) images of electrospun core-shell fibres (PMMA/PAN) prepared with various viscosity ratios of shell/core: A) 0.67, B) 1.22, C) 1.81, D) 2.82 and E) 4.21. F) Schematic diagram of the effect of increased viscosity ration on the core-shell morphology. Adapted from [197].

Tiwari et al. observed that coaxial electrospinning of a PLGA80/20 (in $CHCl_3$/DMF) shell and a PVA (in water) core was not successful when the viscosity ratio exceeded 1.7 due to rapid drying of the shell solution, and when the viscosity ratio was too low (below 0.55) because the viscous drag of the shell solution was either excessive or inadequate for continuous stretching of the core solution causing the core solution to break frequently [198].

Kaerkitcha et al. found that the core diameter decreased with increasing viscosity ratio due to a reduction in the amount of core material flow, while the wall thickness increased because the elongation by the electrostatic repulsion was more difficult for the high viscous shell and the total diameter increased [197]. Furthermore, the diameter of fibres could be altered while maintaining the same morphology with the same viscosity ratio and changing absolute viscosity. Lower viscosity ratios resulted in twisted cores as the shell's viscosity failed to stabilise the core-shell interface. They recommended a range for the viscosity ratio between 1.22 and 2.82.

Evaporation rate of the solvents

Taylor cone formation and jet propagation and elongation are affected by the evaporation of the solvents used. Excessive evaporation rates result in the solution drying at the nozzle before a Taylor cone can form and too low evaporation rates result in an excess of solvent causing drop formation or wet fibres [128]. Fibre collapse and buckling occur when the shell

solution evaporation rate is significantly higher than that of the core solution because the core solution cannot withstand the atmospheric pressure or if the core solution evaporation rate is too high because of the pressure difference between the voids in the core and the atmosphere.

<u>Electrical properties of the solutions</u>

The electrical properties of the solutions strongly influence the instability of the polymer jet as instability is caused by the electric field or disturbed surface charges [199]. It has been established that the shell solution requires intermediate or high conductivity for successful coaxial electrospinning [128]. The addition of salts proved to be an effective way to control the conductivity of solutions without drastically affecting their physical properties, which has significantly increased the range of materials that can be coaxially electrospun.

1.3 Biomaterials

The section to follow introduces the biomaterials selected for this project, i.e. DegraPol®(DP) and polyethylene oxide (PEO) and also provides examples of their use for coaxial electrospinning core-shell fibrous scaffolds.

1.3.1 DegraPol

DegraPol®(DP) is a biodegradable polyester urethane, which consists of block copolymers illustrated in Figure 10 [200]. Both the soft and hard segments are degradable and their products are regarded as non-toxic [201, 202]. The ratio of hard and soft segments can be adjusted to change the mechanical properties according to the need, while the glycolide content at the soft segment side can be adjusted to change the degradation rate (increased glycolide content results in a faster degradation rate) [203-205]. This controlled alteration of hydrolytic degradation is independent of the mechanical properties. DP30, the DegraPol® version used in this project, has a 40:60 hard to soft segment ratio and a 70:30 ε-caprolactone to glycolide ratio, and it has a faster degradation rate than DP0 and DP15 (other established versions of DegraPol®) [203, 205, 206].
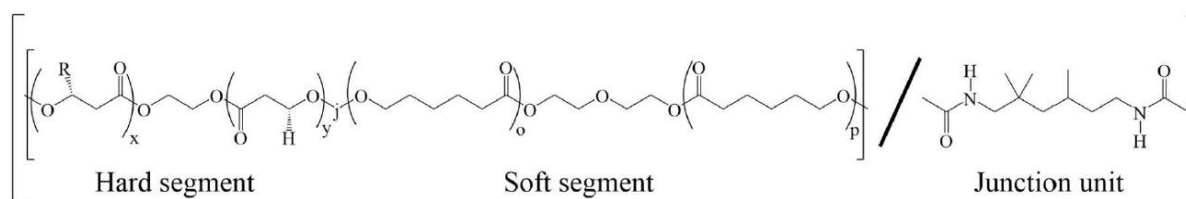
Figure 10: Chemical structure of DegraPol® [207-209].

Various researchers have studied the use of DegraPol® to produce tissue engineering scaffolds, especially via electrospinning, for a wide range of applications such as cardiovascular [210-212], cartilage [213], smooth muscle [214], skeletal muscle and tendon regeneration [207, 215-219]. Only a few studies incorporated bioactive agents into electrospun DP scaffolds via blending or emulsion electrospinning. At the time of writing and to our knowledge, only one work had been published which documented the coaxial electrospinning of DegraPol®.

Evrova et al. produced core-shell fibres with a slightly modified DP15 shell and a polyethylene glycol (PEG, 35 kDa) core with incorporated platelet-derived growth factor-BB (PDGF-BB) for rabbit tendon regeneration application [218]. They established that emulsion and coaxial electrospinning achieved similar encapsulation efficiencies of PDGF-BB in DP scaffolds. However, when comparing the PDGF-BB release profiles of scaffolds produced by coaxial electrospinning to those from emulsion electrospinning, there was a distinct difference, with coaxially electrospun scaffolds yielding a larger initial burst release but also a higher cumulative release percentage after 30 days of in vitro incubation (Figure 11). The released PDGF-BB from both emulsion and coaxially electrospun scaffolds retained its bioactivity.
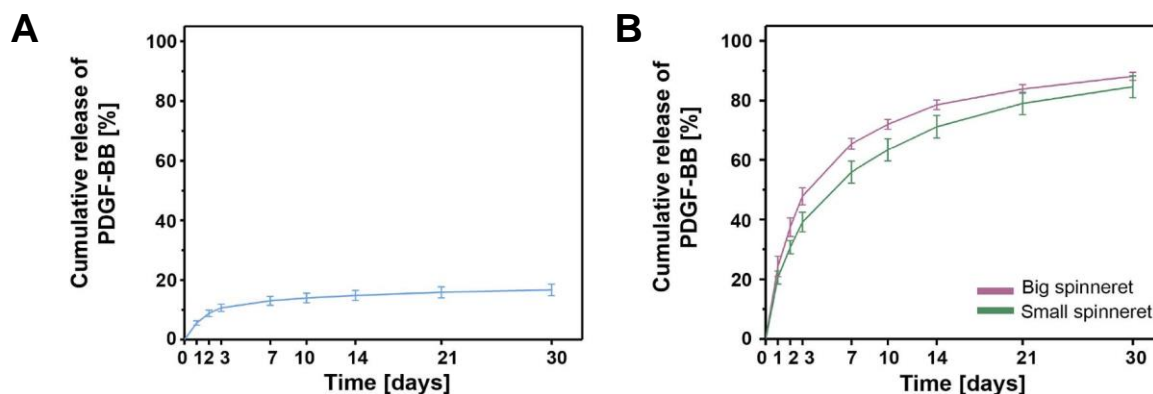
Figure 11: Cumulative PDGF-BB release (%) from DP15 scaffolds produced by A) emulsion and B) coaxial electrospinning [218].

Published studies used chloroform ($CHCl_3$) and/or hexafluoroisopropanol (HFIP) as solvents for producing DP electrospinning solutions. Unpublished work by our research group [209] however documented other possible solving agents for DP which are listed in Appendix A along with their properties. Typical parameters for electrospinning of DP scaffolds are: polymer solution concentrations of 8-30 wt% supplied at flow rates between 0.1 and 12 ml/h through a spinneret with an applied voltage of 5-20 kV placed at a distance of 100-300 mm away from the collector [207, 208, 210-214, 219-222]. These parameters resulted in scaffolds with mean porosities and fibre diameters of 60-83 % and 1.0-25.0 μm respectively.

1.3.2 Polyethelyne-oxide

Polyethylene Oxide (PEO), also called polyethylene glycol (PEG) for lower molecular weights, is a biocompatible water-soluble polymer (repeating unit: $—CH_2CH_2O—$) that is FDA approved for clinical use and frequently used for drug delivery in biomedical applications [223, 224]. One of the major advantages offered by water-soluble polymers in electrospinning is the elimination of the possible toxicity caused by solvents [189]. Furthermore, these polymers can act as drug carriers in drug delivery systems [225-227].

PEO/PEG has been exhaustively explored as an electrospinning polymer [137, 228, 229] with numerous recent studies focusing on its coaxial incorporation into core-shell fibres [189, 223, 230-235]. Esmali & Haseli prepared core-sheath nanofibres with tetracycline hydrochloride and PEO encapsulated in the core and carboxymethyl cellulose in the sheath aimed at achieving sustained antibiotic release and compared to the blend fibres, it displayed a considerably slower and prolonged release [236]. Jiang et al. employed coaxial electrospinning to attain the controlled release of two proteins, bovine serum albumin (BSA)

and lysosome, from core-shell fibres with protein containing PEG as the core and polycaprolactone (PCL) as the shell [237].

1.4 Heparin-eluting filaments

1.4.1 Heparin

Heparin, a negatively charged polysaccharide, is one of the most salient anticoagulants used in clinic and it is also a multifunctional bioactive molecule. Heparin has a non-homogenous chemical structure and molecular weight depending on the tissue source. It has an average molecular weight of 12 000 and an average molecular length of 9 nm [238].

1.4.2 Heparin inclusion

Heparin has both antithrombotic and anti-inflammatory properties and its inclusion into electrospun scaffolds can prevent mid-graft thrombosis, potentiate growth factors (GFs) for enhanced healing as well as subdue undue proliferation of smooth muscle cells that leads to IH [239-241]. Additionally, heparin-GF-bindings was found to stabilise GFs against thermal denaturation and degradation by ECM proteinases [181, 242]. Some recent studies have also suggested that heparin might have the potential to enhance endothelial cell proliferation [243-245], while others advocated the opposite [246].

As heparin offers multiple advantages for implanted tissue engineering scaffolds, several studies have been undertaken to find alternative methods to incorporate heparin into the scaffold structure rather than just administering heparin via injection/medication. This would allow the sustained local release of heparin within the scaffold structure without the need for chronic medication. These methods (Figure 12) include, but are not limited to, physical absorption and inclusion into the bulk of electrospun fibres. Physical absorption entails chemically binding modified heparin onto the structure surface; or soaking the structure in heparin. Heparin can be incorporated into the bulk of electrospun fibres by directly blending heparin into the polymer solution before electrospinning; or through a process known as emulsion electrospinning, where two immiscible solutions are mixed to form a water-in-oil or an oil-in-water emulsion [247].
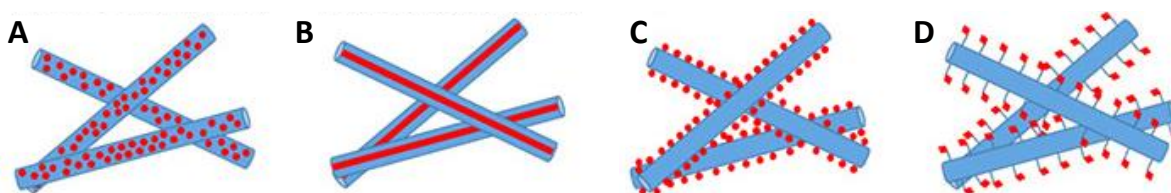
Figure 12: The resulting structures of drug incorporation methods for electrospun fibres: A) blend/emulsion electrospinning, B) coaxial encapsulation, C) physical absorption and D) surface modification (chemical immobalization) [248].

Although these methods met with some success, they resulted in burst release, reduced bioactivity (due to intended/unintended modification of heparin) and rapid (albeit controlled) elution of the heparin due to bulk degradation of the polymers [35, 249]. Furthermore, these methods often lack reproducibility and have also been recorded to weaken the scaffolds mechanically (weakening fibres). Two examples of these studies include Chen et al. that

incorporated heparin and VEGF into PLLA-CL fibres through emulsion electrospinning [249] and Duan et al. that heparinised the surface of PCL/COL coaxial fibres immersion [186]. More recent studies of heparinised vascular grafts have been evaluated in large animal models [250, 251].

The only commercially available heparinised vascular grafts are made of ePTFE (VASCUGRAFT® FLOW, PM® Flow Plus, Flowline BIPORE®, Fusion Bioline®, Propaten®) or Dacron (Intergard®). These grafts provided improved but still suboptimal patencies [252, 253].

1.4.3 Heparin incorporated coaxial fibres

The following subsection provides a summary of previous studies where heparin was coaxially incorporated into electrospun fibres to establish the effect on morphology, mechanical properties, heparin release profiles, cell culture response, in vivo response (graft patency, animal models used) and the limitations of the studies. A summary of each study as well as the electrospinning parameters are provided at the end of this section in Table 2 and Table 3 respectively.

<u>Varying core/shell flow ratios, polymer concentrations and heparin quantities</u>

Chen et al. coaxially electrospun heparin loaded P(LLA-CL) vascular grafts and investigated the effect of the flow rate of the core and shell solutions on the core-shell structure, fibre morphology and the inhibition of fibroblast proliferation [254]. The core and shell solutions were pumped at proportions of 1:3, 1:2 and 1:1 at a constant total feeding rate (refer to Table 3). There was a direct correlation between the core solutions flow rate and the diameter of the core layer, but beading occurred when the core solutions flow rate exceeded a specific threshold. The authors attributed bead formation to the difference in properties between the core and shell solution in terms of solvent volatility and water content causing insufficient pulling force at the needle tip. Stable core-shell fibres were produced at 1:2 and 1:3 ratios, with beading occurring at 1:1 ratio as shown in Figure 13. The smallest fibres were obtained from the 1:3 ratio. Cell viability tests showed that heparin incorporation had a strong inhibitory effect on the proliferation of fibroblasts compared to controls.
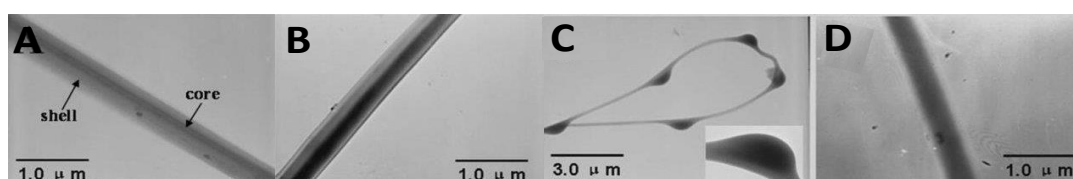
Figure 13: TEM images of core-shell fibres produced with feeding ratios (inner:outer solution) of A) 1:3, B) 1:2 and C) 1:1; and pure P(LLA-CL) fibres [254].

Su et al. found that increased quantities of heparin (0.5, 1.0 and 2.0 wt%) coaxially incorporated into PLLACL fibres resulted in up to 40 % decrease in fibre diameters (Figure 14A-D) compared to the control group [255]. This was ascribed to be due to the addition of highly charged molecules (negatively charged heparin) increasing charge density which in turn caused greater elongation of the jet. The ultimate tensile stress of coaxially electrospun nanofibrous mats was also found to be less compared to pure PLLACL mats, which corresponded with a previous study that indicated coaxial fibres with water-soluble cores, in

general, were weaker than pure polymer fibres [256]. Less heparin loading resulted in faster relative heparin release rates and the release rate could be adjusted by changing the ratio of the core-thickness to the shell-thickness (Figure 14E). Morphology after release suggested that heparin was primarily released by a diffusion/erosion mechanism as the degree of degradation was not high. However, the post-release results indicated that there was a distinct difference in degradation degree for different heparin contents, with more heparin resulting in higher degradation, since nanofibres with more heparin had smaller diameters which enhanced the specific surface area and higher heparin content also meant that more heparin was released (mass loss). In vitro culturing of VSMC indicated that compared to controls, coaxial incorporation of heparin had an inhibitory effect on the proliferation of VSMCs, which confirmed that heparin maintained its bioactivity even after coaxial electrospinning.
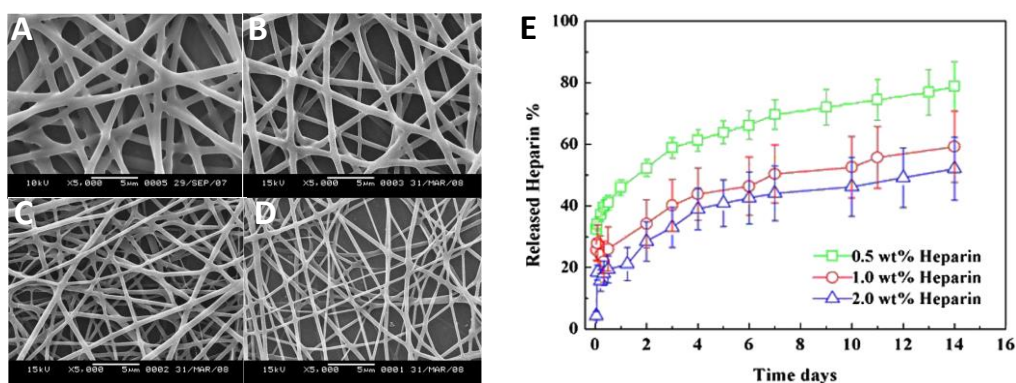
Figure 14: A - D) SEM images showing different fibre sizes of coaxially electrospun PLLACL/heparin fibres prepared containing different heparin amounts at A) 0, B) 0.5, C) 1 and D) 2 wt% of PLLACL wt [255]. E) In vitro heparin release profiles from PLLACL fibres different proportions of heparin coaxially incorporated [255].

Yin et al. initially found that COL/chitosan/PLCL nanofibrous grafts caused thrombus formation [257], and subsequently coaxially encapsulated heparin into grafts with different polymer concentrations [258]. With constant heparin concentration, the average diameter steadily decreased by 38 % as chitosan and COL content increased. However, with constant shell volume ratios, an increase in heparin did not have a gradual effect (5 % = 769 ± 234 nm, 15 % = 744 ± 198 nm, 30 % = 517 ± 112 nm), which the authors ascribed to the increase in heparin content leading to increased ion formation, increasing conductivity. Larger diameter fibres resulted in prolonged heparin release as thicker walls meant longer diffusion distance for heparin. Therefore it was hypothesised that the drug release rate could be controlled by varying shell ratios, which would lead to different fibre diameters.

The shell ratio primarily influenced the UTS of the graft rather than the core concentration, with increased PCL resulting in higher UTS. Similarly, increased PCL resulted in higher ultimate strain, however, the heparin concentration had an obvious effect on the ultimate strain. The compliance decreased by half with increased heparin content (from 5 % to 30 %) for the 40:10:50 graft suggested being due to the flexibility of the graft changing with the addition of heparin.

In general, a faster relative heparin release rate was observed with less drug loading and a slower rate with a higher drug loading amount. The graft most suitable for application in clinical use was the graft (40:10:50-15 %) with a high drug-load amount, a high encapsulation

efficiency, a low initial burst release and a stable sustained release. Overall the grafts with heparin loading were favourable for the proliferation of in vitro cultured ECs compared to controls but higher released concentrations and faster rates caused cell growth to slow down. These cell proliferation results suggested that heparin in an appropriate concentration can lead to enhanced cell growth.

When directly comparing the heparin release profiles of the grafts from these last two studies [255, 258], a much larger initial burst and faster release was displayed by the first study [255]. This was likely due to the shell consisting of only pure polymer and the conductivity being changed, which in turn changes the fibre structure and alters the loading capacity of heparin [258]. The authors stated that adding COL and chitosan to the shell solution hindered the heparin from being distributed on the surface or close to the surface of the fibres, resulting in a more controlled release.

Heparin loading vs pre-endothelialisation

Huang et al. conducted a pilot study aimed at comparing and showing the suitability of the two most used antithrombotic methods – heparin loading and pre-endothelialisation, for clinical application in vascular grafts [259]. Bi-layered heparin loaded P(LLA-CL) grafts were fabricated by coaxially incorporating heparin into the inner layer of fibres, while pre-endothelialised grafts were obtained by seeding ECs on the luminal surfaces of pure P(LLA-CL) and maturing in a specifically designed bioreactor.

Compared to controls (pure P(LLA-CL)), heparin loaded P(LLA-CL) scaffolds presented 36 % smaller fibre diameters and 22 % less mechanical strength. In vivo analysis of both graft types (heparin loaded and pre-endothelialised) showed equally enhanced patency of 100 % at 2 weeks and 75% at 3 months in comparison to 50 % at 2 weeks and 12.5 % at 3 months in the control group. Tensile testing of the implanted grafts after excision showed superior tensile properties in the pre-endothelialised grafts compared to the heparin loaded grafts, probably due to the difference in the fibre structure. Histological analysis of the implanted heparin loaded grafts showed only a cell monolayer at the proximal end with a few cell islands at the middle and distal end which suggests that the scaffold was not fully able to accommodate TM endothelialisation. The pre-endothelialised graft however had a confluent cell monolayer at the proximal, middle and distal section and even had some cell infiltration into the pores.

A subsequent study further investigated the combination of both heparin loading and pre-endothelialisation on the in vivo response, as opposed to their separate application [260]. Similar to the previous study, the addition of heparin caused a decrease in ultimate tensile stress, and also a decrease in burst pressure and an increase in suture retention and compliance. In vitro assessment proved greater EC viability and proliferation on P(LLA-CL) and heparin loaded P(LLA-CL) scaffolds than on PCL scaffolds after 7 days, with almost no EC on PCL scaffolds, numerous ECs attached and growing on the luminal surface of P(LLA-CL) scaffolds and a well spread EC monolayer on the heparin loaded P(LLA-CL) grafts. Interestingly, in contrast with previous reports stating that heparin is a potent antiproliferative agent, the extent of EC proliferation was no different between P(LLA-CL) and heparin loaded P(LLA-CL) scaffolds after a week of dynamic cell culture. The authors were unsure of the cause but suggested it might be due to the controlled release of heparin preventing heparin from exerting antiproliferative action against ECs.

In vivo assessment of these grafts (specifics in Table 2) showed superior patency at 24 weeks among the pre-endothelialised heparin loaded grafts (85 %) compared to pre-endothelialised P(LLA-CL) grafts (66.7 %), heparin loaded grafts (37.5 %) and pure P(LLA-CL) grafts (12.5 %). This suggested that pre-endothelialisation has a greater influence on patency than heparin loading but seeing that 90 % of heparin was released after 12 weeks, there was almost no heparin left for the remaining 12 weeks which could be the cause for graft thrombosis. The enhanced patency of the joint application of heparin loading and pre-endothelialisation was ascribed to the following mechanisms: "*firstly, the coverage of autologous ECs through in vitro pre-endothelialization provided an anticoagulant and anti-thrombogenic luminal surface for the scaffolds to avoid acute thrombosis; secondly the coverage of ECs ensured the luminal integrity of the vascular grafts and prevented the occurrence of inflammatory responses, which have been demonstrated to cause intimal hyperplasia; thirdly, the sustained release of heparin from heparin-bonded P(LLA-CL) nanofibres reduced thrombin-mediated fibrin formation and platelet activation. In addition, heparin also offered a negative-charged surface to block the interaction between platelets and scaffolds by electrostatic repulsion, thus contributing to the prevention of thrombotic occlusion*" [260].

Huang et al. concluded that even though pre-endothelialised grafts possessed better mechanical properties and cellular compatibility, heparin loading provided a comparatively economical and easy alternative to enhancing in vivo results [259]. Similarly, even though the combination of heparin loading and pre-endothelialisation proved to be a promising strategy to overcome poor patency, the whole process to construct this type of graft requires 2 weeks before being ready for implantation, showing that this is only an option for elective vascular surgery [260].

Addition of other biomolecules

Further research was done to investigate the effect of adding other biomolecules in the core along with heparin. This included salvia, rosuvastatin calcium and vascular endothelial growth factor (VEGF).

Kuang et al. incorporated heparin and Salvianolic acid B (SAB) extracted from a traditional Chinese herb, Salvia, known to promote endothelial cell adhesion, migration and protection [261]. SAB with proved anti-inflammatory, antioxidative, anti-arteriosclerotic, anti-hypoxic and antiapoptotic properties, easily decomposes in aqueous solution and therefore had to be loaded (via physical absorption) into a drug-loading medium i.e. mesoporous silica nanoparticles (MSN) and blended into the shell solution. Grafts produced for this study included coaxially electrospun heparin cores with either PLCL/COL blended SAB-MSN or PLCL/COL shells, and control groups of electrospun PLCL/COL blended SAB-MSN and PLCL/COL.

Contrary to previous studies, there was an increase in average fibre diameter of 26.6 % and 29.7 % with the addition of heparin in the pure PLCL/COL and SAB/MSN containing PLCL/COL grafts respectively. The contact angle of PLCL/COL fibres decreased from 118° to 81° and 65° with the incorporation of SAB-MSN and heparin respectively, while fibres with both SAB-MSN and heparin displayed a contact angle of 31°, demonstrating that SAB-MSN and heparin, separately and together, increase the hydrophilicity of fibre membranes.

The heparin/SAM-MSN fibres showed an initial burst release of 36 % and a steady accumulative sustained release of 68 % at 30 days (Figure 15A). HUVEC adhesion was significantly higher on the grafts containing SAB-MSN than those without and cell proliferation was significantly higher in grafts containing heparin (ascribed to the increased hydrophilicity). It was postulated that SAB and heparin had a synergistic effect as heparin comprising grafts presented strong anticoagulation, with the highest anticoagulation ability exhibited among the heparin/SAB-MSN grafts. In vivo comparison (Table 2) showed less inflammatory cells and a red tissue layer on the heparin/SAB-MSN grafts indicating improved biocompatibility compared to pure PLCL grafts. In summary, the addition of heparin and SAB effectively prevented acute thrombosis and promoted rapid endothelialisation of blood vessels.

Feng et al. from the same group investigated coaxially loading heparin and rosuvastatin calcium (Ros-Ca) in P(LLA-CL) nanofibres to cover stent-grafts for aneurysm treatment [262]. Varying ratios of heparin and Ros-Ca in the core solution were electrospun directly onto metal stents. Similar to the abovementioned study, fibre diameter increased with the addition of heparin and Ros-Ca but decreases with increased amounts of Ros-Ca. The heparin and Ros-Ca incorporated fibres had higher tensile strength than the control group, but increased amounts of Ros-Ca led to a decrease in tensile strength.

In vitro HUVEC culturing showed that too high heparin content affected cell adhesion negatively as the fibres with the most heparin displayed worse biocompatibility than the control group. Increased Ros-Ca contents showed an increased tendency to cell proliferation, with the nanofibres containing the highest Ros-Ca contents exhibiting the most superior biocompatibility. The anticoagulation properties were enhanced with the addition and synergistic effects of heparin and Ros-Ca and the grafts with the highest Ros-Ca content showed the best anticoagulation ability. Only the release of Ros-Ca was investigated and it demonstrated a continuous and stable release to 31% (cumulative) over 83 days.

Hu et al. conducted an in vitro and in vivo study of bi-layered coaxial electrospun vascular grafts loaded with heparin and vascular endothelial growth factor-165 ($VEGF_{165}$) aiming to offer better patency rate and biocompatibility than ePTFE grafts by promoting the proliferation of endothelial cells in the early postoperative phase [263]. The shell polymer for both the inner and outer layer consisted of blended P(LLA-CL), COL and elastin, while the core solutions consisted of heparin dissolved in pure water (inner layer) and human recombinant $VEGF_{165}$ dissolved in bovine serum albumin (BSA) solution (outer layer). Coaxial fibres with a pure P(LLA-CL) shell and BSA without $VEGF_{165}$ core were produced for blank controls.

There was a sustained release of heparin and $VEGF_{165}$ over 4 weeks, with an initial burst release of 48 % and a cumulative stable release of 77 % at 28 days for heparin and in comparison, $VEGF_{165}$ displayed a relatively flattened cumulative release curve to 56 % at 28 days (Figure 15B). After one week of in vitro culture (Table 2), the heparin and $VEGF_{165}$ loaded grafts displayed significantly higher cell proliferation than ePTFE grafts, confirming the presence of bioactive $VEGF_{165}$, and a clear confluent monolayer was present on the electrospun surface compared to scattered cells on ePTFE grafts. In vivo comparison between the bi-layered and ePTFE grafts in a rabbit model showed enhanced patency at 4 weeks in the bi-layered grafts (86.7 %) compared to the ePTFE grafts (40 %) despite no postoperative anticoagulant administration. Histological analysis showed a trend for endothelialisation and

no mural thrombus, suggesting that heparin loaded grafts have the potential to maintain a safe period of no anticoagulant administration during the early postoperative phase, providing controlled release and an antithrombotic surface.
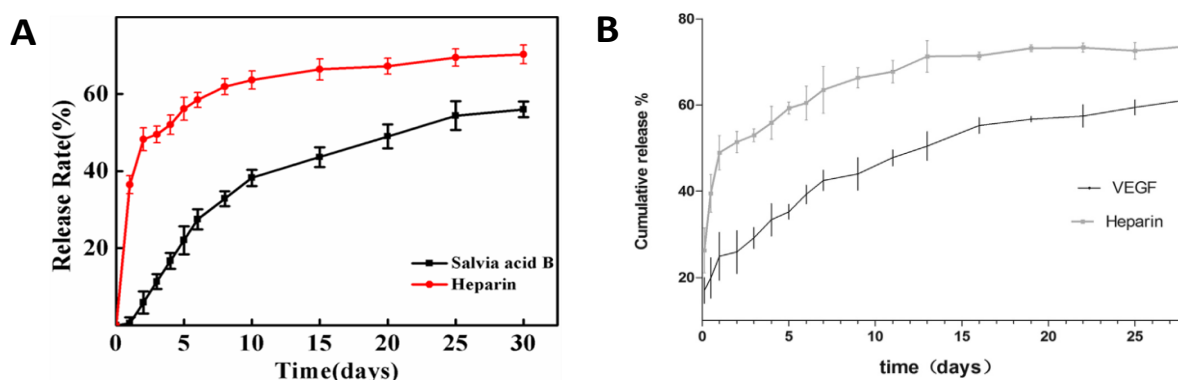
Figure 15: A) Heparin and SAB cumulative release response from coaxially electrospun fibres produced by Kuang et al. [261]. B) Heparin and VEGF cumulative release rate from coaxially electrospun fibres produced by Hu et al. [263].

Jia et al. coaxially incorporated both VEGF and heparin into dextran/PLGA core-shell fibrous membranes [242]. They found that beading occurred for higher concentrations of heparin (10 µg/ml vs 5 µg/ml), which was ascribed to the negative charges in the heparin increasing the instability of the electrospinning process. Additionally, they speculated that the introduction of heparin lessened the initial burst release of VEGF compared to BSA due to the heparin-binding regulating the VEGF over an extended time, resulting in a more smooth VEGF release.

Heparin incorporated into the shell

Rather than incorporating heparin into the cores of fibres, some researchers incorporated it into the shell polymer. Ye et al. investigated the healing mechanism of sutures comprising of heparin-loaded (emulsion in shell solution) core-shell fibres seamed into ruptured rat Achilles tendons and found that these high heparin loaded sutures performed better compared to sutures with lower heparin concentrations or with no heparin [264]. The high heparin concentration decreased the immune-inflammatory response and the VEGF concentration present increased by 37.5 %. Altogether, heparin loaded sutures promoted healing and regeneration of the Achilles tendon.

Hou et al. produced coaxially electrospun magnetic cellulose−Fe_3O_4 core−shell fibres that were heparinised either by blending heparin into the cellulose shell or by covalent immobilisation of heparin onto the surface of the cellulose shell [265]. An amidolytic assay, used to analyse the anticoagulant activity of the structures, confirmed the presence of accessible bioactive heparin on the surface of both fibre types. Cellulose−Fe_3O_4 core−shell fibres with covalently immobilized heparin presented notably larger fibre diameters (2.7 µm) compared to those with heparin blended into the shell (≈ 1 µm), while blended cellulose−Fe_3O_4−heparin monofilament fibres were much thinner (375 nm). This agrees with previous studies showing a trend that heparin addition decreases fibre diameter due to increased jet instability during electrospinning (caused by negative charge).

Table 2: Summary of heparin eluting scaffolds results.

Authors	Study aim	Shell polymer	Core polymer	Control	Patency	Heparin initial burst (24h)	Heparin sustained release	In vitro cells cultured	Animal model
Chen et al. [254]	Compares the effect of core and shell flow rate on fibre structure and inhibition of fibroblast.	P(LLA-CL)	Heparin + gelatin	P(LLA-CL)	N/A	N/A	N/A	Fibroblasts	N/A
Su et al. [255]	Investigate effect of different Hep. quantities (0.5, 1.0 and 2.0wt%) in the core on on fibre morphology, heparin release rate and SMC proliferation.	PLLACL	Heparin	PLLACL	N/A	20-45 %	70 % (14 days)	VSMC	N/A
Yin et al. [258]	Determine effect of different of Hep. and shell polymer conc. on morphology, release, in vitro EC growth and mechanical properties.	COL/ chitosan/ PLCL	Heparin	older study	N/A	18-40 %	60-96 % (45 days)	Porcine iliac artery Ecs	N/A
Huang et al. [259]	Investigate clinical suitability of heparin loading vs pre-endothelialisation on bi-layered VGs	P(LLA-CL)	Heparin	P(LLA-CL)	100% (week 2) 75% (3 months)	50 % (20% immediate)	72% (14 days)	Canine femoral ECs	Canine bilateral femoral replacement
Wang et al. [260]	Investigate combination of heparin loading and pre-endothelialisation on bi-layered VGs	P(LLA-CL)	Heparin	P(LLA-CL), PCL	24 weeks: Control = 12.5 % Hep. load = 37.5 % Pre-endoth. = 66.7 % Combo = 85 %	25 % (1 week)	90 % (12 weeks)	Canine femoral ECs	Canine bilateral femoral replacement
Kuang et al. [261]	In vivo comparison of Heparin and SAB incorporation in fibrous membranes	PLCL/COL or PLCL/COL+SAB/MSN	Heparin	PLCL/COL	N/A	36%	68 % (30 days)	HUVEC	SD rats (subcutaneous)
Feng et al. [262]	Investigate various concentrations of heparin + Ros-CA on endovascular stent coating	P(LLA-CL)	Heparin+ BSA & Ros-Ca	N/A	N/A	N/A	Ros-CA = 21.9 - 31.1 %	HUVEC	N/A
Hu et al. [263]	In vitro and in vivo evaluation of combined of heparin and VEGF incorporation in bi-layered VGs	P(LLA-CL), COL, protein& elastin	Heparin (inner), VEGF (outer)	P(LLA-CL)/BSA (no VEGF), ePTFE	28 days: 86% (coax) 40% (ePTFE)	48%	28 days: 77 % (Hep), 56 % (VEGF)	HAEC	Rabbit infra-renal aorta
Jia et al. [242]	Evaluation of coaxial incorporation of VEGF+Hep+Dextran into PLGA fibrous membranes	PLGA	DEX + VEGF+ BSA + heparin	DEX/PLGA, PLGA	N/A	19.3% (VEGF) 59.8 % (BSA)	28 days: 81.6% (VEGF), 77 % (BSA)	HUVEC	N/A
Ye et al. [264]	Examination of healing mechanism of heparin loaded sutures for rabbit Achilles tendon regeneration	PLLA + Heparin	PA-6	PLLA with low Hep conc. or no Hep	N/A	≈ 5 -10 %	67.5 - 88.5 % (28 days)	N/A	Rabbit tendon model
Hou et al. [265]	Evaluation of magnetically responsive heparin-immobilized cellulose nanofibre composites produced by wet-wet electrospinning.	Cellulose + Heparin	Fe₃O₄	Cellulose/Fe3O4 with hep immo-balised surface	N/A	N/A	N/A	N/A	N/A

N/A: not available or not applicable, P(LLA-CL): poly(L-lactic acid-co-ε-caprolactone), PLCL: poly(L-lactide-co-caprolactone), SAB: Salvianolic Acid B, MSN: Mesoporous silica nanoparticles, PLGA: poly(lactide-co-glycolide), PCL: polycaprolactone, BSA: bovine serum albumin, Ros-Ca: rosuvastatin calcium, VEGF: vascular endothelial growth factor, DEX: Dextran, PA-6: polyamide-6, FE3O4: Superparamagnetic magnetite, COL: collagen, VSMC: vascular smooth muscle cells, EC: endothelial cell, HUVEC: human umbilical vein endothelial cells, HAEC: human aortic endothelial cells, SD: Sprague Dawley

Table 3: Summary of parameters for fabrication of heparin-eluting scaffolds.

Authors	Shell polymer	Core polymer	Shell solvent	Core solvent	Fow rate (ml/h) Shell	Core	Appl. kVs (+)	TCD (cm)	Graft ID (mm)	Fibre diameter
Chen et al. [254]	P(LLA-CL)	Heparin + gelatin	Water/ TFE	Water/ TFE	0.9, 0.8, 0.8	0.3, 0.4, 0.6	15	20 (down)	1.5 & 4	413 nm (avg)
Su et al. [255]	PLLACL	Heparin	TFE	Water	1.0	0.1	N/A	12	N/A (flat)	765 ± 98 nm (PLLACL control) - 437 ± 134 nm (coax)
Yin et al. [258]	COL/ chitosan/ PLCL	Heparin	HFP/ TFA	Water	1.0	0.2	12	12	4	517nm - 938nm
Huang et al. [259]	P(LLA-CL)	Heparin	TFE	Water	0.8	0.1	18	15	4	321 nm (hep loaded avg), 506nm (control)
Wang et al. [260]	P(LLA-CL)	Heparin	TFE	Water	0.8	0.2	18	15	3	several hundred nms
Kuang et al. [261]	PLCL/COL or PLCL/COL + SAB/MSN	Heparin	HFIP	Water	1.0	0.1	14	N/A	N/A (flat)	714 ± 87 nm (Hep) 821 ± 162 nm (Hep + MSN)
Feng et al. [262]	P(LLA-CL)	Heparin+ BSA & Ros-Ca	HFIP	PBS (hep), DMSO (Ros-CA)	2.0	0.1	11	10 to 25	2.5 (stent)	1211 ± 226 to 1474 ± 347 nm
Hu et al. [263]	P(LLA-CL), COL, protein & elastin	Heparin (inner), VEGF (outer)	HFIP	Water (inner), BSA (outer)	0.1	1	16	15	4	N/A
Jia et al. [242]	PLGA	DEX + VEGF+ BSA + heparin	CHCl3/ TFE	Water	0.6	0.2	13 - 15	15	N/A (flat)	≈ 1 to 2 μm
Ye et al. [264]	PLLA + Heparin	PA-6	HFP	HFP	4	2	2.5	5 mm (NFE)	N/A	0.74 μm
Hou et al. [265]	Cellulose + Heparin	Fe_3O_4	[EMIM] [Ac]	[EMIM] [Ac]	0.2 - 0.23	0.2 - 0.23	12 to 16	15	N/A (flat in bath)	≈ 1 μm

ID: inner diameter, N/A: not available or not applicable, P(LLA-CL): poly(L-lactic acid-co-ε-caprolactone), PLCL: poly(L-lactide-co-caprolactone), SAB: Salvianolic Acid B, MSN: Mesoporous silica nanoparticles, PLGA: poly(lactide-co-glycolide), PCL: polycaprolactone, BSA: bovine serum albumin, Ros-Ca: rosuvastatin calcium, VEGF: vascular endothelial growth factor, DEX: Dextran, PA-6: polyamide-6, FE_3O_4: Superparamagnetic magnetite, TFE: Trifluoroethanol, HFIP / HFP: hexafluoro-2-propanol, TFA: Trifluoroacetic acid, CHCl3: chloroform, [EMIM][Ac]: 1-methyl-3-methylimidazolium acetate, COL: collagen.

1.5 Drug release kinetics models

Bioactive molecules are mainly released from electrospun scaffolds through means of diffusion [218, 266-272]. Factors such as the physiological condition, polymer degradation, scaffold/fibre morphology (affects the diffusion distance/gradient), and the solubility of the polymer and bioactive molecule are known to influence the diffusion profile along with the

drugs type, crystallinity, molecular weight, polymorphic structure, its solubility in the release fluid and the total quantity of drug-loaded in the scaffold [273-275].

Various drug release kinetics models have been established to aid researchers in describing drug dissolution from polymer matrixes which are listed in Table 4. The release mechanism considered to be ideal for numerous drug delivery applications is a sustained delivery, zero-order release kinetic mechanism for which the release is constant over time irrespective of the drug concentration [276, 277]. Korsmeyer-Peppas and Higuchi are also considered to be some of the best models to describe drug release responses from polymer matrices [273].

Table 4: Drug dissolution models. Adapted from [267, 273].

Model	Equation
Zero-order	$W_t = W_0 + k_0 t$
First-order	$\ln W_t = \ln W_0 + k_1 t$
Second-order	$W_t / W_\infty (W_\infty - W_t) k_2 t$
Hixson-Crowell	$W_0^{1/3} - W_t^{1/3} = k_s t$
Weibull	$\log[-\ln(1 - (W_t / W_\infty))] = b \times \log t - \log a$
Higuchi	$W_t = k_H t$
Baker-Lonsdale	$(3/2)[1 - \left(-1(W_t / W_\infty)\right)^{2/3}] - (W_t / W_\infty) = kt$
Korsmeyer-Peppas	$W_t / W_\infty = k_K t^\epsilon$
Quadratic	$W_t = 100(k_1 t^2 + k_2 t)$
Logistic	$W_t = A/[1 + e^{-K(t-y)}]$
Gompertz	$W_t = A\, e^{-e-K(t-y)}$
Hopfenberg	$W_t / W_\infty = 1 - [1 - k_0 t / C_0 a_0]^\epsilon$

W: The amount of drug dissolved, k: release constant, ϵ: release exponent, t: time, a: scale parameter, b: shape parameter, C_0: solution concentration

Different diffusion transport mechanisms are distinguished through the use of interpretation values. These transport mechanisms (Table 5) include Fickian diffusion, Non-Fickian transport, Case II transport and Super Case II.

Table 5: Diffusion release kinetics interpretation values. Adapted from [278].

Drug transport mechanism	Release exponent (ϵ)	Rate as a function of time
Fickian diffusion	0.5	$t^{-0.5}$
Non-Fickian transport	$0.45 < \epsilon = 0.89$	$t^{\epsilon - 1}$
Case II transport	0.89	Zero-order
Super case II transport	> 0.89	$t^{\epsilon - 1}$

1.6 Research Proposal

This project intends to overcome or mitigate some of the limitations from previously attempted heparin incorporation methods (physical absorption, blend and emulsion electrospinning) such as initial burst release, reduced bioactivity and rapid elution, by the coaxial of core-shell fibres with heparin and GFs cores within polyurethane shells.

1.6.1 Aims and Objectives

This research project aims to develop tubular, small-diameter vascular grafts comprising of electrospun degradable (Degrapol®, DP30) fibres with coaxially incorporated heparin for possible application in the tissue engineering of blood vessel substitutes.

The objectives to be met to achieve this aim are to:

1. Upgrade the electrospinning equipment and rig setup to facilitate the coaxial electrospinning process.

2. Determine the conditions for core-shell electrospinning of degradable polymers (DP30) with water soluble cores (PEO) onto a large mandrel (25 mm) to produce fibrous scaffolds with coaxially incorporated heparin.

3. Fully characterise the morphology of the electrospun scaffolds.

4. Determine the mechanical tensile properties of the electrospun scaffolds.

5. Analyse the thermal response of electrospun scaffolds and raw polymers.

6. Establish the drug elution profiles and drug activity (after incorporation and release) of the electrospun scaffolds.

7. Establish the hydrolytic degradation response over time of incubated electrospun scaffolds.

8. Determine the polymer swelling over time of cast polymer films in water as well as the wettability (contact angle) of the polymer films and electrospun scaffolds.

9. Determine the conditions for translating the electrospinning techniques from a large to a smaller mandrel to allow the fabrication of small diameter (2.6 mm) vascular grafts with coaxially incorporated heparin and characterise their morphological and mechanical properties.

1.6.2 Motivation

The clinical application of vascular grafts with heparin included into the fibres hopes to potentially reduce the inflammatory response, enhance healing by potentiating GFs and prevent mid-graft thrombosis and SMC proliferation (leading to IH). This project proposes the use of fibrillar drug-eluting scaffolds, immediately capable of fulfilling the basic function of a vessel (conducting blood flow) and retaining long-term function after being endothelialised and remodelled into a living neo-artery. The in vivo regeneration of living, functional neo-arteries offers the possibility to provide much needed and improved outcomes, especially in long, peripheral applications where current synthetic grafts provide poor patency.

2 Materials and methods

This chapter describes the materials and methods used to produce drug-eluting electrospun scaffolds, the processes performed to characterise the morphological, mechanical, and thermal properties of the scaffolds and the determination of the corresponding drug release and degradation responses over a 6-week period.

2.1 Materials

The biomaterial chosen for electrospun scaffold development was a biodegradable polyester urethane block copolymer, Degrapol®30 (DP30, 1.15 g/cm^3, ab medica S.p.A., Lainate, Italy)., Polyethylene oxide (PEO, 400 kDa), a water-soluble polymer obtained from Sigma-Aldrich (Pty) Ltd (RSA) was incorporated into fibres. Heparin sodium (HepNa$^+$, from porcine intestinal mucosa) was purchased from Celsus Laboratories Inc. (Cincinnati, USA). All other reagents and solvents were obtained from Sigma Aldrich (RSA), Saarchem Holpro Analytic (RSA), Fluka Chemie AG (Buchs, Switzerland), Merck Millipore (Pty) Ltd. (RSA) and Oakwood Chemicals (USA) unless specified otherwise.

2.2 Heparin modification

Heparin sodium was modified to heparin tributylamine (HepTBA) by ion exchange, illustrated in Figure 16, during which the sodium ions (Na$^+$) were exchanged for hydrogen ions (H$^+$) and thereafter replaced by tributylamine (TBA) to render it soluble in organic solvents [279].
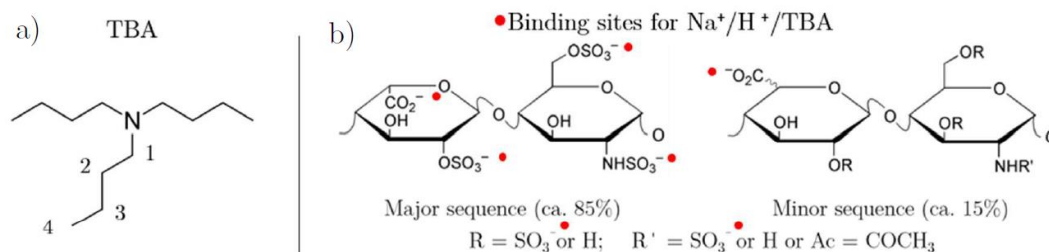
Figure 16: Ion exchange during the heparin-TBA modification process, A) The numbering reference of the methyl groups of tributylamine for NMR; B) The sites where ion exchange is expected to occur for heparin molecules [209].

1 g of HepNa$^+$ was dissolved in 100 ml of DI water (pH = 6.5). The solution, assisted with compressed air, was passed through a glass column (ID = 10 mm) packed with resin (7.5 g, 50W × 8 [H$^+$], 200-400 mesh, Dowex ®, Sigma Aldrich, RSA) at a flow rate of 5 ml/min. Subsequently, an additional 100 ml of DI water was passed through the same column to yield a 200 ml stock solution of heparin acid (HepH$^+$/DI water, 5 mg/ml, pH = 2.0).

HepTBA was produced by reacting 10 ml of TBA/methanol solution (80 mg TBA/ml MeOH) with 40 ml of HepH$^+$ stock solution (stirred for 2 hours). The MeOH was evaporated (RII Rotavapor Buchi, 122 mbar, 40 °C, 60 min) until a volume of 40 ml remained. The unreacted TBA was subsequently removed by liquid-liquid extractions with hexane (3 × 100 ml). Finally, the HepTBA/DI water solutions were freeze-dried for 48 hours to obtain a white powdery substance.

2.2.1 Nuclear magnetic resonance spectroscopy

The compounds were prepared by dissolution (4 mg/mL) and microfiltration (0.45 μm) in heavy water (D2O). A spectrometer (Bruker DRX-400, 10 s recycle delay. 128 scans) was used to record the Nuclear Magnetic Resonance (NMR) spectra at RT. The signals were processed for baseline subtraction, phase correction and numerical integration (MestReNova, v11.0, Spain).

2.3 Electrospinning and cast film solution preparation

The mass of polymers, solvents, drugs and scaffolds were measured with a 4-decimal precision balance (MS204S, Mettler Toledo AG, Greifensee, Switzerland) unless specified otherwise.

2.3.1 Polymer solution preparation for electrospinning

All solutions for electrospinning were prepared by magnetic stirring overnight at RT in glass test tubes or Pyrex® bottles. Solutions were removed from the stirrer 30-60 minutes prior to electrospinning, to equalise minimal heat generated and to remove air bubbles before transferring the solutions to syringes for processing. All solution concentrations were expressed as a weight-by-weight percentage (%wt/wt) for polymer mass to total solution mass unless specified otherwise.

Incorporated drugs (HepNa$^+$, HepTBA) were expressed as a weight percentage of the total polymer mass. Drugs were mixed into the volume of solvent (magnetic stirring, 60-90 min) until completely dissolved. The appropriate mass of polymer was then added and the solution was placed back on the magnetic stirrer overnight to obtain the final solution.

2.3.2 Polymer film preparation

DP30 polymer films were prepared by solution casting (n = 2) from 5 wt% DP30 in chloroform mixed on a magnetic stirrer overnight. 5 ml of the solution was poured into a 6 cm glass petri dish, covered with filter paper to minimise exposure to dust particles and placed in the fume hood for 24 hours. The cast films were submerged in distilled water for 30 seconds to lift the films from the petri dish and placed in the vacuum oven (48 hours, RT) to remove solvent and water.

2.4 Experimental setup for electrospinning
2.4.1 General setup

The experimental setup (Figure 17) for electrospinning scaffolds consisted of a previously custom-designed rotation and translation stage with adjustable speed settings and a humidity control unit. The electrospinning rig consisted of the following components:

- A melamine cabinet (electrospinning chamber) with sealed glass doors.
- Two high voltage power supplies (a positive ES30P-5W power unit and a negative ES30N-5W power unit, Gamma High Voltage Research, Ormond Beach, USA).
- A 0.067" stainless steel 304V rod (Small Parts Inc., Logansport, USA).

- Two syringe pumps (SE200 & SE400B, Fresenius SE & Co. KGaA, Bad Homburg, Germany).
- A 6 cm x 6 cm stainless steel base plate.
- Blunt needles (single/coaxial, process dependent).
- Syringes (20 ml Inkjet® Luer Solo, B Braun AG, Melsungen, Germany).
- PTFE tubing (OD = 4mm and ID = 2mm, 3D Printing Factory Pty (Ltd)., RSA).
- A stainless steel mandrel (d = 25 mm / 2.6 mm).
- An Arduino Mega 2560 microcontroller (Communica, RSA).
- Two NEMA stepper motors (23HSX-102A, 12 V, 1 A, Blantech Technology Supplies C.C., RSA; and RS Pro 191-8362, 12 V, 0.6 A, RS Components, UK, respectively).
- Two digital stepper motor drivers (Geckodrive G203V, Geckodrive, Santa Ana, USA).
- A low voltage power supply (8A, 12V, Communica, RSA).
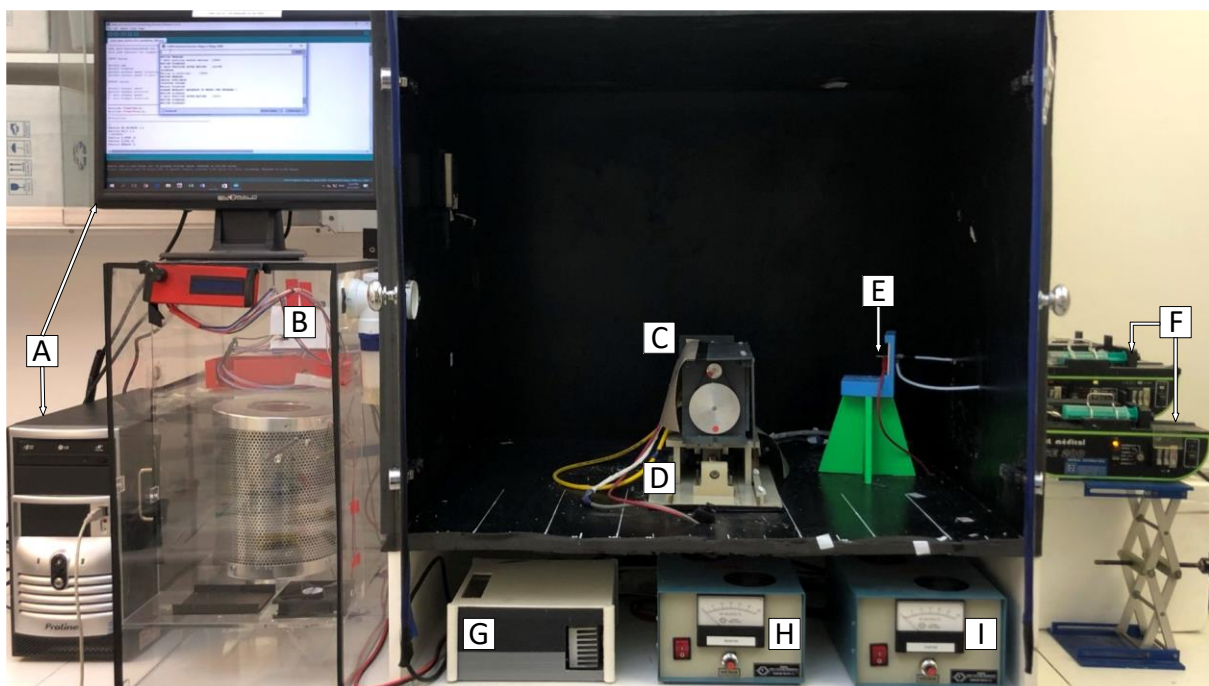
Figure 17: Electrospinning rig general setup. A) Serial monitor for translational and rotational speed input. B) Humidity control unit. C) Negatively connected rotating mandrel stage. D) Translational stage. E) Positively connected needle. F) Syringe pumps. G) Control unit containing Arduino microcontroller. H) Negative power supply. I) Positive power supply.

Briefly, the syringe pumps (Figure 17F) fed the polymer solution to the needle tip via PTFE tubing at a constant flow rate (0-4 ml/h). The needle (Figure 17E) was connected to the base plate which was positively charged (0-20 kV) and the rotating mandrel was negatively charged (0-10 kV). The two stepper motors were connected to digital stepper drivers controlled by the Arduino Mega 2650 microcontroller (Figure 17G) and controlled the translating (Figure 17D) and rotating stages (Figure 17C). The microcontroller received inputs from the serial user interface on the computer (Figure 17A) for the rotational speed of the mandrel (in *RPM*), the translation distance (in *mm*) and translating speed (in *mm/min*) of the translating axis which was used as the output of the stepper motors. The hardware components were powered by the 8 A, 12V power supply.

A humidity control unit (Figure 17B) for regulating the humidity in the electrospinning chamber consisted of the following components:

- An advanced Air Carbon Filter, 4" × 12" size, 200 CFM flow rate (Futurama, RSA).
- A desiccant silica gel filled filter (2 – 5mm beads, Silisorb™ Evirogel, Zantech, RSA).
- A nebuliser (MB-80E-01-H, TDK Corporation, Digi-Key, USA).
- A humidity sensor (Adafruit SHT31-D, Communica, RSA).
- An Arduino Uno microcontroller (Humidity_Control.ino, Communica, RSA).
- Three high-speed fans (10 cm × 10 cm, 12V DC, 0.35 A, Communica, RSA).
- A low voltage power supply (8 A, 12V, Communica, RSA).
- An LCD screen (16 × 2, IIC/I2C/TWI, Communica, RSA).

Briefly, the activated carbon filter was used for removal of solvent vapour, the desiccant silica gel filled filter for removal of moisture from the air (thus reducing the relative humidity) and the nebulizer for increasing the relative humidity as required. The humidity sensor was connected to the Arduino microcontroller which displayed the current relative humidity and temperature as well as the relative humidity setpoint on the LCD screen. The temperature and relative humidity displayed were verified using a thermo-hygrometer (Testo 175 H1 – 2 channel data logger, Testo South Africa, RSA).

2.4.2 Coaxial needle fabrication

Custom coaxial needles were designed (Figure 18A) and fabricated for coaxial electrospinning. After initial prototyping with plastic needles of various gauges, the optimum combination for stable coaxial electrospinning was found to be a 17 G (ID = 1.07 mm) shell and 24 G (ID = 0.34 mm) core needle with a 16 G side-feed needle. The stainless steel hypodermic needles (Glovtech CC, RSA) were blunted and filed to specific lengths so that there was no protrusion of the core needle and the hole for the side-feed needle was drilled using a drill press. The assembly was then fixed with steel epoxy (Steel Quickset, Pratley®, RSA) as illustrated in Figure 18B and C. Detailed computer-aided design drawings are included in Appendix A.
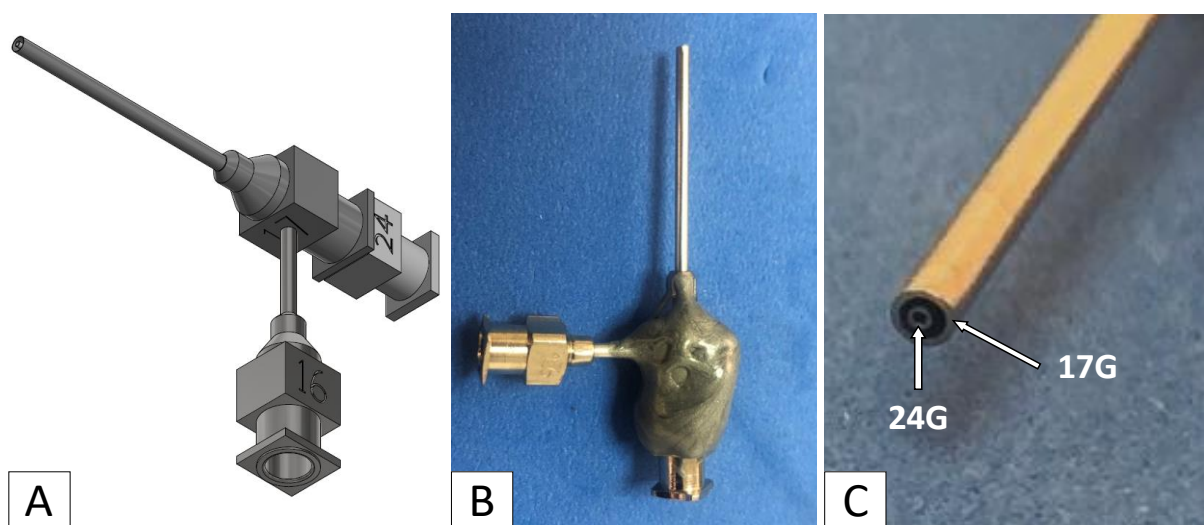
Figure 18: Custom made coaxial needles: A) CAD model. B) Side view and C) closeup of the physical model.

2.5 Electrospinning of degradable polyurethane scaffolds

Scaffolds were electrospun to investigate the effects of coaxial incorporation of heparin/water-soluble cores in DP30 fibres on the morphological, mechanical and thermal properties as well as the drug release and degradation response compared to conventional and blend electrospinning. Following extensive initial iteration of parameter combinations (described in Appendix C), the parameters that were used throughout the study, unless otherwise stated, are listed in Table 6. These parameters were selected to enable the best possible comparison between scaffold types due to similarity in solution type.

Table 6: Constant electrospinning parameters.

Parameter	Value
General	
DP30 concentration and solvent	22% wt/wt, Chloroform ($CHCl_3$)
Mandrel diameter	25 mm
Relative humidity (rH)	35 %
Translation speed	2 mm/s
Translation distance	10 cm
Duration	90 min
Coaxial specific	
Needle size	17 G × 24 G
Mandrel rotational speed	70 RPM
PEO (400kDa) solvent ratio	DI water: Ethanol (60:40)
Conventional specific	
Needle size	21 G
Mandrel rotational speed	125 RPM

Three sets of coaxially electrospun scaffolds were produced, all with PEO cores: HiHepCA – a group with a high heparin content (0.6 wt% HepNa$^+$); LoHepCA – a group with a low heparin content (0.3 wt% HepNa$^+$); and NoHepCA – a group with no heparin incorporated (control). Various quantities of heparin were incorporated to investigate the effect of increased HepNa$^+$ on the scaffold characteristics and drug delivery response. Furthermore, the group with pure PEO cores (containing no heparin) was used to establish the effect of heparin addition on the electrospinning process. DP30 scaffolds (HTBlend) with incorporated HepTBA (0.6 wt%) were produced by blend (dissolving the HepTBA into the solution) electrospinning to investigate the effect of the incorporation method on drug release. Lastly, a set of DP30 scaffolds (DP30CTRL) were produced by conventional electrospinning to act as a control group.

The parameters used for each group is specified in Table 7. All produced scaffolds were placed in a vacuum oven overnight (RT) to remove excess solvents. A summary of the produced scaffolds and their applications in subsequent studies is provided in Table 8.

Table 7: Electrospinning parameters for scaffold development.

	Coaxial electrospinning							
Group code	**PEO (400kDa) core conc. (% wt/wt)**	**HepNa$^+$ conc. (% wt/ wt PEO)**	**TCD**	**Shell flow rate (ml/h)**	**Core flow rate (ml/h)**	**Positive voltage-needle (kV)**	**Negative voltage-target (kV)**	**Sample size (n)**
HiHepCA	3.75	38.5	29	2.2	0.4	16.5	-3.0	5
LoHepCA	3.50	27.5	27	2.2	0.3	16.0	-2.5	5
NoHepCA	3.75	-	30	2.6	0.5	15.5	-1.0	2
	Conventional electrospinning							
Group description	**HepTBA conc. (% wt/ wt DP30)**	**TCD**		**Flow rate (ml/h)**		**Positive voltage-needle (kV)**	**Negative voltage-target (kV)**	**Sample size (n)**
DP30CTRL	-	30		2.4		11.5	-1.0	5
HTBlend	0.6	35		2.4		11.0	-1.0	4

Table 8: Summary of the electrospun sample groups (heparin content, PEO content and applications in studies).

Group code	Group description	Heparin content (wt / wt$_{total}$)	PEO content (wt / wt$_{total}$)	Study						
				Morphological characterisation	Water contact angle	Mechanical characterisation	DSC	Heparin quantification	Heparin activity	Degradation
HiHepCA	High heparin coaxial	0.6 % HepNa+	2.25 %	✓	✓	✓	✓	✓	✓	✓
LoHepCA	Low heparin coaxial	0.3 % HepNa+	1.05 %	✓	✓	✓	✓	✓	✓	✓
NoHepCA	No heparin coaxial	-	-	✓	-	-	✓	✓	-	-
DP30CTRL	DP30 control	-	-	✓	✓	✓	✓	✓	-	✓
HTBlend	HepTBA/ DP30 blend	0.6 % HepTBA	-	✓	✓	✓	✓	✓	✓	✓

2.6 Characterisation of scaffold morphology

2.6.1 Scanning electron microscopy (SEM)

Dried samples were cut and adhered to metal stubs using double-sided carbon tape to observe the fibre morphology of the luminal, abluminal and cross-sectional surface, and subsequently sputter-coated with gold (60 s, 1.2 kV, 20 – 25 mA, Polaron SC7640, Quorum Technologies, England). Under constant high-vacuum observation conditions (15.0 kV, WD 10.8, Std.-PC 60, HighVac) at various magnifications, the images were acquired with a JEOL JSM-IT200 Scanning Electron Microscope (SEM, JEOL Ltd., Tokyo, Japan) using the designated InTouchScope™ computer interface (JEOL Ltd.).

2.6.2 Fibre diameter, fibre orientation and pore size

Scanning electron micrographs of the luminal (n = 3) and abluminal (n = 3) surfaces from three sections per electrospun sheet were used for 2D image processing. The selected magnification was ×500 for DP scaffolds. The average fibre diameter, fibre orientation index and equivalent pore size were determined from these images (n = 12 per group, 4 per sample × 3 for the number of electrospun sheets) using an image analysis software, ImageJ (version 1.53a, National Institutes of Health, USA) with a plugin, DiameterJ 1-018. The plugin generated a .csv file with the data as an output.

After cropping the images captured by SEM, they were placed in the same folder and segmented with the DiameterJ Segment plugin by selecting 'Stat. Region Merged' and 'Mixed' for the segmentation algorithm. The best-segmented image of each SEM image was manually chosen (visual comparison) and analysed with the DiameterJ 1-018 plugin.

The following settings were selected when running the DiameterJ 1-018 plugin: orientation analysis (OrientationJ), convert pixels to real units (yes), length of scale bar (207 pixels), length of scale bar (50 microns), identify location of specific radius (no), min fibre radius (1 pixel), max fibre radius (255 pixels), analyse more than one image (yes), and combine analysis from all images with DiameterJ (yes). The length of the scale bar (in pixels) was determined by zooming in on the scale bar, selecting the 'straight line' function in ImageJ and drawing a line from one end to the other of the scale bar. The length of the scale bar (in pixels) is displayed under ImageJ's toolbar.

The OrientationJ Measure plugin runs simultaneously with the DiameterJ 1-018 plugin by selecting 'OrientationJ' from the 'Orientation Analysis' section's dropdown list with the following settings: No pre-filter, Ellipse thickness (0.5), Ellipse opacity (100), Ellipse colour (255: 0: 0), Area opacity (50), Area colour (128: 128: 0). The Orientation Index (OI, $0 \leq OI \leq 1$) quantifies the fibre alignment of each scaffold, where an OI approaching zero ($\rightarrow 0$) indicates randomly aligned fibres (Figure 19B) and an OI of unity (= 1) exhibits perfectly aligned fibres (Figure 19A).
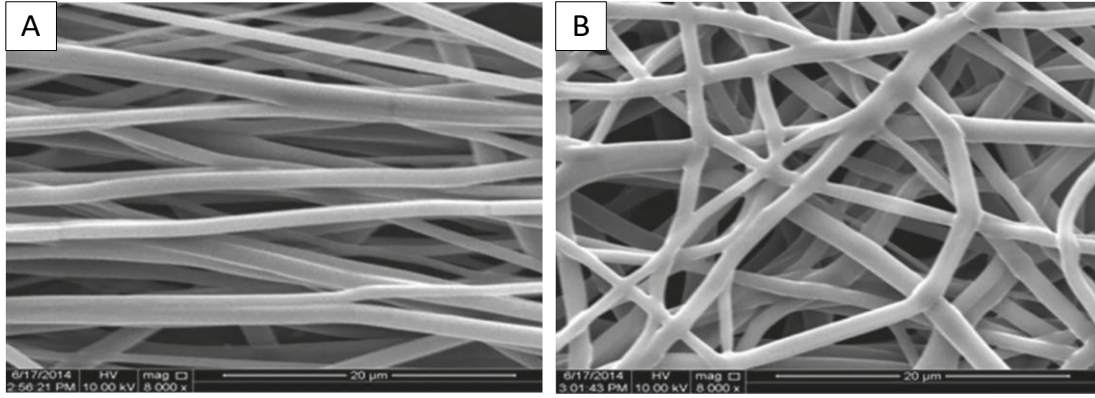
Figure 19: A) Aligned fibres. B) Randomly oriented fibres.[280]

2.6.3 Porosity

The porosity of scaffolds can be defined as a function of the volume of the fibres and the total volume of the scaffold as expressed in Equation 1. It is however not feasible to measure such small volumes directly, therefore previous researchers have modified the definition to acquire Equation 2 [206, 210, 212]. Gravimetric liquid intrusion measurement was used to determine these quantities by weighing punched scaffold disks (d = 6 mm, n = 4) in air and submerged in heptane (ρ = 0.68 g/cm^3) to eliminate all air from the scaffold (Figure 20). A 5 decimal precision balance (XS105 DualRange balance, Mettler Toledo AG, Greifensee, Switzerland) and an Adam density determination kit (AAA250L, Adam Equipment Inc, Danbury, USA) were used.

$$\Phi = 1 - \frac{V_{Fibres}}{V_{Total}} \qquad\qquad Eq. \quad 1$$

$$\Phi = 1 - \frac{m_{sample,air} - m_{sample,heptane}}{\rho_{heptane} \times V_{Total}} \qquad\qquad Eq. \quad 2$$

With $m_{sample,air}$ and $m_{sample,heptane}$ representing the mass of the sample in air and the mass of the sample submerged in heptane. V_{Total} is acquired through dimensional measurement, $V_{Total} = \pi(d/2)^2 \times t$, where t is the thickness of the sample.
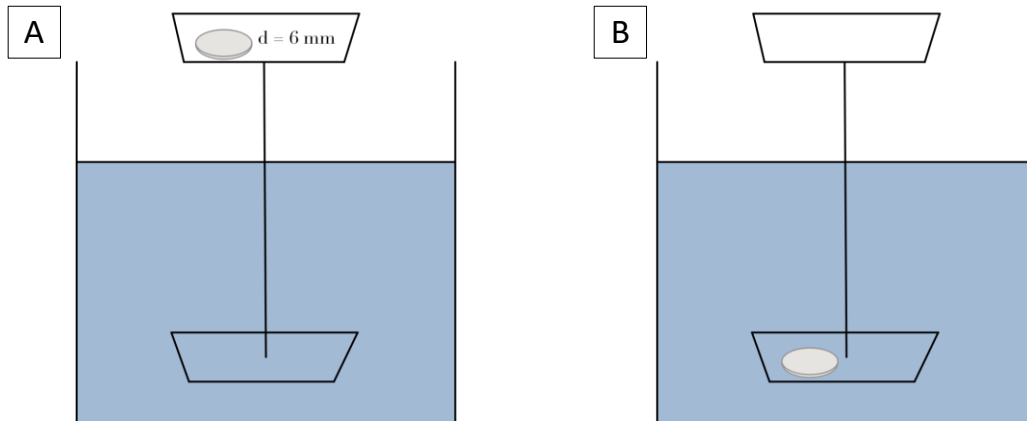
Figure 20: Porosity measurement. A) Weighing the scaffold mass in air. B) Weighing the scaffolds mass in heptane.

2.6.4 Core-shell morphology validation

The core-shell fibre structure of coaxially electrospun fibres was confirmed by immersing grafts into liquid nitrogen (to reduce plastic deformation during cross-sectioning) and rapidly cutting with a scalpel to generate a cross-section where the layer edges will be visible on the SEM. The samples were then placed in 500 ml DI water: ethanol (90:10) and placed on a magnetic stirrer to wash out some of the water-soluble core polymer. The aqueous solution was replaced with fresh solution every 8 hours for 48 hours. The samples were then dried in the vacuum oven overnight and the cross-section was observed by the SEM.

2.7 Water contact angle

The water contact angle (θ) was determined by using the low-bond axisymmetric drop shape analysis (LB-ADSA) method based on the fitting of the Young-Laplace equation to image data [281]. Briefly, a 3 µl droplet of DI water was pipetted onto the luminal and abluminal surfaces of cast films and electrospun samples (10 × 10 mm, n = 3) and an image was taken with a charge-coupled device (CCD) camera (Techgear Eaglescope, China). The image was imported to ImageJ (version 1.53a) and the image type was converted to grayscale (32-bit). Thereafter, the 'Drop Analysis – LB-ADSA' plugin was used to determine the contact angle by changing the 'Drop parameters' (b, x0, y0, h, d) until the Young-Laplace equation (indicated in green) fit the drop as illustrated in Figure 21.
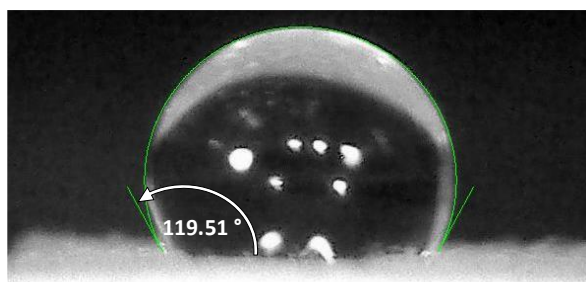
Figure 21: Contact angle calculation (Young-Laplace equation fitting indicated in green).

2.8 Polymer swelling characterisation

The swelling of DP30 in water was characterised by determining the mass increase of cast films submerged in water over time. Punched disks (d = 6 mm) of cast DP30 films (n = 4) with a recorded mass were prepared in sealed glass tubes (immersed in 20 ml of DI water). The samples were removed at designated time points (12 h, 24 h, 36 h, 48 h, 7 days) and lightly dabbed on a paper towel to remove surface wetness. Thereafter, the mass was recorded and samples were placed back in the tubes.

2.9 Mechanical characterisation of electrospun scaffolds

The mechanical properties of samples were characterised by using a tensile tester (Instron 5544, 10 N loadcell, Norwood, USA) with Merlin (version 5.04) as the user interface. The thickness of samples was measured using a digital thickness gauge (Mitutoyo PK-0505 CPX 700-118-20, Mitutoyo Corporation, Kanagawa, Japan).

2.9.1 Circumferential and longitudinal tensile testing

Dogbone-shaped samples (gauge size of 20 × 3 mm) were prepared of sample groups and subsequently clamped and tested in the longitudinal (n = 3) and circumferential (n = 3) direction using the tensile tester (Figure 22).

The ultimate tensile strength (UTS) was defined as the stress at the point of global maximum stress on the stress/strain curve and the maximum elongation (ε_{max}) as the corresponding strain at that point. The Youngs modulus (E_y) was approximated as the slope of the longitudinal stress/strain curve until 10 % stress. The samples were tested until failure under physiological conditions as established by Tai, Salacinski [282], at a strain rate of 66 mm/min, which is based on the compliance of a healthy blood vessel (8 %/100mmHg) and a heart rate of 72 bpm [283, 284].

Dry and surface-wet testing was performed on samples of the control group (DP30 control) to establish the effect of surface wetness on the tensile response. For surface-wet testing, samples were submerged in PBS at 37±2°C for 10 minutes, lightly patted with a paper towel to remove excess fluid and then tested. All other groups were only tested under surface-wet conditions as it is a better representation of physiological conditions than dry testing.
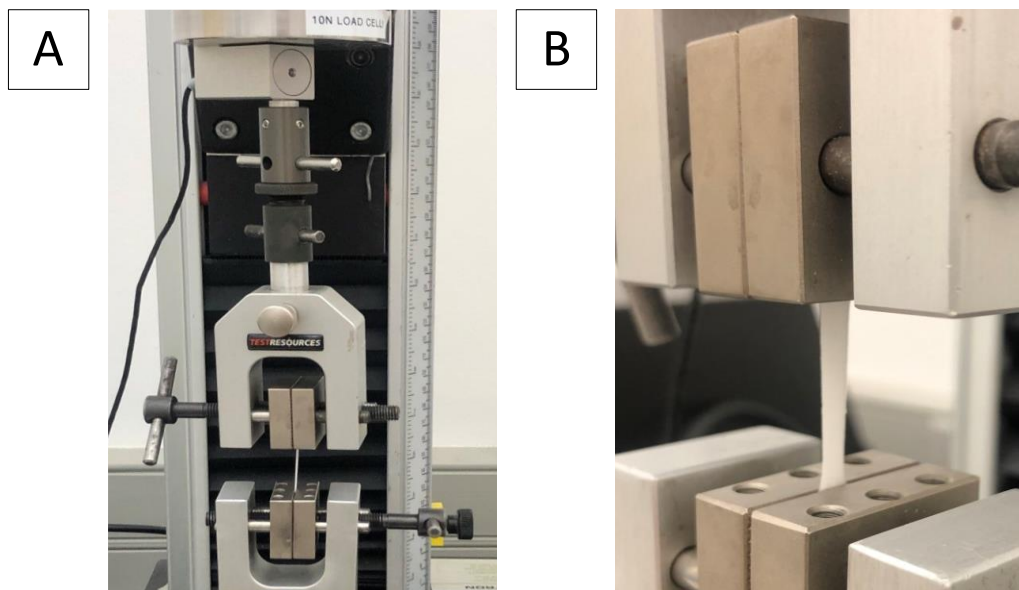
Figure 22: Mechanical characterisation. A) Instron setup used for mechanical testing of samples. B) Exploded view of clamping of samples.

After testing the force-displacement data was logged in a .raw file and imported into Python (Spyder IDE v4.1.4., Anaconda Navigation). The custom Python script processed the data as stress-strain plots, determined the UTS, ε_{max} and E_y; and exported it to an Excel workbook.

2.9.2 Suture retention testing

Suture retention tests were conducted as specified in ISO 7198: 2016 using the "straight-across" procedure [285]. Samples (longitudinal and circumferential, n = 3) were prepared as cut dogbone samples of 3 mm in width and approximately 15 mm in gauge length. As illustrated in Figure 23A, the sample's shoulder was clamped to the fixed bottom clamp of the

tensile tester and a single bite of 7-0 polypropylene suture (Prolene, BV-1 needle, Ethicon, USA) was placed centrally, 2 mm from the end of the sample and looped around the customised top clamp. Once the loop had minimal slack, it was pulled out at a constant rate of 66.0 mm/min (Figure 23B) to determine the maximum force (N) at specimen failure (characterised by suture pull out).
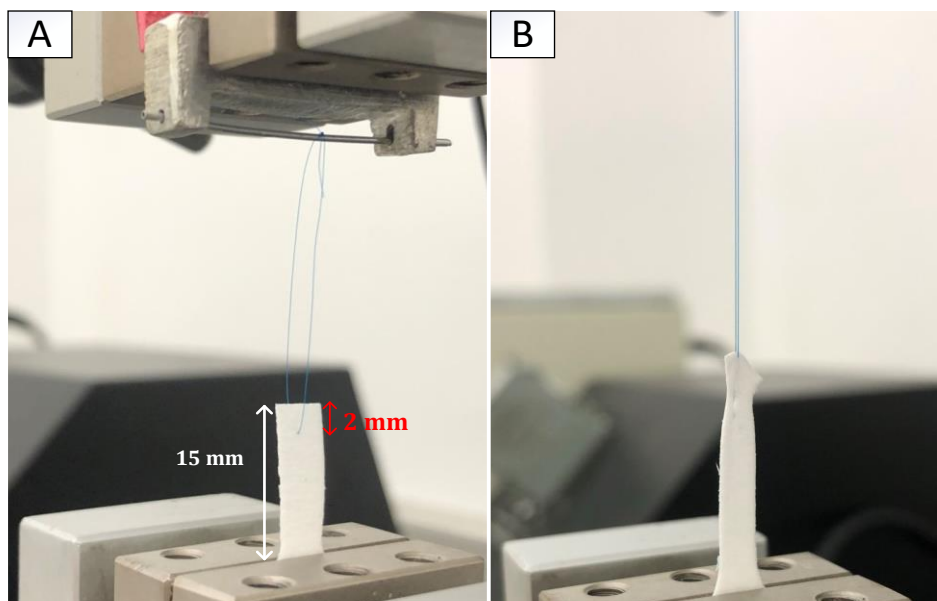
Figure 23: Suture retention tests. A) Setup and specimen dimensions. B) Illustration of pull out response.

2.10 Differential scanning calorimetry (DSC)

A differential scanning calorimeter (DSC, DSC 4000, PerkinElmer, USA) was used to determine the thermal properties of sample groups. All tests were run with nitrogen as purge gas at a flow rate of 20 ml/h and pressure of 400 kPa.

The DSC was calibrated using a calibration sample kit (N519-0762, PerkinElmer). It was first calibrated with Indium and subsequently with Zinc over a specified temperature range against a reference. The temperature onset value of Indium and Zinc and the heat flow (ΔH) of Indium were inserted as temperature and heat flow calibration values respectively. Thereafter, a quick run was performed with no samples inserted (both stages empty) to ensure that the DSC was warmed up. The parameters of these initial processes are specified in Table 9.

A known mass (5-10 mg) of each sample was placed in a 50 µL aluminium pan (BO143017, PerkinElmer) and sealed with an aluminium cover using a PerkinElmer crucible sealing press. The sealed sample was inserted into the DSC chamber at room temperature then subjected to a range of isothermal steps and thermal scans. A temperature rate of 10 °C/min was used for all temperature scans. All sample runs contained an initial isothermal step followed by an increasing temperature scan step, isothermal step, decreasing temperature scan step and ended with an isothermal step. The specifics of each scan are tabulated in Table 10. Additionally, a DP30 powder sample at 170 °C was quenched in liquid nitrogen (LN2) after an increasing temperature scan and subsequently subjected to a full run.

Table 9: DSC calibration and quick pre-test run. IT – Isothermal, TS – Thermal scan.

Process	Reference stage	Sample stage	Thermal range	Temperature Rate
Indium calibration	Ref. Pan	Indium (5.597 mg)	IT: 130 °C (1 min) TS: 130 °C – 170 °C	10 °C/min
Zinc calibration	Ref. Pan	Zinc (2.491 mg)	IT: 370 °C (1 min) TS: 370 °C – 430 °C IT: 430 °C (1 min)	10 °C/min
Quick pre-test run	Empty	Empty	IT: -30 °C (4 min) TS: -30 °C – 180 °C IT: 180 °C (4 min) TS: 180 °C – 30 °C IT: -30 °C (4 min)	20 °C/min

Table 10: Thermal scan per sample group. IT – Isothermal, TS – Thermal scan.

Sample	Step 1 (IT)	Step 2 (TS)	Step 3 (IT)	Step 4 (TS)	Step 5 (IT)
DP30 raw material	-75 °C (5 min)	-75 °C – 170 °C	170 °C (5 min)	170 °C – -75 °C	-75 °C (5 min)
PEO (400kDa) raw material	-75 °C (5 min)	-75 °C – 120 °C	120 °C (5 min)	120 °C – -75 °C	-75 °C (5 min)
HepNa$^+$, HepTBA	-75 °C (5 min)	-75 °C – 300 °C	300 °C (5 min)	300 °C – -75 °C	-75 °C (5 min)
All electrospun DP30 scaffolds	-75 °C (5 min)	-75 °C – 170 °C	170 °C (5 min)	170 °C – -75 °C	-75 °C (5 min)
DP30 raw material- quenched from 170°C	-75 °C (5 min)	-75 °C – 170 °C	170 °C (5 min)	QUENCHED IN LN2	
	-75 °C (5 min)	-75 °C – 170 °C	170 °C (5 min)	170 °C – -75 °C	-75 °C (5 min)

DSC results were processed and analysed on the Pyris software (PerkinElmer, USA) as *Heat flow vs Temperature* curves (thermograms) to determine enthalpy changes (ΔH – area under the curve) and temperatures (peak values) of thermal transitions. The data was exported as a raw data file and plotted in Matlab.

2.11 In vitro heparin release and activity study

An in vitro heparin release study was performed by incubating scaffold strips in buffer solution and quantifying the release at specified time points by colourimetric assay and the activity of the heparin eluted from scaffolds was subsequently determined by thromboelastography (TEG).

2.11.1 Heparin quantification

Samples (cut to 8 × 12 mm strips, n = 5) were weighed and subsequently prepared in sealed plastic tubes (immersed in 1 ml PBS) and incubated at static conditions (37 °C, Heraeus Instruments oven, Lasec, RSA). At selected time points (1, 2, 3, 4, 7, 14, 21 and 42 days), the samples were removed from the tubes (the elution fluid stored as eluates in the same tube), rinsed in PBS and placed in a new tube with fresh PBS.

A 3-methyl-2-benzothiazolinone hydrazone hydrochloride (MBTH)-assay was used to analyse eluates for heparin (HepNa$^+$/HepTBA) content. Each eluate (250 µl) was reacted (sonicated, 30 min at RT) with nitrous acid solution (500 µl, 0.025 M HNO$_2$, 1 M HCL) before the addition of ammonium sulfamate solution (250 µl, 1 M H$_6$N$_2$O$_3$S). The mixture was diluted with sodium chloride solution (300 µl, 1M NaCl) and MBTH solution (500 µl, 0.011M) and incubated (15 min at 50°C). Ferric chloride solution (500 µl, 0.031M FeCl$_3$) was subsequently added to the mixture without cooling and was incubated again (20 min at 50°C).

The resulting colourimetric solutions were transferred to disposable cuvettes and placed in a spectrophotometer (UV-1601PC, Shimadzu, Kyoto, Japan) for measuring their absorbance with UV spectroscopy (660 nm wavelength). A standard absorbance curve (Figure 24) for heparin was generated at known concentrations (0, 0.002, 0.005, 0.01, 0.02, 0,.05, 0.1, 0.2 mg/ml) to calculate the concentration (*mg/ml*) of released heparin for each sample. The released concentrations were normalised with the initial scaffold masses to determine the theoretical drug content (mg Hep/g scaffold). The release curves of heparin were expressed as cumulative and instantaneous delivery rates; and normalised against control groups DP30CTRL and NoHepCA as appropriate and where applicable.
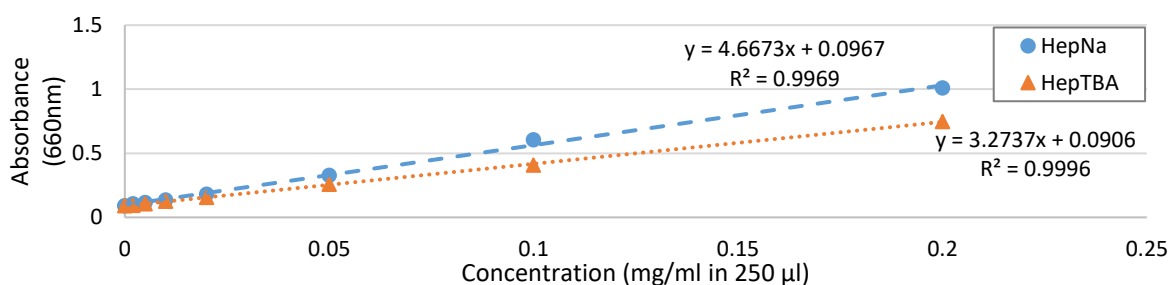
Figure 24: Typical absorbance curves for heparin concentration calculations.

2.11.2 Thromboelastography

The anti-thrombotic activity of pure heparin (HepNa$^+$ or HepTBA) solution and heparin eluates from electrospun scaffolds was analysed using a TEG®5000 thromboelastograph hemostasis analyser system (Haemonetics Corporation, Boston, USA). Before testing treatment groups, all sample channels (n = 4, two analysers with two channels each) were tested and approved for their accuracy by running an e-test.

The selected blood treatments for TEG® analysis (summarised in Table 11) included pure PBS solution, pure heparin solutions (HepNa$^+$ or HepTBA, 0.01 mg/ml in PBS) and heparin eluted from the electrospun scaffolds after 48 hours of in vitro incubation (PBS at 37°C). The eluates (with concentrations determined by MBTH-assays) were diluted with PBS if necessary to acquire the concentration in Table 11.

In order to perform a TEG, whole human blood was required. Voluntary donors were approached to donate blood samples (HREC REF: 491 / 2021, ethics approval letter – Appendix D; UCT access to staff for research purposes approval – Appendix E). A 2 syringe technique was used as blood had to be free-flowing to avoid contamination with tissue thromboplastin. 2 ml of blood was drawn into a syringe and immediately discarded and thereafter a further 3 ml of blood was collected into a citrated Vacutainer® tube (coagulation sodium citrate 3.2%, 9NC, BD Medical, RSA) and set up in the TEG within 1 hour.

Table 11: Heparin treatments for whole blood TEG analysis.

Treatment (110 µl)	Control	Concentration (mg/ml)	Sample size (n)
PBS	Yes	N/A	2
HepNa$^+$ (in PBS)	Yes	0.01	2
HepNa$^+$ electrospun eluate (LoHepCA)	No	0.01	2
HepNa$^+$ electrospun eluate (HiHepCA)	No	0.01	2
HepTBA (in PBS)	Yes	0.01	2
HepTBA electrospun eluate (HTBlend)	No	0.01	2

110 µl of the blood treatment fluid along with 890 µl of citrated blood was transferred to a Kaolin-coated vial (40 µl Kaolin, TEG® Hemostasis System, Haemonetics Corporation) and carefully inverted ten times. The mixture (340 µl) was then placed inside a pre-warmed (37°C) disposable non-heparinased TEG® analyser cup (Clear, Haemonetics Corporation) containing 20 µl of calcium chloride (0.2M $CaCl_2$, TEG® Hemostasis System, Haemonetics Corporation). The oscillating blood clotting process (parameters illustrated and described in Figure 25 and Table 12) was recorded with the provided software (TEG® Analytical Software v. 4.2.3, Haemonetics Corporation). A summary of all blood treatment group's responses was plotted in MATLAB. One-tailed, equal variance t-tests were used to determine significance between groups.

Table 12: Thromboelastography parameters [286, 287].

Parameter	Definition / Significance	Symbol
Reaction time	Time until start of clot formation (waveform breaches 2mm above the baseline)	R
Kinetics / Clot formation time	Time until clot reaches a fixed strength (from 2 to 20 mm above the baseline)	K
Angle	Rate of clot development (slope between R and K)	α
Maximum amplitude	Clot strength (maximal firmness)	MA
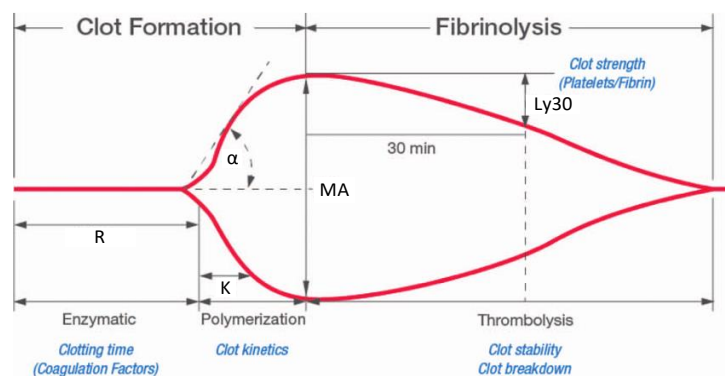
Figure 25: Illustration of recorded TEG parameters [288].

2.12 Degradation study

The rate of hydrolytic degradation was characterised through in vitro strength loss and in vitro mass loss over a 6-week period in physiological aqueous solution. The degradation of the samples were further investigated by performing DSC analysis on degraded samples. Dogbone shaped samples were prepared similarly to those for mechanical testing in Section 2.9.1 and their initial mass (m_0) were recorded.

2.12.1 Mechanical strength loss

Samples (n = 3 for each time point) from DP30CTRL, HTBlend, HiHepCA and LoHepCA were prepared in sealed glass tubes (immersed in 15 ml PBS) and incubated at static conditions (37 °C, Heraeus Instruments oven, Lasec, RSA). At selected time points (7, 14, 21, 42 days), the samples were removed and the longitudinal and circumferential mechanical properties were tested using the same method described in Section 2.9.1.

2.12.2 Mass loss

To investigate mass loss (%) over time, the samples that were mechanically tested in the abovementioned mechanical loss study were rinsed in DI water (to remove any PBS salts), dried (24 hours in the fume hood at RT and then placed under vacuum). The samples were weighed until the same mass was recorded for two consecutive days (indicating that the samples are completely dry). The mass was then recorded as m_t, the mass at time point t. The mass loss percentage at each time point was expressed as:

$$\% \text{ Mass loss} = (1 - \frac{m_t}{m_0}) \times 100$$

Eq.   3

For further investigation of the mass loss over the 6-week period, the samples from the in-vitro drug elution study (Section 0) were also rinsed and dried as described above and weighed to determine their mass loss after 6 weeks.

2.12.3 Differential scanning calorimetry (DSC)

Thermal runs were performed as described in Section 2.10 on the dried degradation samples (3 and 6 weeks) as summarised in Table 13. The resulting thermograms were subsequently compared to those acquired from thermal analysis of Week 0 scaffolds (Section 2.10).

Table 13: DSC analysis of degraded samples.

Sample	Step 1 (IT)	Step 2 (TS)	Step 2 (IT)	Step 4 (TS)	Step 5 (IT)
Week 3 Degradation	-75 °C (5 min)	-75 °C – 170 °C	170 °C (5 min)	170 °C – -75 °C	-75 °C (5 min)
Week 6 Degradation	-75 °C (5 min)	-75 °C – 170 °C	170 °C (5 min)	170 °C – -75 °C	-75 °C (5 min)

2.13 Translational study

A pilot study was performed to investigate whether the electrospinning technique used could be translated from a large mandrel (25 mm) to a smaller mandrel (2.6 mm) to produce tubular

vascular grafts. The morphology of produced grafts was characterised by SEM analysis and porosity determination. Furthermore, the produced vascular grafts were mechanically tested to determine tensile properties as well as burst pressure and compliance.

2.13.1 Electrospinning of vascular grafts

Two sets of vascular grafts were produced by (i) conventional electrospinning of DP30 in chloroform – DP30CVG; and (ii) coaxial electrospinning with a shell solution of DP30 in chloroform and a core solution of heparin (HepNa$^+$) incorporated into PEO (400kDa) in DI water and ethanol – HepCAVG. DP30CVG and HepCAVG would respectively act as translations from DP30CTRL and LoHepCA. The solution parameters and the processing parameters that were held constant for all sample groups are listed in Table 14.

Table 14: Solution parameters and constant processing parameters.

Parameter	Value
Solution parameters	
Conventional electrospinning solution concentration	22% DP30/Chloroform (CHCl$_3$) wt/wt
Coaxial electrospinning shell solution concentration	22% DP30/Chloroform (CHCl$_3$) wt/wt
Coaxial electrospinning core solution concentration	27.5 wt% HepNa$^+$ / 3.5 % PEO(400kDa)/ Di Water: Ethanol (60:40) wt/wt
Constant processing and environmental parameters	
Mandrel diameter	2.6 mm
Translation speed	2 mm/s
Translation distance	10 cm
Duration	15 min
Relative humidity (RH)	30 %

Vascular grafts were electrospun with the group-specific parameters listed in Table 15. In order to remove whole grafts from the mandrel after spinning, the mandrel (with the vascular graft) was placed in the vacuum oven (RT) for 60 minutes and thereafter briefly dipped into ethanol (swelling agent) to facilitate the removal of the graft from the mandrel. The vascular grafts were then placed back into the vacuum oven overnight (RT) to remove the ethanol.

Table 15: Electrospinning parameters for translational study.

Group description	Needle size (G)	TCD (cm)	Mandrel speed (RPM)	Shell flow rate (ml/h)	Core flow rate (ml/h)	Positive voltage (kV)	Negative voltage (kV)	Sample size (n)
Conventional (DP30CVG)	21	30	150	2.1	-	10.5	-4.0	4
Coaxial (HepCAVG)	17 & 24	28	120	2.5	0.4	16.5	-3.0	2

2.13.2 Morphological characterisation of vascular grafts

The vascular grafts were observed via scanning electron microscopy and analysed in ImageJ as described in Sections 2.6.1 and 2.6.2. The porosities of the grafts were determined similarly to Section 2.6.3. Vascular grafts with recorded wall thicknesses were cut to 10 mm lengths, and weighed in air and submerged in heptane.

2.13.3 Mechanical characterisation of vascular grafts

The current method for tensile testing tubular vascular grafts was performed under the surface-wet testing conditions in Section 2.9.1. Required lengths and diameters were measured with a calliper and inserted into Merlin for cross-sectional area calculation.

2.13.3.1 Longitudinal tensile testing

Samples (n = 3) were cut to 30 mm length and longitudinally clamped to a gauge length of 10 mm between custom-made stainless-steel clamps with diamond patterned rubber grips (Figure 26) and tested at a strain rate of 66 mm/min until failure. The UTS, ε_{max} and E_y were determined by processing the force-displacement data as described in Section 2.9.1.
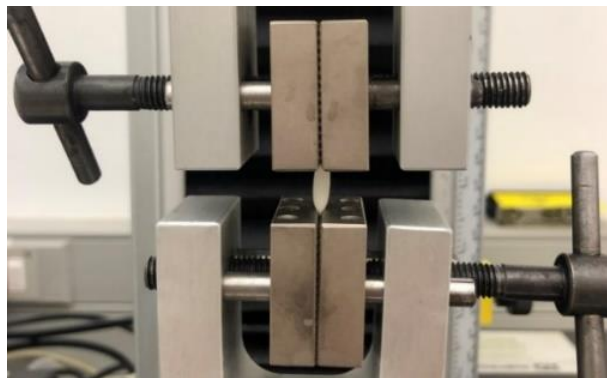
Figure 26: Longitudinal tensile testing of vascular grafts.

2.13.3.2 Circumferential tensile testing

Samples (n = 3) were cut to 5 mm tubular lengths and tested in the circumferential direction with a custom-made device (Figure 27) at a rate of 66 mm/min until failure.
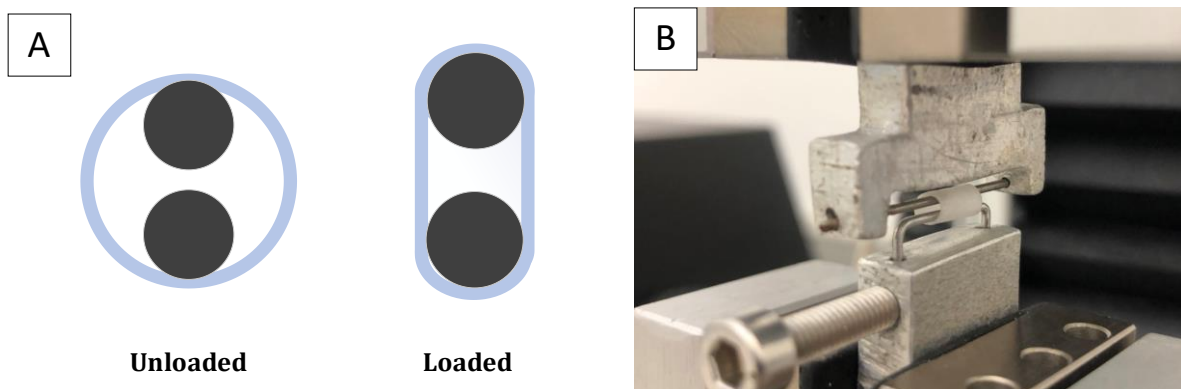
Figure 27: Circumferential testing of vascular grafts. A) Unloaded and loaded sample held by pins. B) Setup on the tensile tester.

The samples were held by two pins (OD = 1 mm, Figure 27A) and stretched to ensure the graft walls were near parallel but a load of less than 0.01 N was measured. This setup allowed for straight stretching with the walls parallel to each other as illustrated in Figure 27B. The force-displacement data was logged in a .raw file and imported into Python, where the custom Python script processed the data as stress-strain plots.

Hoop stress

The UTS in the circumferential direction is equal to the hoop stress in the wall of the tubular graft and thus the hoop stress was calculated using the circumferential force-displacement data and the following formula:

$$\sigma_{\text{hoop}} = \frac{F}{2 \times t \times w} \qquad \textit{Eq. \quad 4}$$

with σ_{hoop}, F, t and w representing the hoop stress (*MPa*), force (*N*), wall thickness (*mm*) and width (*mm*) of the graft, respectively.

Burst pressure

Thick-walled cylinder theory ($r/t < 10$) was applied to the hoop stress vs strain curve to approximate the theoretical burst pressure of grafts. A simplified version of Lame's theory was used which negates external pressure, radial and axial stresses and strains and assumes maximum hoop stress at point D_i. The theoretical burst pressure was defined as the pressure at the maximum hoop stress.

$$\sigma_{\text{hoop}} = P_i \times \frac{r_o^2 + r_i^2}{r_o^2 - r_i^2} \qquad \textit{Eq. \quad 5}$$

$$P_i = \sigma_{\text{hoop}} \times \frac{r_o^2 - r_i^2}{r_o^2 + r_i^2} \qquad \textit{Eq. \quad 6}$$

Where P_i, r_o and r_i are the internal pressure (*MPa*), outer radius (*mm*) and inner radius (*mm*), respectively. All pressures were also reported in mmHg. The thin-walled cylinder theory was used as a control method for determining the burst pressure:

$$P_i = \frac{\sigma_{\text{hoop}} \times t}{r_o} \qquad \textit{Eq. \quad 7}$$

Compliance

The compliance was estimated through modification of the standard compliance equation:

$$C_d = \frac{D_s - D_d}{(P_s - P_d) \times D_d} \times 10^4 \ [\% / 100 mmHg] \qquad \textit{Eq. \quad 8}$$

by replacing the diameters with the strain values based on the definition of strain:

$$D_x = D_0(\epsilon_x + 1) \ [mm] \qquad \textit{Eq. \quad 9}$$

yielding the equation for compliance as:

$$C_d = \frac{\epsilon_s - \epsilon_d}{(P_s - P_d) \times (\epsilon_d + 1)} \times 10^4 \ [\% / 100 mmHg] \qquad Eq. \quad 10$$

with the description of the symbols summarised in Table 16.

Table 16: Description of symbols for burst pressure and compliance calculations.

Symbol	Description	Unit
C_d	Diametral compliance	$\% / 100 \ mmHg$
D_s	Systolic diameter	mm
D_d	Diastolic diameter	mm
P_s	Systolic pressure	MPa
P_d	Diastolic pressure	MPa
D_x	Equivalent diameter at the given strain	mm
ϵ_x	Strain at the equivalent diameter	-
ϵ_s	Systolic strain at the systolic hoop stress	-
ϵ_d	Diastolic strain at the diastolic hoop stress	-

The equivalent diastolic and systolic hoop stress, σ_d and σ_s, were then determined using Equation 5 at internal pressures of 80 mmHg ($P_d = 1.07 \times 10^{-2}$ MPa) and 120 mmHg ($P_s = 1.6 \times 10^{-2}$ MPa). Thereafter, the corresponding strains were determined as depicted in Figure 28A by interpolating the stress-strain curve values using a custom MATLAB script (Appendix G). The strain values were substituted into Equation 10 to equate C_d for each tested sample. An example of the resulting MATLAB plot is provided in Figure 28B.
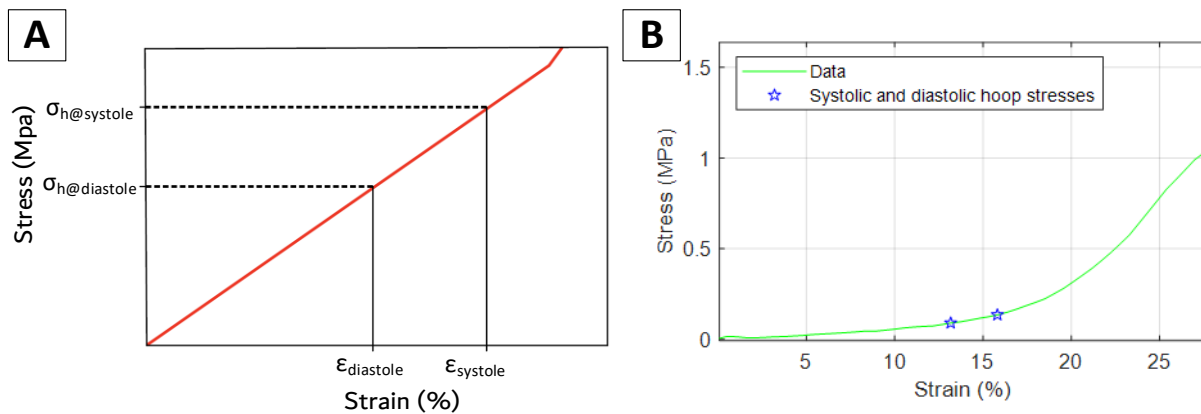
Figure 28: A) Illustration of compliance calculations to obtain the equivalent systolic and diastolic strain. B) Example of the resulting MATLAB plot.

2.14 Statistical analysis

All data was expressed as mean±standard deviation unless otherwise specified. One-way ANOVA was used to analyse the variance and significance (P-value) of data sets and two-tailed, equal variance t-tests were used if datasets were found to be significant. $P < 0.05$ between data sets was assumed to be significant. The plotting of graphs and computations were performed on Microsoft Excel unless stated otherwise.

3 Results and discussion

This chapter summarises the results for the development of degradable polyurethane (DegraPol®, DP30) electrospun scaffold sheets and vascular grafts. The subsections include studies on scaffold morphology, mechanical characterisation, thermal analysis, drug incorporation and elution as well as degradation.

To review, the groups of scaffold sheets (cut from 25 mm tubes) produced will henceforth be referred to as DP30CTRL (DP30 control), HTBlend (0.6wt% HepTBA/DP30 blend electrospun), HiHepCA (high HepNa$^+$ content coaxially electrospun), LoHepCA (low HepNa$^+$ content coaxially electrospun) and NoHepCA (no heparin content coaxially electrospun). The produced vascular grafts will be referred to as DP30CVG (DP30 control vascular graft) and HepCAVG (low HepNa$^+$ containing coaxially electrospun vascular graft).

3.1 Polymer swelling

The polymer swelling response of cast DP30 films is illustrated in Figure 29. The films experienced a small but significant increase of 1.5±0.6 % (P = 0.0.3) in mass within the first day. Further swelling was observed the following day and then the mass increase remained uniform at 3.0±2.2 after 1 week.
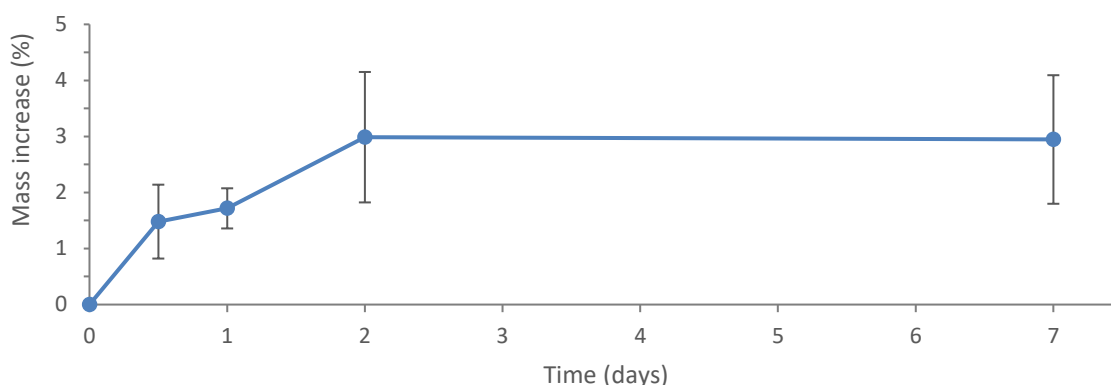
Figure 29: Polymer swelling in DI water as percentage mass increase

This swelling response indicates that despite DP30's hydrophobic nature, it has some water absorbance capacity, with a substantial volume of water absorbed within a short period. Therefore prolonged contact between DP30 and water should be avoided as it could result in swelling. This might explain the difficulty of maintaining stability during coaxial electrospinning with DP30 in the shell and water in the core.

3.2 Scaffold characterisation

This section summarises the resulting fibre morphology and contact angle of scaffold sheets produced by conventional, coaxial and blend electrospinning techniques. SEM images of the scaffolds are displayed in Figure 30.

Sample	Abluminal (x500)	Luminal (x500)
DP30CTRL		
HTBlend		
HiHepCA		
LoHepCA		
NoHepCA		
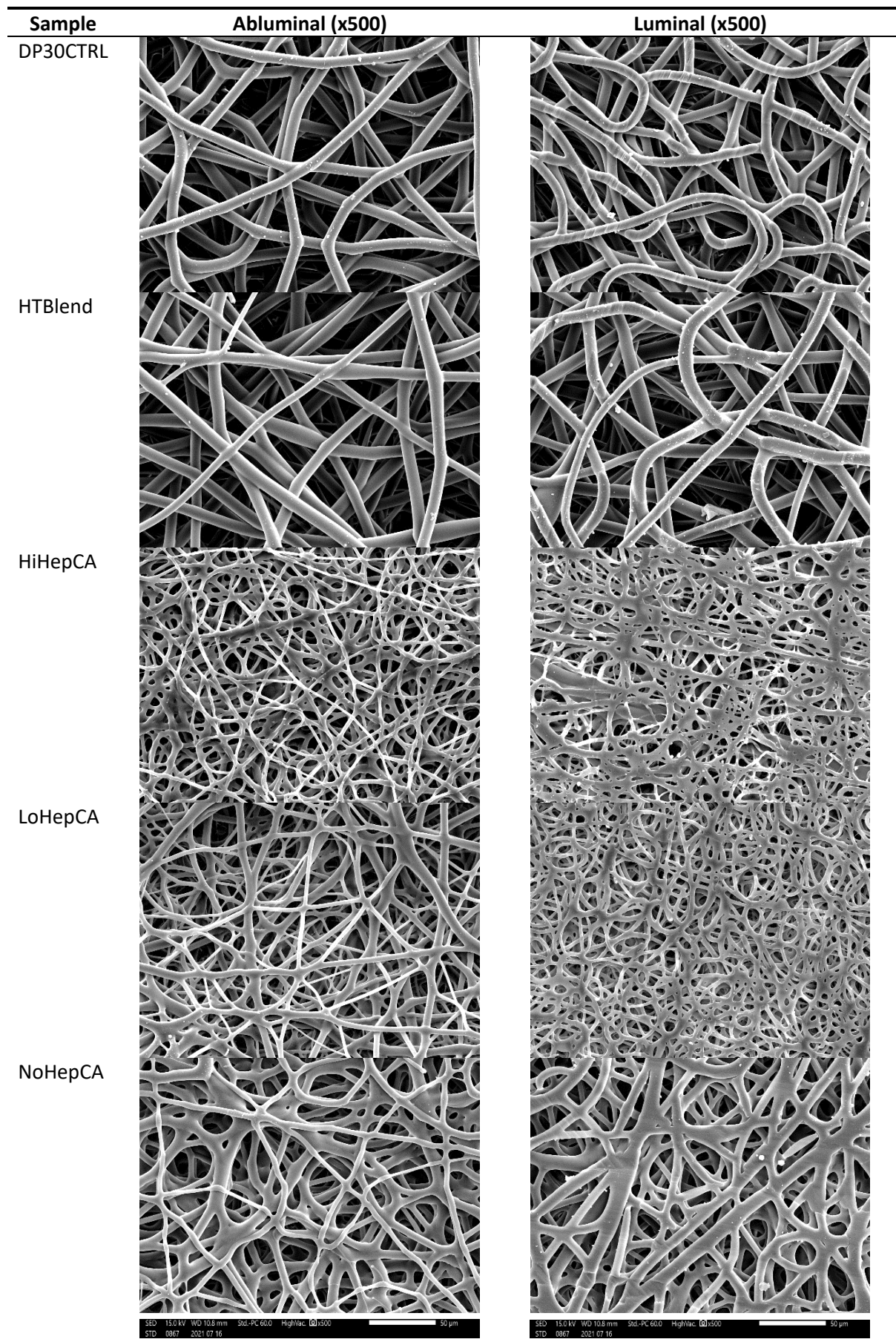
Figure 30: SEM images (Scale bar = 50 µm)

3.2.1 Fibre morphology

3.2.1.1 Fibre diameter

The mean fibre diameter between all groups displayed in Figure 31 was 5.6±2.7 µm. The mean fibre diameter of the heparin containing coaxial fibres (HiHepCA, LoHepCA) was 3.7±1.7 µm compared to NoHepCA with significantly larger fibres of 7.1 ±2.1 µm ($P < 0.001$). Control (DP30CTRL) fibres and blend electrospun (HTBlend) fibres had mean diameters of 7.8±1.0 µm and 8.4±1.8 µm. Overall there was a small but significant difference (< 17.1 %) between the abluminal and luminal fibre diameters within groups ($P < 0.03$).
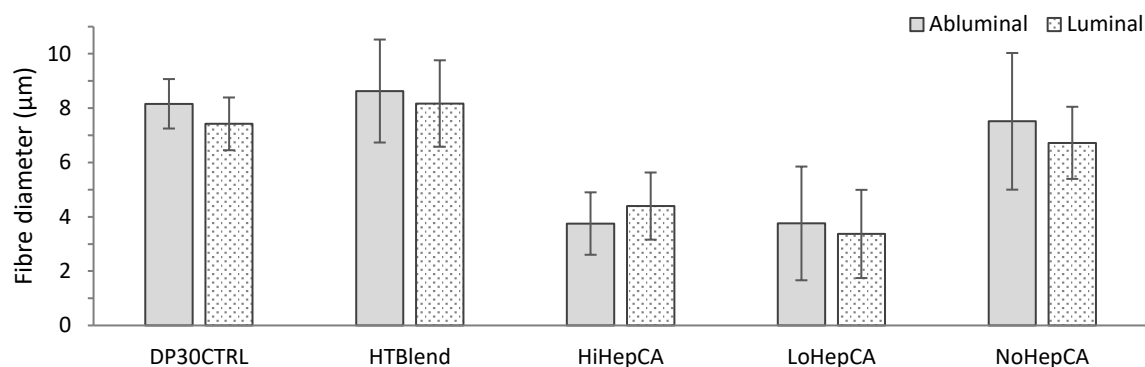
Figure 31: Fibre diameter

Significantly reduced fibre diameters for coaxial groups was probably due to the higher dielectric constant of the water-based core inducing a longer jet stretching and whipping region [255]. Higher voltages were required for coaxial electrospinning (16.5 kV) and could be a supplementary explanation for the significantly thinner fibres produced compared to conventional electrospinning (11.5 kV). The mean fibre diameter decreased by 7.9 % ($P = 0.01$) from DP30CTRL to NoHepCA. A further decrease was expected and achieved with the addition of heparin in the cores due to its high conductivity (charge) with fibres of LoHepCA being half ($P = 1 \times 10^{-34}$) as thick as NoHepCA, corresponding with the 36 % decrease (506 vs 321 nm) in fibre diameter observed by Huang *et al.* [259]. An increased amount of heparin was expected to result in a greater decrease of fibre diameter, but there was however no statistically significant difference between LoHepCA and HiHepCA ($P = 0.98$).

With the addition of HepTBA into the electrospinning solution, a similar trend was expected for HTBlend fibres due to increased conductivity caused by addition of the HepTBA salt. However, this resulted in a small but significant 8.36 % ($P < 0.02$) increase in mean fibre diameter from DP30CTRL to HTBlend. In this case, it could possibly be ascribed to the lower voltage required for stable electrospinning of the blend solution or it might indicate that the TBA modification reduces the charge of HepNa$^+$.

The term *wet landing* is used to describe the excessive merging/fusion of fibres (fibres conglutinated at their junction zone) after landing which can create either smaller pores and flattening of the fibres or in the extreme case where merged completely, results in film formation. Through visual comparison (Figure 30) the coaxial groups showed a higher degree of wet landing which could be ascribed to three factors. Firstly, it was caused by the slightly shorter TCD (27 cm vs 30 cm) required for stable electrospinning and secondly, the presence

of water in the electrospinning solution, with its relatively low volatility, which results in the inability to completely evaporate before landing [249]. Lastly, this could also be explained by the higher humidity (35 % rH) required to prevent clogging of the coaxial needle since previous research by our group found that increased humidity during electrospinning of DP30 resulted in a higher degree of fibre fusion [206]. Wet landing can result in the apparent thickening of the fibres on the luminal surface due to flattening. Even though when surfaces were compared visually there was wet landing on the luminal surface of all groups, only the HiHepCA group presented (apparent) significantly thicker luminal fibres, while DP30CTRL, LoHepCA and NoHepCA groups had significantly thicker fibres on their abluminal surface.

Although an ideal fibre diameter is yet to be determined, previous research indicates a certain threshold may modulate cellular response [289, 290]. Sanders postulated that fibre diameters below 6 µm result in a reduced number of activated macrophages as well as thinner fibrous encapsulation [291-293]. The current fibre sizes are in a similar range to those suggested.

3.2.1.2   Fibre orientation

The mean orientation index (OI) of groups illustrated in Figure 32 was 0.13±0.07. Other than HiHepCA, all groups had similar OIs on their abluminal and luminal surfaces.
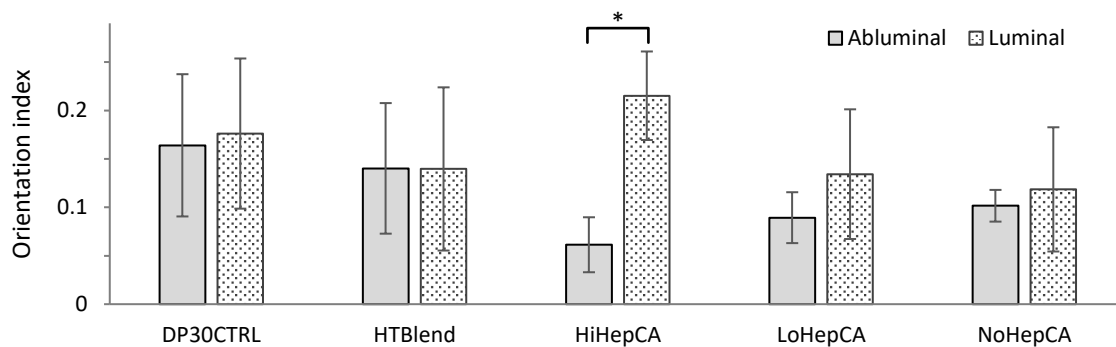
*Figure 32: Coherency of fibres (*P = 0.002).*

The apparent decrease in OI from the luminal to the abluminal surfaces indicates that if there was any level of alignment (even though very small), the effect dissipated at the lumen, showing more random distribution of fibres as the wall thickness of the scaffold sheet increased, likely altering the electric field acting on the fibres from the mandrel. The lower OI among coaxial groups can be explained by the increased whipping and jet stretching caused by the presence of water and heparin (in the case of LoHepCA and HiHepCA). However, despite the statistically significant lower OI of HiHepCA, overall, the low OI's and visual assessment provide no notable indications of fibre alignment.

3.2.1.3   Pore size

DP30CTRL and HTBlend groups had similar mean equivalent pore diameters of 16.6±2.2 µm and 17.2±1.8 µm. Coaxial groups LoHepCA, HiHepCA and NoHepCA had significantly smaller (P <0.01) mean pore sizes of 8.2±1.1 µm, 8.5±1.5 µm and 14.1±2.3 µm respectively.
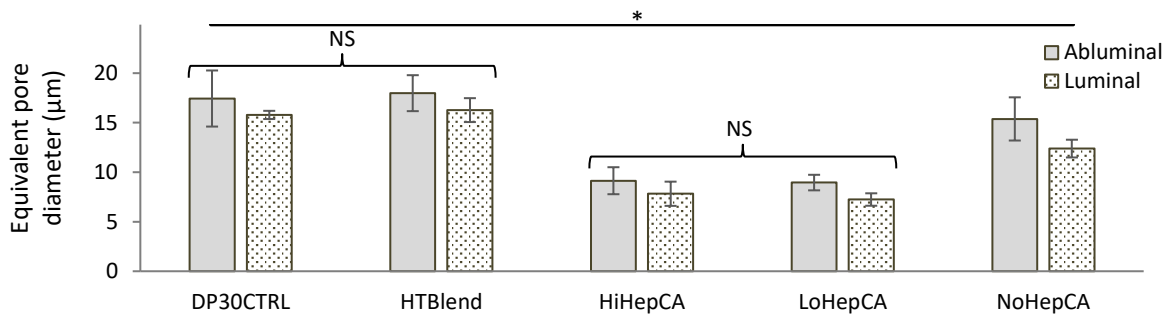
*Figure 33: Pore size of the abluminal and luminal surfaces (*P = 1 × 10^{-26}).*

The decrease in pore size of heparin containing coaxial fibres (LoHepCA and HiHepCA) was expected due to their smaller fibre diameters as it is well documented that larger pores can be obtained by increasing fibre diameter [294, 295]. A similar trend was observed between the pore sizes of groups as between the fibre diameters, establishing their relationship. The addition of a water core resulted in a 15.4 % (P = 0.02) decrease in the mean equivalent pore diameter from DP30CTRL to NoHepCA and the addition of heparin resulted in a further 41.7 % (P = 1 × 10^{-8}) decrease from NoHepCA to LoHepCA. Furthermore, the pore sizes of LoHepCA and HiHepCA were similar (P = 0.5), indicating the negligible effect of the combined increase in heparin and PEO quantity on the pore size. The significantly smaller pore sizes of HiHepCA on the luminal surfaces compared to the abluminal surfaces is characteristic of wet landing.

Sufficient pore size is crucial for ensuring proper graft performance and healing as insufficient size can impede cell infiltration, whereas excessive pore size can lead to problems such as blood leakage [296]. Scaffold pore size and fibre diameter can influence cell phenotype and differentiation as it determines the surface area for cell attachment and migration [293]. Although in vitro and in vivo evaluation would be needed to confirm the adequacy of these pore sizes, it has been shown by Voorneveld et al. that similar 77-98 % cellular infiltration was possible for pore-sizes ranging from 9.9-11.1 μm [297].

3.2.1.4 Porosity

A significant difference in porosity (Figure 34) was observed between scaffold groups (ANOVA: P = 0.0002). Similar mean porosities of 63.7±1.8 % and 60.2±6.7 % were achieved for the control and blend electrospun group, while coaxially electrospun scaffolds yielded significantly lower porosities (P <0.04) of 50.2±3.0 %, 53.2±5.0 % and 44.8±8.1 % for NoHepCA, LoHepCA and HiHepCA groups respectively.
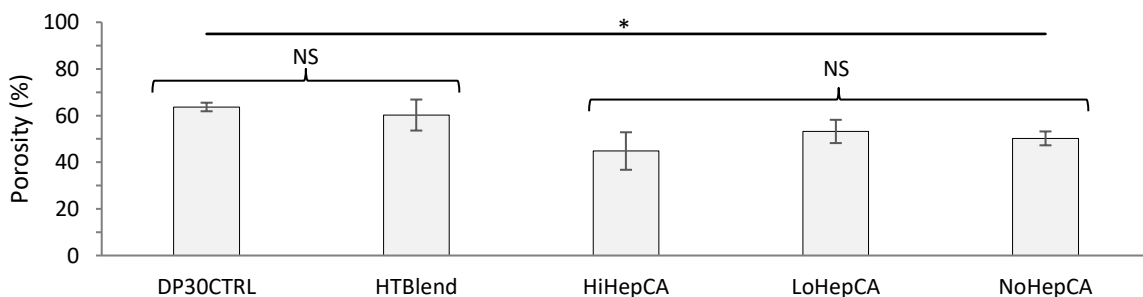
*Figure 34: Porosity (*P = 0.0002).*

Porosity is a key determining factor in graft healing [298-305]. It influences the surface area available for cell attachment and foreign body detection [290]. For polymeric scaffolds that have a wettability attractive to cell infiltration, higher porosities tend to result in increased immune response due to the increased surface area available to cells as the polymer degrades [306]. This results in an increased magnitude of the foreign body response. On the other hand, sufficient void space and interconnectivity is required for capillary ingrowth and subsequent transmural endothelialisation [22].

As expected, coaxial groups had lower porosities (44 - 54 %) which could be ascribed to the observed higher degree of wet landing, especially in the case of HiHepCA. The resulting porosities of produced scaffolds (44 – 64 %) are notably less than previous studies on electrospun DegraPol® which achieved higher porosities of up to 93 % [207, 212, 214-218, 220-222] but it is important to note that these involved various solvents, grades of DegraPol® (not DP30) and porosity enhancing methods (e.g. cryo-electrospinning).

3.2.1.5   Core-shell validation results

Figure 36 shows SEM images of the scaffold groups before and after washing, indicating washed out cores by the presence of holes in the fibres. No sign of cores was visible in fibres of DP30CTRL and HTBlend groups. All coaxial groups showed distinct holes in a substantial portion of the fibres. NoHepCA scaffolds presented large central holes in the majority of fibres (> 90 %), while notably fewer holes (> 70 %) were visible in fibres for LoHepCA scaffolds. HiHepCA scaffolds had the least (> 55 %), and after washing, had distinct groves along the fibre suggesting that during electrospinning the core solution broke through the shell. This phenomenon was observed more prominently during initial experimentation (Figure 35).
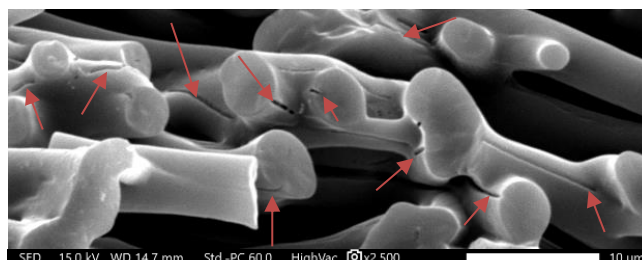
Figure 35: Extreme example of indentation/grooves along fibres after washing (indicated in red).

The unchanged fibre morphology (absence of holes) of DP30CNTRL and HTBlend confirms the legitimacy of the resulting visible holes in fibres representing cores in the coaxial electrospun scaffolds. An interesting observation was that these two groups seemed to have rougher surfaces compared to coaxial groups.

The indentations (grooves) along some HiHepCA fibres can be explained by the results of initial experimentation where it was evident that during electrospinning the core solution broke through the shell, most likely as a result of the heparin increasing the conductivity of the core solution. These 'surfaced' water cores could explain the higher degree of fibre fusion for the HiHepCA group due to 'wetter' surfaces. This could explain why HiHepCA fibres, containing more heparin, exhibited this indentation prominently with a reduced number of cores compared to LoHepCA fibres which contained less heparin. Finally, it could also be the reason why NoHepCA scaffolds had the largest population fraction of fibres with distinct holes.
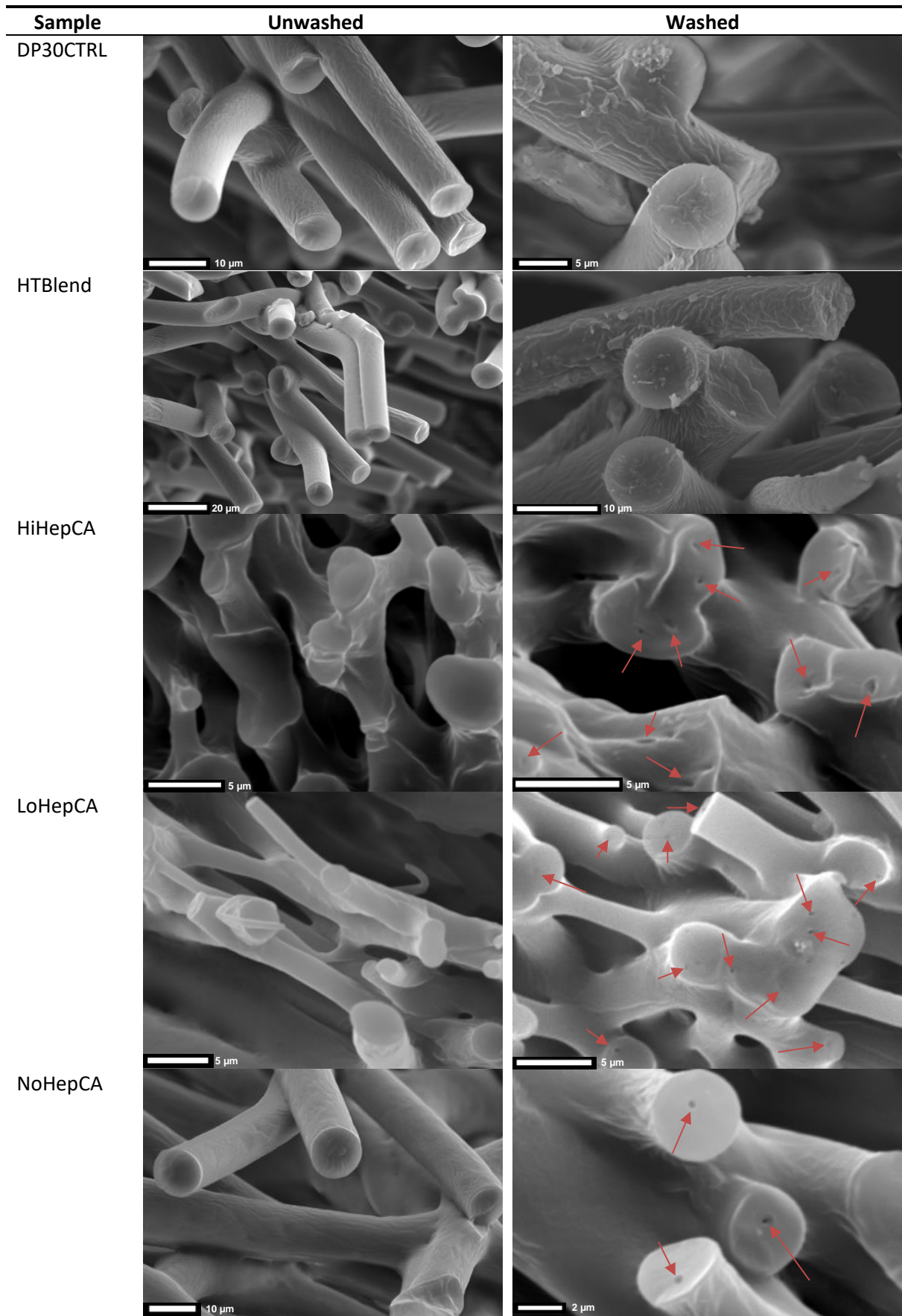
Figure 36: Cross-sectional SEM images of unwashed and washed samples for core-shell validation (red arrows indicate holes – washed out cores).

3.2.2 Contact angle

The mean contact angles for the abluminal and luminal side of all electrospun groups were 121±8 ° (P = 0.23) and 105±13 ° (P = 0.07) respectively. Compared to electrospun scaffolds, the ablumen and lumen of cast DP30 films had significantly smaller mean contact angles of 93±2 μm and 98±1 ° (P = 7 × 10^{-6}). The luminal contact angle of HiHepCA was less (> 11 %) than that of HTBlend (P = 0.03) and LoHepCA (P = 0.02).
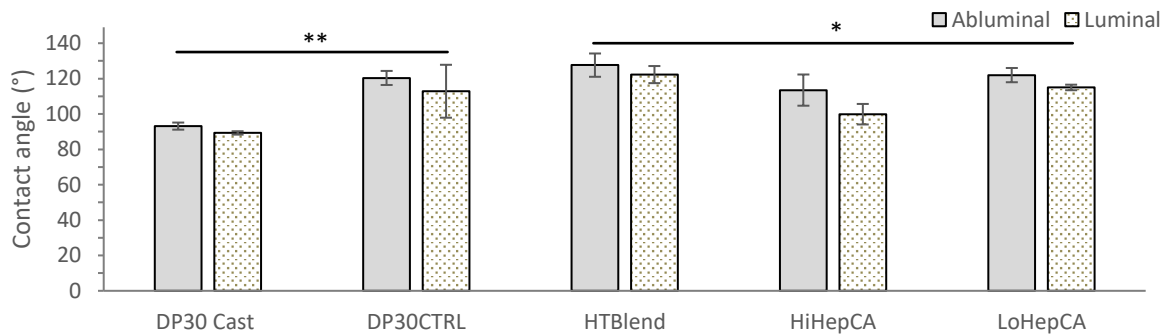
Figure 37: Water contact angle, (*P = 0.006, **P = 7 × 10^{-6}).

Some researchers state that polymers are hydrophobic when θ > 90 ° and hydrophilic when θ < 90 ° [307]. Therefore, DP30 could be classified as hydrophobic, but seeing as the contact angle of films approached the threshold, the hydrophilicity can only be confirmed by determining more complex variables such as the sliding, advancing, and receding angle.

It was noted that HiHepCA had the lowest contact angle and HTBlend, the highest (P = 0.004). HighHepCA's lower contact angle could be attributed to the higher degree of fibre fusion while HTBlend's high contact angle could be due to the large fibre size, high porosity and the presence of HepTBA (during the TBA-modification the drug is made less hydrophilic).

3.3 Mechanical properties

This section explores the mechanical properties of produced scaffolds. It is important to note that comparison between mechanical values of scaffolds sheets and native vasculature are purely illustrative and do not reflect a direct comparison as the produced scaffolds were not tubular and factors such as diameter, thickness and length were not considered when comparing. Figure 38 shows a typical stress-strain response resulting from tensile testing of the scaffolds.
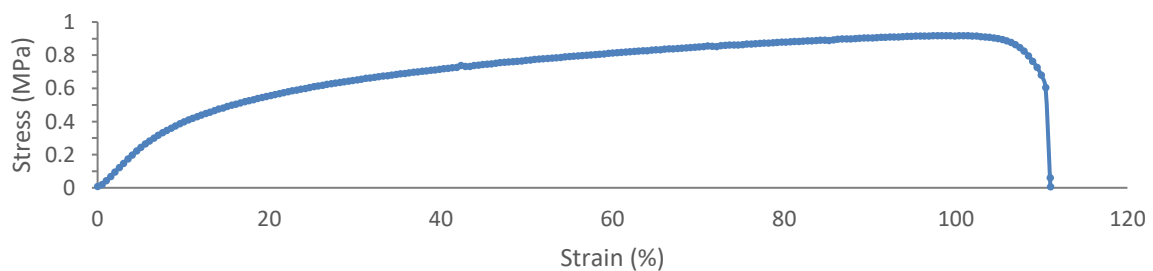
Figure 38: Example of an acquired stress-strain curve

3.3.1 Ultimate tensile stress (UTS)

The groups had similar mean ultimate tensile stresses in the circumferential and longitudinal direction of 1.31±0.32 MPa (ANOVA: P = 0.053) and 1.49±0.48 MPa (ANOVA: P = 0.27) respectively. There was no statistically significant difference within groups between the longitudinal and circumferential UTS. The only exception was the DP30CTRL group, which had a 36.41 % (P = 0.008) higher ultimate tensile stress in the longitudinal direction.
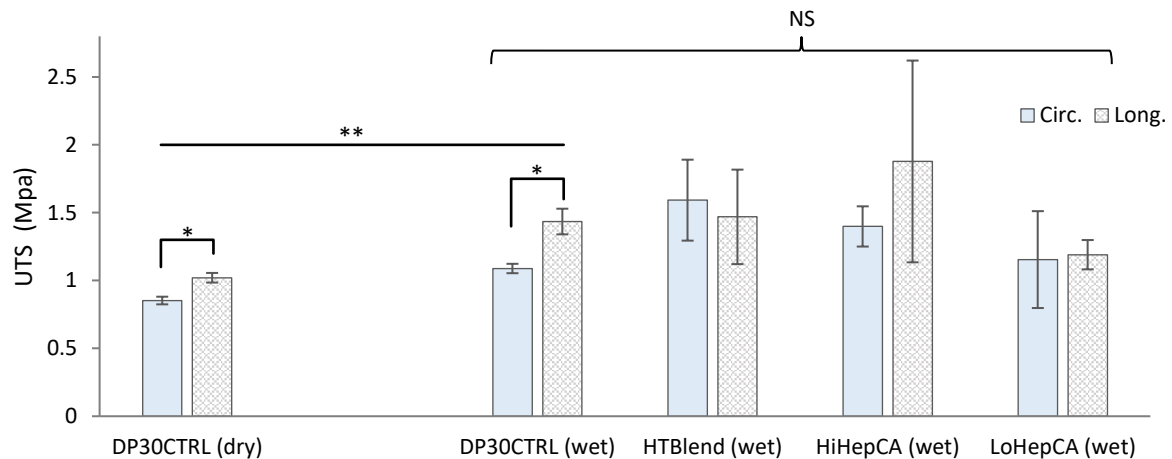
Figure 39: Ultimate tensile stress (UTS) in the longitudinal and circumferential direction, (*P < 0.01, **P = 5 × 10⁻⁶).

The bulk material UTS characterised in a previous study by this research group was $UTS_{DP30,cast}$ = 3.50±0.25 MPa [209]. The UTS of scaffold groups (0.85 MPa – 1.87 MPa) were about half of this bulk UTS, which agrees with the generalisation that electrospun scaffolds are weaker than cast scaffolds (less material due to porous scaffolds).

It is interesting to note that notwithstanding a two-fold difference in fibre diameter between control and coaxial groups, no significant difference in UTS was observed. Although statistically non-significant in most cases, groups (excluding HTBlend) tended to exhibit a higher UTS in the longitudinal direction. This is significant in the case of DP30CTRL, and due to its slightly higher OI observed in Section 3.2.1.2, suggests that there is marginal alignment of fibres in the longitudinal direction. This could possibly be due to the lower whipping and jet stretching due to the absence of a heparin/water core or HepTBA increasing conductivity and dielectric constant of the solution. The slow rotational speed would also contribute to this phenomenon as it makes it difficult to align fibres circumferentially resulting in the deposition of fibres along the axial direction.

The scaffold UTS values were much lower than most documented values for human vasculature [308]. Circumferential UTS resembled recorded values of the SV (1.8 MPa), femoral arteries (1 – 2 MPa) and the coronary arteries (0.39±0.07 MPa [113], 0.45±0.19 MPa [114]) but was lower than IMA's (4.1 MPa) [40, 105]. The longitudinal UTSs were approximately a third of an IMA's (4.3 MPa) and a fifth of an SV's (6.3 MPa) [105, 309]. The burst strengths of vascular grafts made from these scaffolds, however, can be engineered to be far in excess of requirements as will be shown in Section 3.7.2.4.

3.3.2 Maximum elongation

Similar maximum elongations, ε_{max}, (Figure 40) were exhibited by groups in the circumferential and longitudinal direction of 160.2±48.2 % (P = 0.1) and 128.3±30.6 % (P = 0.2). The surface-wet control group (D) was the only group with a difference between the circumferential and longitudinal direction, with a significantly higher ε_{max} in the circumferential direction (P = 0.04).
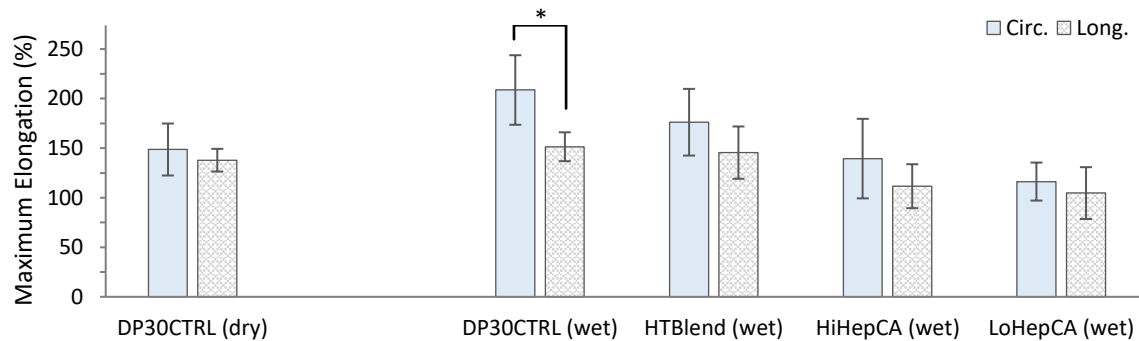
*Figure 40: Maximum elongation (%) in the longitudinal and circumferential direction (*P = 0.04).*

Bulk material characterisation demonstrated ε_{max} of 216±29 % for cast DP30 films [209]. Briefly, the electrospinning process reduced the achieved ε_{max}. The only group that indicated comparable elongation at failure is DP30CTRL electrospun scaffolds (specifically in the circumferential direction), whereas the notable decrease for other groups suggests that the blend and coaxial electrospinning process significantly reduces the ε_{max}.

Altogether, the scaffolds had higher ε_{max} in the circumferential direction, with DP30CTRL (surface-wet) showing a significant 57.3 % higher elongation in the circumferential direction. This agrees with the statement that the fibre alignment of groups (especially DP30CTRL) had a slight inclination toward the longitudinal direction. Furthermore, the lowest ε_{max} were among the coaxial groups LoHepCA and HiHepCA, which could be ascribed to more wet landing and possibly its thinner fibres.

Scaffolds had maximum elongations at failure comparable to those of the human femoral artery ($\varepsilon_{max,circ.}$ = 63 -155 %, $\varepsilon_{max,long.}$ = 120 % [40, 111]) and IMA ($\varepsilon_{max,circ.}$ = 134 %, $\varepsilon_{max,long.}$ = 59 % [105]). In some studies SVs demonstrated much higher maximum elongations in the circumferential direction of 242 % [105] but others only reached 11 % [106].

3.3.3 Youngs modulus

The Youngs modulus (E_Y) of scaffold groups (Figure 41) were similar (P = 0.3) with a mean E_Y value of 5.39±2.53 MPa. The acquired values for E_Y of scaffolds were approximately 30 % less than the bulk E_Y of 7.96±0.64 MPa characterised in a previous study by this research group [209]. Similar E_Y irrespective of the direction are indicative of anisotropy of fibres. These values also further suggest that coaxial electrospinning or heparin addition does not unduly affect the mechanical properties. These values of produced scaffolds are comparable to some E_Y for native vasculatures such as the FA_{circ} (E_Y = 9-12 MPa) and SV_{circ} (E_Y = 4.2±3.3 MPa [105]), but significantly less than others e.g. SV_{long} (E_Y = 130.2±56.4 MPa) and IMA_{long} (E_Y = 16.8±7.1 MPa).
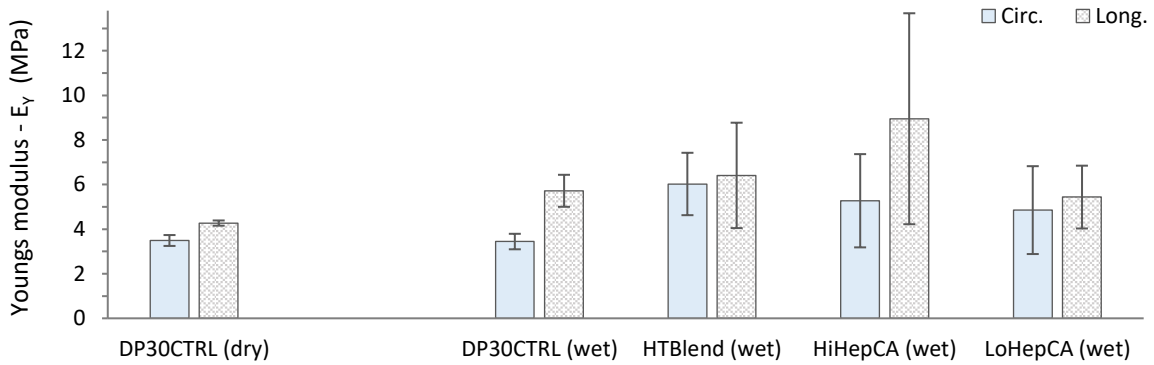
Figure 41: Youngs modulus (MPa) in the circumferential and longitudinal direction.

3.3.4 Suture retention strength

The mean suture retention (SR) strength was 2.82±0.99 N per mm thickness (P = 0.55) with no statistically significant difference between groups or between directional properties within groups.
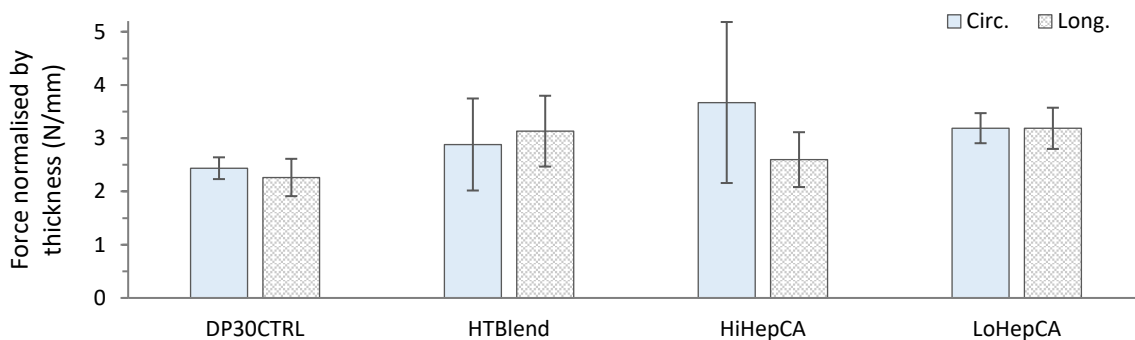
Figure 42: Suture retention (pull out) strength in the longitudinal and circumferential direction.

The lack of difference between directional pull out strengths confirms the anisotropy of scaffolds and the similar inter-group values agrees with the UTS trend. Consequently, it can be concluded that excluding some minor differences, the conventional, coaxial and blend electrospinning did not result in major differences in mechanical response despite the differences in fibre diameter and porosity. All groups revealed a similar suture retention force which was higher than that of the native aortic rat vessel of 1.7 ± 0.7 N [308].

3.4 Differential scanning calorimetry (DSC)

DSC was performed to see if the electrospinning process had any obvious or major effects on crystallinity etc., not for full comparison and statistical analysis. The DSC thermograms for raw materials are given in Figure 43. Raw DP30 and PEO (400 kDa) exhibited melting temperatures (T_m) of 135.2 °C and 70.9°C with T_c of 66.2 °C and 43.7 °C. HepNa$^+$ did not show a distinct melting and crystallisation phase but the thermogram was consistent with a previous study [310]. Heating of HepNa$^+$ resulted in a minor peak at 156.9 °C (ΔH = -0.1 J/g) followed by a major endothermal peak at 175.9 °C (ΔH = 148.3 J/g) and an exothermal peak at 246.4 °C (ΔH = -330.4). When cooled there was only a minor exothermal peak at 202.3 °C (ΔH = -9.2).
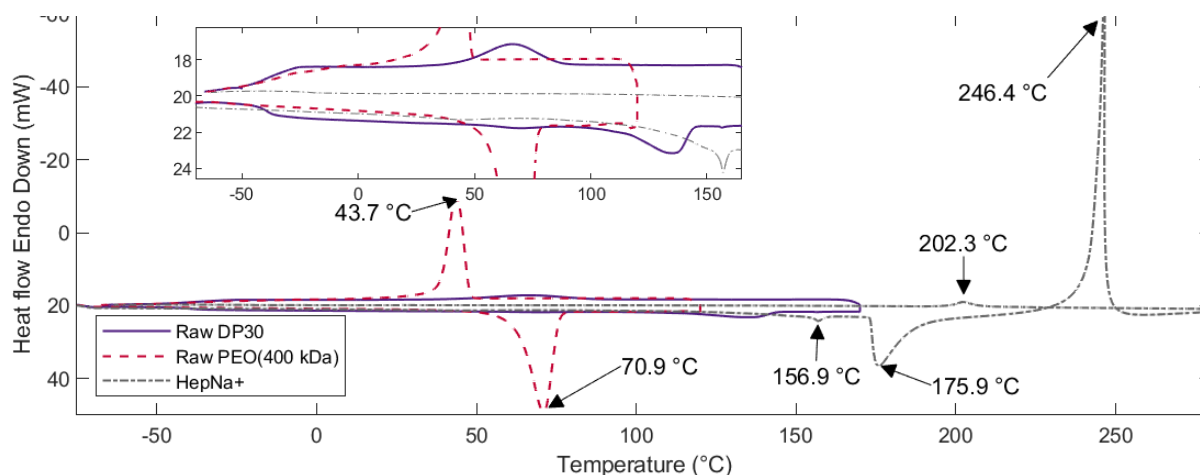
Figure 43: DSC thermograms of raw DP30, PEO(400 kDa) and HepNa⁺.

Figure 44 shows the DSC thermograms of DP30 in different states (raw, quenched and electrospun). There seemed to be some slight differences between raw DP30 and electrospun DP30 but no major changes or appearance/disappearance of peaks which would have indicated a change in thermal properties or crystallinity caused by the electrospinning process that could influence polymer degradation or drug release response. During the increasing thermal scan on quenched (at 170 °C) raw DP30, an exothermal peak at 73.8 °C (ΔH = -27.9 J/g) and an endothermal peak at 136.3 °C (ΔH = -22.9 J/g) were observed. This represented a crystallinity for raw DP30 of approximately 82.3 % (22.9 J/g /27.9 J/g).
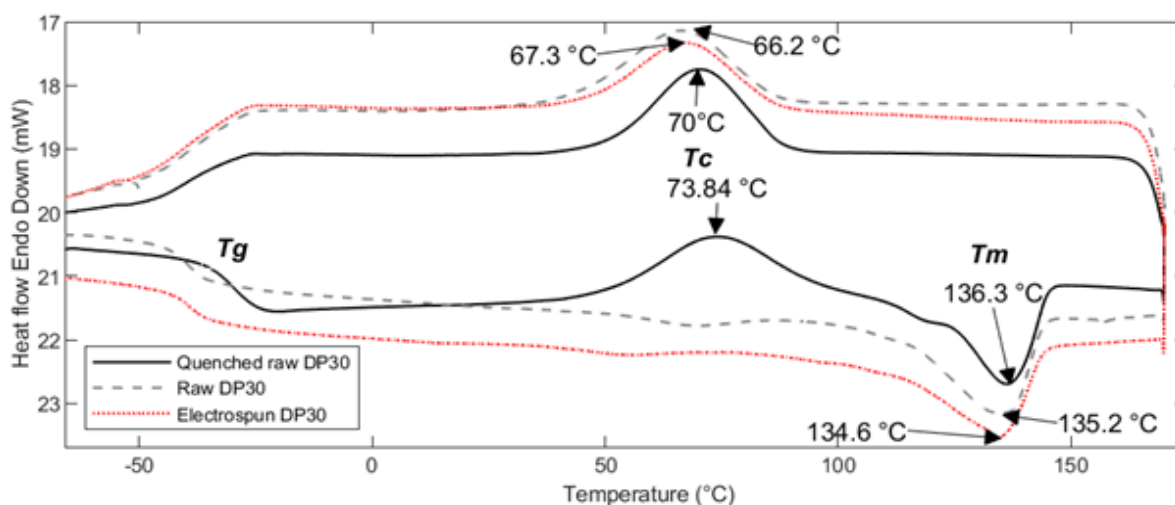
Figure 44: DSC thermograms of raw DP30 (normal and quenched) and electrospun DP30 scaffolds.

The DSC thermograms for control, blend and coaxially electrospun samples are given in Figure 45. The glass transition temperature (T_g) of scaffold groups were within the range of -40.2 °C to -39.1 °C. The scaffolds had T_m between 130.1°C and 139.5 °C and T_c between 61.3 °C and 68.0 °C. There were distinct endothermal peaks (encircled in Figure 45A) during the increasing temperature cycle for LoHepCA and HiHepCA at temperatures of 52.5 °C (ΔH = 2.84 J/g) and 52.7 °C (ΔH = 3.4 J/g) and slightly higher at 59.8 °C (ΔH = 2.7 J/g) for NoHepCA. These endothermal peaks observed only for coaxial groups around 55 °C were attributed to the presence of the HepNa⁺/PEO cores since the melting phase for raw PEO starts around this temperature. This is further confirmed by the fact that HiHepCA, which contains the most

PEO, has the largest enthalpy change at this phase. No signs of HepNa$^+$ were visible for LoHepCA and HiHepCA, but this was expected due to the large quantity and mostly since its characteristic peaks only appear above 150 °C.
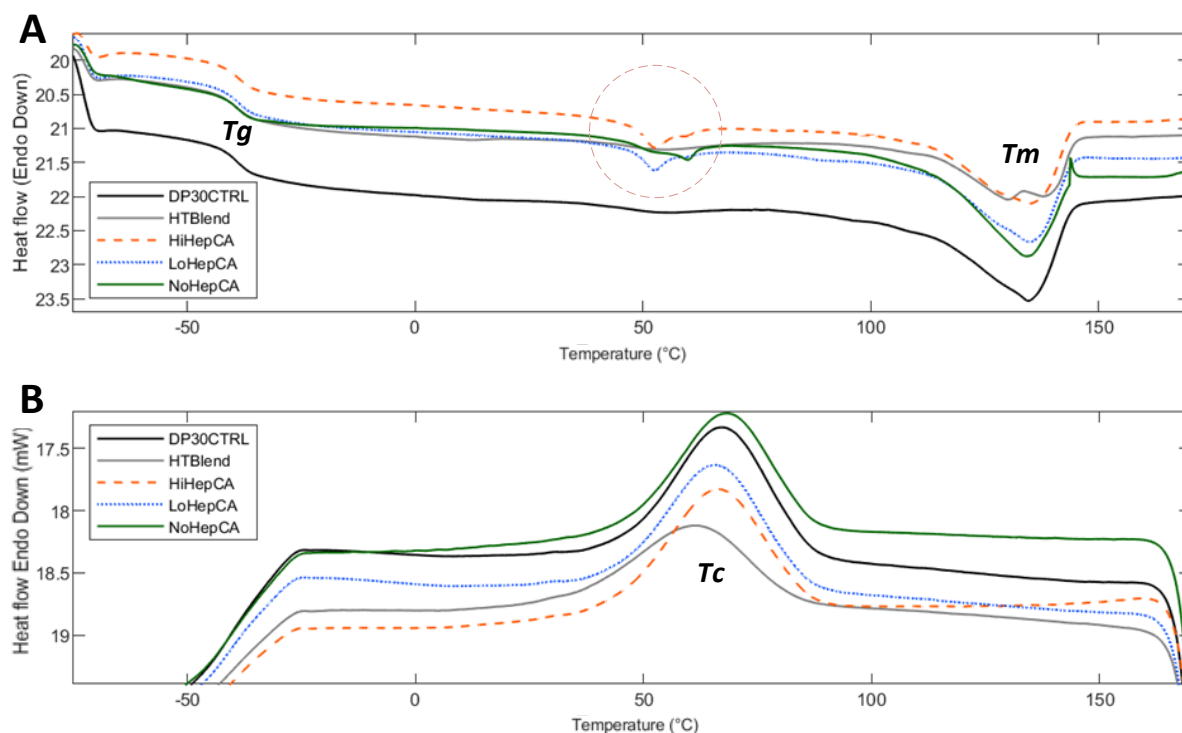
Figure 45: DSC thermograms of electrospun scaffold groups. A) Increasing temperature cycle (heating). B) Decreasing temperature cycle (cooling).

3.5 Drug incorporation and elution

This section reports on heparin quantification in terms of expressing the cumulative release as a percentage of the total amount of drug incorporated and the normalised instantaneous heparin quantity released at time points over 6 weeks according to UV-spectrometry measurement. Thereafter the bioactivity of heparin eluted from the scaffolds will be covered.

3.5.1 Drug release profile

3.5.1.1 Percentage cumulative release

The mean normalised cumulative release of LoHepCA, HiHepCA and HTBlend are given in Figure 46 as a percentage of the total mass incorporated and the exploded view (B) depicts the initial 4-day release in greater detail. LoHepCA and HiHepCA had similar cumulative releases at all time points. From Day 2 and Day 3 onwards, the cumulative release of HTBlend differed significantly (P < 0.5) from the respective cumulative release of LoHepCA and HiHepCA.

All groups displayed an initial burst release within the first 3 days with LoHepCA, HiHepCA and HTBlend releasing a cumulative percentage of 38.7±5.5 %, 42.8±8.4 % and 34.9±7.0 % within the first 24 hours and 55.2±3.8 %, 63.0±12.7% and 44.3±7.0 % after 48 hours. After 3 days,

the cumulative release of LoHepCA and HiHepCA was approximately 1.5 × higher than that of HTBlend (P < 0.02).

LoHepCA and HiHepCA had similar cumulative releases after 1 week ($\bar{x}$ = 74.6±12.6 %) and 3 weeks ($\bar{x}$ = 82.9±14.8 %), whereas the cumulative release of HTBlend at these timepoints (1 week: 52.8±7.3 %, 3 weeks: 55.9±7.4 %) were much lower (P < 0.03). The final cumulative release for LoHepCA, HiHepCA and HTBlend was 97.7±6.3 %, 81.9±18.2 % and 56.1±7.5 %.
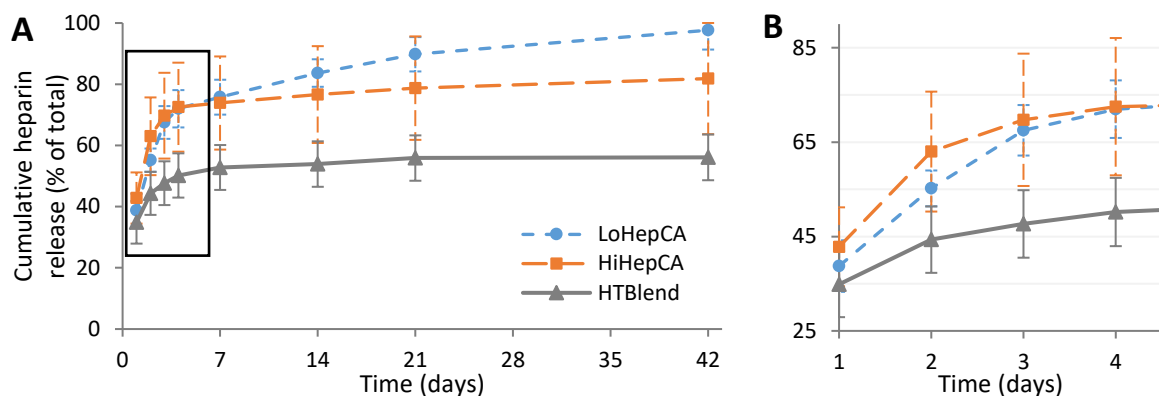
Figure 46: A) Cumulative drug release from LoHepCA, HiHepCA and HTBlend as a percentage of the total drug incorporated. Exploded view B) Detailed initial 4 days.

Due to the gradient of the curves approaching zero towards the end of the study, it was assumed that the samples would no longer release significant amounts of heparin after 6 weeks and that the total possible released amount has been reached. The cumulative release of LoHepCA and HiHepCA was significantly higher than the release of HTBlend, indicating that both HiHepCA and LoHepCA demonstrated higher encapsulation efficiency (how much of the total drug incorporated has been released when the release presumably stops – indicating how efficate the incorporation method was). If assumed that drug release stopped after 6 weeks for all groups, LoHepCA had a mean encapsulation efficiency approximating 100 % while HiHepCA's mean efficacy was less at 81.9 %, although there was no statistically significant difference between the two. HTBlend's significantly lower mean encapsulation efficiency of 56.1 % was nearly half of LoHepCA's and HiHepCA's (P < 0.04). This could however not be confirmed unless the elution study was executed until total degradation of the scaffolds.

The initial burst release of the coaxial groups was higher than anticipated and contrary to expected, also seemingly higher than the release from HTBlend (P > 0.1). Thereafter the coaxial groups however continued to release large quantities, while the release from HTBlend reduced notably faster. Compared to general reviews on coaxial electrospinning [187, 189], a possible cause for these significantly higher initial releases could be the inconsistent core-shell morphology discussed in Section 3.2.1.5 since these uncentred and/or surfaced cores would result in higher release rates as the distance for the diffusion gradient is reduced. The results do however correspond with other studies that coaxially incorporated heparin such as Hu et al. where a 48 % release of HepNa$^+$ was observed within the first 24 hours [263]. The subsequent sustained drug release is however characteristic of coaxial drug incorporation and the faster release by HiHepCA vs LoHepCA is also typical for higher drug loading [189, 254]. HTBlend's more hydrophobic nature (larger contact angle), its 2× thicker fibre diameter as

well as the fact that HepTBA is less soluble in water than HepNa$^+$ could explain its delayed drug release compared to the coaxial groups which contained highly water-soluble HepNa$^+$.

An alternative approach to show that HTBlend had a substantial initial bulk release is that within the first 48 hours it released 79.0 % of the total amount released during the 6 weeks (2.66 mg of 3.37 mg). The release response of HTBlend agrees with a previous study [279] where 1 wt% HepTBA was eluted from PLCL electrospun scaffolds and an initial burst release occurred during the first few days with a cumulative release of 31 % achieved after 4 weeks. Interestingly, the study found an increase in efficacy (encapsulation efficiency) with increased drug loading (5 wt% and 10 wt% HepTBA yielding 36% and 53 % release), where these results proved 20 % higher efficacy for a lower drug loading (0.6 wt %). This difference can be due to the different polymers used (PLCL vs DP30).

To conclude, the initial burst release of heparin, as well as the sustained release (more prominent in LoHepCA and HiHepCA), may be beneficial in vascular grafts for the development of an anti-thrombotic lumen and prevent SMC proliferation and IH.

3.5.1.2   Normalised instantaneous release

Figure 47 represents the instantaneous release of the coaxial groups (LoHepCA and HiHepCA) normalised to the average of the DP30CTRL and NoHepCA release per day and HTBlend normalised to the DP30CTRL-HepTBA noise reading. During the first 24 hours, sample groups LoHepCA, HiHepCA and HTBlend respectively released a mean quantity of 1.4±0.2 mg HepNa$^+$, 2.7±0.5 mg HepNa$^+$ and 2.1±0.4 mg HepTBA per gram scaffold. The following day LoHepCA, HiHepCA and HTBlend experienced a significant decrease of 57.7 %, 54.5 % and 72.9 % in the amount of the drug released and the day thereafter a further 25.2 % (P = 0.5), 58.0 % (P = 0.03) and 64.9 (P = 0.2) decrease.

LoHepCA exhibited another significant decrease in the quantity of heparin released from Day 3 to Day 4 (63.6 % decrease, P = 0.02). Thereafter, LoHepCA showed no statistically significant difference between the heparin quantities released on sequential time points, except from Day 7 to Day 14 (108.5 % increase, P = 0.02). Following the large quantities of drug release in the first week, the average daily release from LoHepCA for the succeeding 5 weeks was 36.5±6.7 µg HepNa/g (P = 0.6). After Day 3, HiHepCA also only showed a significant difference between the quantities of heparin released at subsequent time points from Day 7 to 14, in which case the release doubled (from 1.4±1.1 % to 2.8±0.9 %, P = 0.04). HTBlend released similar HepTBA quantities at subsequent time points, except for the last week where the quantity of HepTBA released decreased by 88.4 % (P = 0.04).
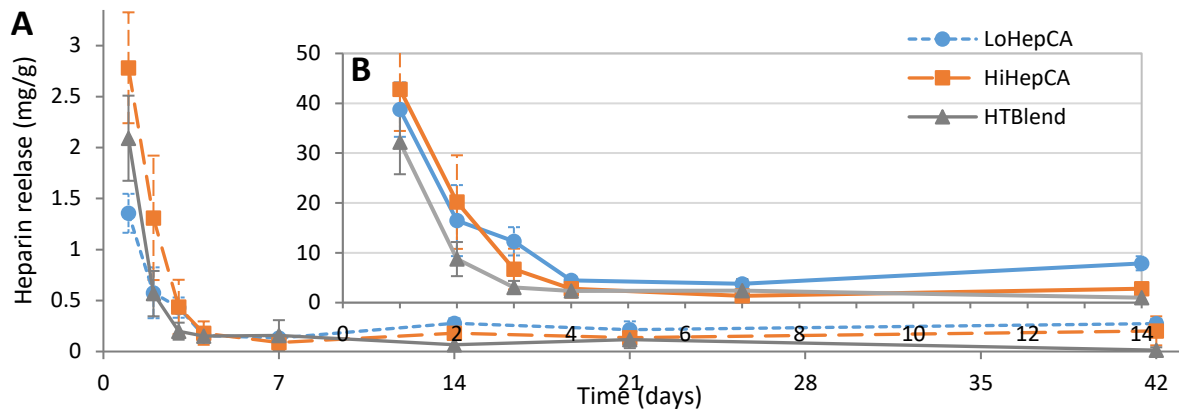
Figure 47: Normalised instantaneous heparin release from LoHepCA, HiHepCA and HTBlend A) of 6 weeks in mg/g and B) 14 days as the percentage of total drug incorporated.

The instantaneous release values of LoHepCA and HiHepCA were significantly higher than HTBlend at each time point (P < 0.01), the most noteworthy being during the last week where HTBlend's value was approaching zero. The only exception was Day 7 to 21 for HiHepCA vs HTBlend.

The significant decrease in the instantaneous release over the first few days was expected as the rate of diffusion decreases due to lowering diffusion gradients. In the case of LoHepCA and HiHepCA, the significant doubling of the instantaneous heparin release from Day 4 – 7 to Day 7 – 14 was likely, since the period lengths compared were 3 days vs 7 days. Taking this into account, it could be assumed from the insignificance in instantaneous release at subsequent time points, that a sustained release was attained from Day 4 to Day 42. This is the desired response of coaxial fibres. For both groups, when considering the increasing period between time points, the plateaux of the instantaneous release curves shows that the release rate gradually decreased.

As illustrated by the steep initial gradient, drug release from HTBlend decreased more rapidly. The similar releases between points would suggest that a sustained release had been accomplished over the full 6 weeks. The lack of significant difference between the DP30CTRL and unnormalized HTBlend values (from pre-normalised data) would however suggest that the quantity of HepTBA being released from Day 7 to 42 was very low (or at least much lower than the coaxial groups) and this was further implied by the significantly higher quantities released by LoHepCA and HiHepCA at time points during this period. It could be assumed that the last noteworthy release was during the Day 14 – 21 period (most probably due to bulk degradation/ saturation of fluids) since the HTBlend value was comparable to the HiHepCA values (P = 0.75) and more so since the release decreased to a tenth of the previous week with a final value of 0.01 mg/g. Therefore it was assumed that the drug release from HTBend stopped after the initial 3 weeks.

3.5.2 Heparin activity

Figure 48 shows the average antithrombotic activity of blood treatment groups as measured by TEG (full results in Appendix H) and the output parameters given in Figure 49 A-D.
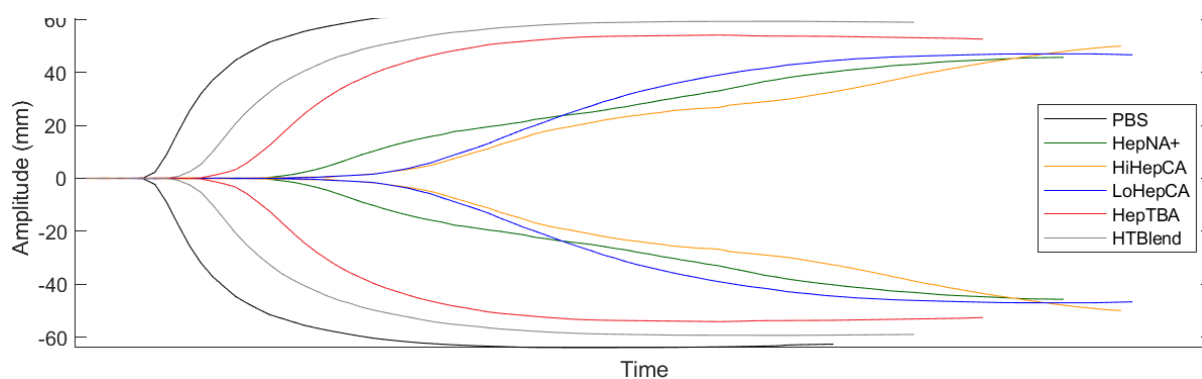
Figure 48: Mean antithrombotic activity from TEG per blood treatment group.

The time to initiate a clot within a sample of human blood (reaction time, R) treated with HepNa$^+$ (0.01 mg/ml) was delayed by more than 4 times when compared to samples where heparin was not present (P = 0.09). HepTBA (0.01 mg/ml) was also found to be antithrombotic but only proved to delay the reaction time two-fold (P = 0.03). Taking the larger variation of HepNa$^+$ and HiHepCA into account, it was clear that the reaction time of HepNa$^+$ (30.3±12.1 min), LoHepCA (26.5±2.2 min) and HiHepCA (43.0±17.8 min) were within the same range. HTBlend eluates had a mean reaction time of 24.2 % lower than HepTBA-stock solution.

The speed of clot formation (Figure 49B) for all heparin containing treatments was significantly decreased (higher kinetic time, K) compared to PBS samples (P < 0.05). Similar to the reaction time, the longest kinetic times were observed among HepNa$^+$ and its scaffold eluates (K$_{mean}$ = 12.9±3.6 min, P = 0.3) with no statistically significant difference among them. HepTBA showed an inferior ability to slow down clot formation (K = 5.1±0.4 min) and again HTBlend eluates exhibited a 26.7 % lower value (P = 0.03).

The clotting angles (α) presented an inverse response with a similar trend (Figure 49C). A significantly higher clotting angle was observed among the PBS group (α = 59.9±0.7 °), with the lowest clotting angles observed among HepNa$^+$, LoHepCA and HiHepCA eluates (α$_{mean}$ = 16.7±5.9 °). The HepTBA solution showed a clotting angle of 34.1±1.2 ° and the clotting angle of HTBlend eluates was 20.5 % higher.

From Figure 49D it is evident that the maximum amplitude (MA) showed a trend similar to the clotting angle with significantly lower values for heparin containing treatments than PBS (P = 0.008), and approaching significance among the heparin groups (P = 0.07).
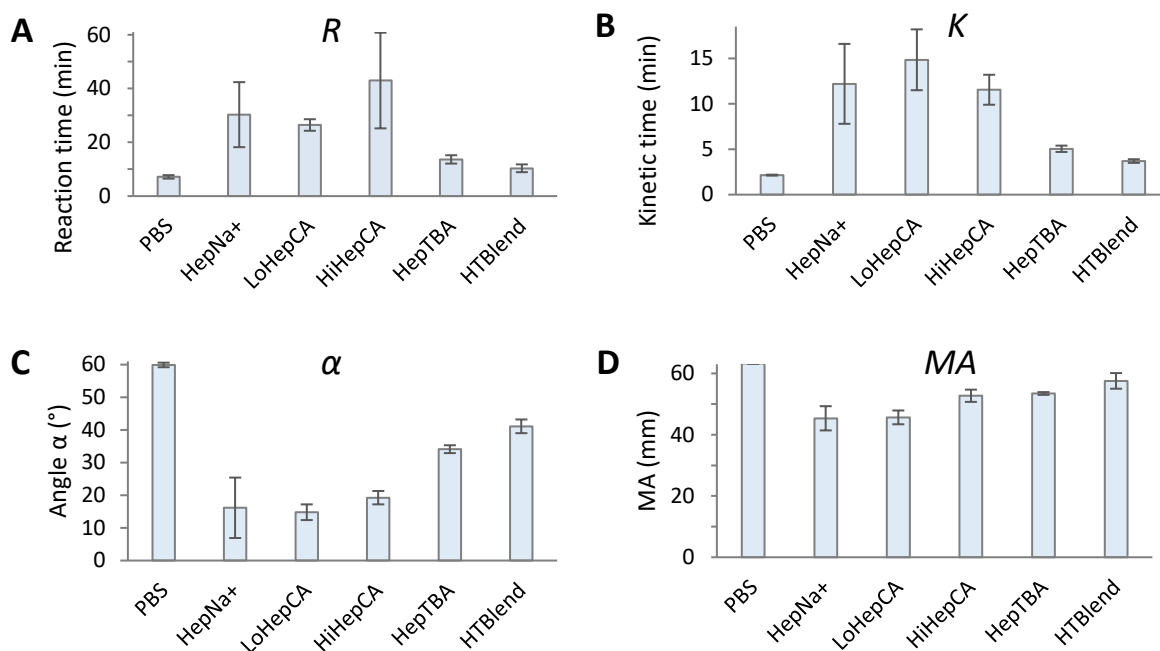
Figure 49: A) R time, B) K time, C) α and D) MA values of TEGs per blood treatment group.

One of the major challenges associated with the incorporation of drugs into electrospun scaffolds is preventing sensitive agents from losing their bioactivity during or after processing and electrospinning. With all blood treatment groups exhibiting statistically significant differences compared to the control group (PBS) it is evident that all groups presented some extent of antithrombogenicity.

HepNa$^+$ seemingly retained its antithrombotic properties post-processing and post-electrospinning as a scaffold eluted product since all parameters were within the same range with no statistically significant differences. Heparin, post TBA-modification, however, retained some but not all of its antithrombotic properties (-55.0 % R, -58.6 % K, +111.2 % α, +17.9 % MA), which was further reduced post electrospinning (-24.2 % R, -26.7 % K, +20.5 % α, +7.8 % MA). The post electrospinning reduction could be explained by exposure to harsh conditions such as high electric fields and organic solvents (CHCl$_3$). In the case of coaxial electrospinning, the bioactivity is retained as the drug is protected from the external environment by the shell solution and avoids direct contact with toxic solvents.

Therefore, it is evident that of produced scaffolds, the most superior antithrombotic properties were observed among coaxial electrospun fibres which indicated no signs of major modification in bioactivity. The eluates' ability to slow down the reaction time (R) and the speed of clot formation (K) and reduce the clot strengthening (α) and clot firmness (MA) would all be beneficial for vascular graft applications [286].

Although some differences discussed do not have P < 0.05, they have P < 0.1, approaching significance when considering the sample size of n = 2. Furthermore, it is important to note that the observations discussed were confirmed based on a direct comparison between sample groups at each experimental repeat.

3.6 Degradation study

This section summarises the rate of hydrolytic degradation by characterising in vitro mechanical and mass loss as well as thermal analysis after a 6-week incubation period.

3.6.1 Mechanical loss

3.6.1.1 Ultimate tensile stress loss

Figure 50A shows that after 6 weeks, samples experienced a mean loss in circumferential UTS of 41.4 % (P = 0.01). The circumferential UTS of DP30CTRL decreased from an initial 1.09±0.03 MPa on Day 0 to 0.80±0.08 MPa (26.5 %, P = 0.01) and 0.92±0.26 MPa (15.5 %, P = 0.4) after 3 and 6 weeks. Coaxial groups LoHepCA and HiHepCA exhibited a decrease in circumferential UTS after 6 weeks of 51.2 % (UTS$_{6w - LoHepCA}$ = 0.56±0.23 MPa, P = 0.1) and 43.6 % (UTS$_{6w - HiHepCA}$ = 0.79±0.44 MPa, P = 0.1). HTBlend lost 50.0 % (P = 0.04) of its circumferential UTS from 1.59±0.30 MPa to 0.79±0.21 MPa.

The mean longitudinal UTS decreased by 44.4 % (P = 0.0005) from 1.49±0.48 MPa to 0.83±0.23 MPa as displayed in Figure 50B. DP30CTRL and HTBlend exhibited 45.7 % (P = 0.02) and 50.0 % (P = 0.07) loss in longitudinal UTS to 0.78±0.21 MPa and 0.73±0.23 MPa. The longitudinal UTS of LoHepCA and HiHepCA decreased by 29.2 % and 48.6±6.90 % from 1.19±0.11 MPa and 1.88±0.73 MPa to 0.84±0.14 MPa and 0.97±0.26 MPa.

The final time point for DP30CTRL is assumed to contain an outlier, 1.21 MPa, (motivated by the significantly larger error and the fact that this point exceeds the initial UTS). If this outlier was discarded, DP30CTRL would follow the same trend as the other sample groups with a final decrease of 28.9 % after 6 weeks.
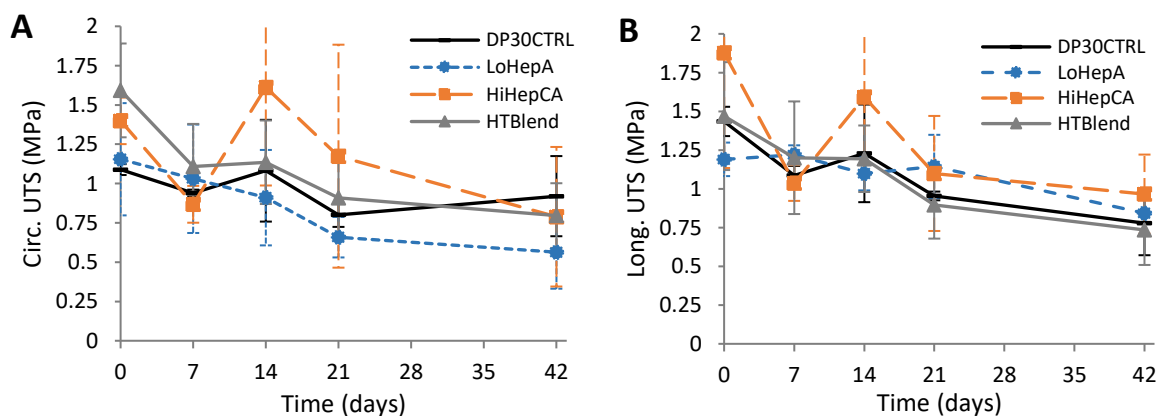
Figure 50: Change in UTS after 7, 14, 21 and 42 days of degradation. A) Circumferential. B) Longitudinal.

The observed responses are likely to result from initial water uptake followed by progressive degradation of the polymer by hydrolysis. The degradation response is consistent with a previous study where, after 4 weeks of incubation in PBS, the pure DP30 scaffolds lost 46 % and 32 % in circumferential and longitudinal UTS, with HepTBA incorporated scaffolds (3 wt%) exhibiting slightly higher losses of 50 % and 35 % in circumferential and longitudinal UTS [206].

3.6.1.2 Maximum elongation loss

It is clear in Figure 51 that the circumferential and longitudinal maximum elongation (ε_{max}) decreased for all groups after 6 weeks of incubation with an overall decrease in mean circumferential ε_{max} of 82.6 % ($P = 9 \times 10^{-9}$) from 160.2±48.2 % to 28.5±7.8 %, and in longitudinal mean ε_{max} of 79.8 % ($P = 3 \times 10^{-10}$) from 128.3±30.6 % to 25.9±6.9 %.

During this period, DP30CTRL, LoHepCA, HiHepCA and HTBlend respectively lost 85.1 % ($P = 0.002$), 76.5 % ($P = 0.004$), 81.0 % ($P = 0.02$) and 83.5 % ($P = 0.004$) of its inherent elongation properties. All groups showed significant loss after the initial 2 weeks with circumferential ε_{max} decreasing by at least half ($P < 0.05$).

The longitudinal ε_{max} of DP30CTRL and HTBlend decreased to less than a quarter of their initial values to final elongations of 24.9±2.0 % ($P = 0.0002$) and 31.3±9.7 % ($P = 0.004$). LoHepCA and HiHepCA respectively lost 73.7 % ($P = 0.015$) and 82.2 % ($P = 0.004$) of their inherent elongation properties. All groups, except LoHepCA, experienced a significant decrease in the longitudinal ε_{max} within the first week.
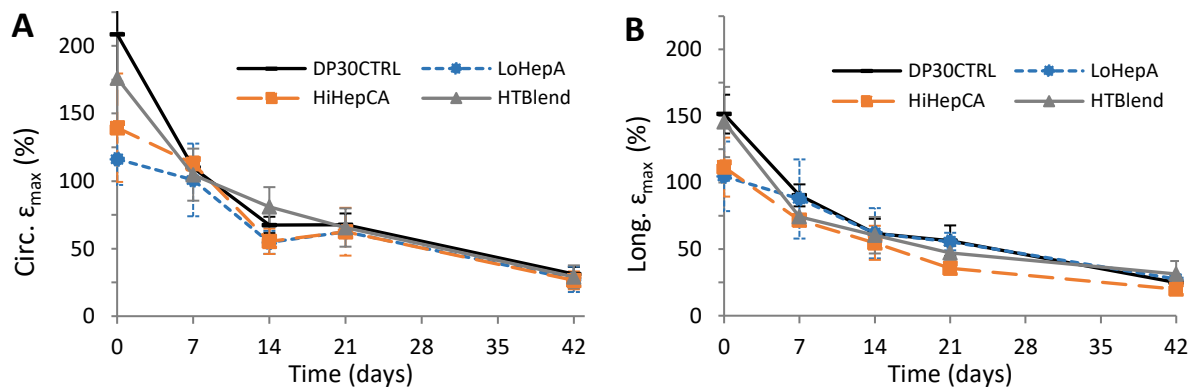
Figure 51: Change in maximum elongation (%) after 7, 14, 21 and 42 days of degradation. A) Circ. B) Long.

The significant decrease in elongation within the first few weeks could also be attributed to the swelling of fibres due to water uptake causing a loss in elongation capacity. More loss in maximum elongation was experienced in the circumferential direction (82.2 % vs 79.8 %) but this could be explained by the fact that the circumferential direction had superior initial maximum elongations. Interestingly, despite the large difference between initial maximum elongations of groups, the maximum elongations converged to the same values over the period. No obvious trend was observed regarding the degradation response between electrospinning techniques since, overall, the DP30CTRL group exhibited the most loss in maximum elongation followed by HiHepCA, HTBlend and lastly LoHepCA.

3.6.1.3 Change in Youngs modulus

Overall, Figure 52 shows that degradation had minimal influence on Youngs modulus (E_Y) as there was no significant change for any of the groups between timepoints. Hence, a mean E_Y of 6.02±1.56 MPa was calculated across the time points and groups.
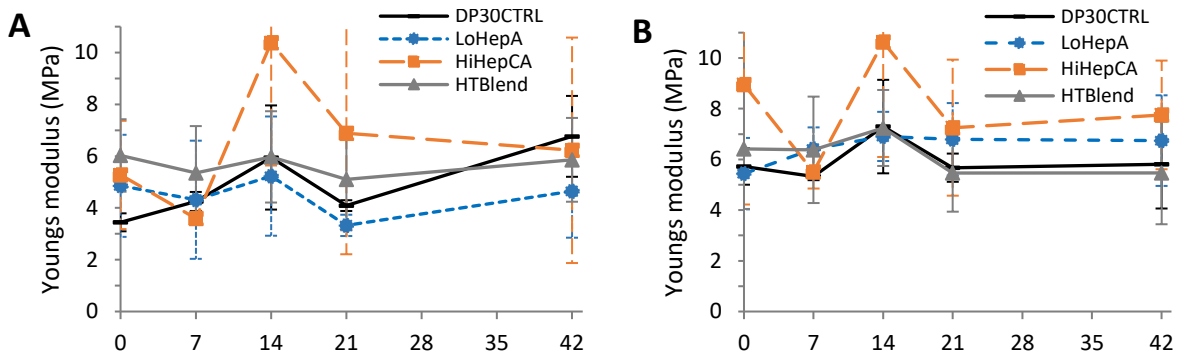
Figure 52: Change in Youngs modulus (MPa) after 7, 14, 21 and 42 days of degradation. A) Circ. B) Long.

It is necessary for a vascular graft to preserve its elastic properties since a certain consistent E_y is required to allow the tissue to thrive and differentiate [311]. The constant E_y for scaffold groups over time in both directions ensures the scaffolds maintains mechanical integrity while allowing and aiding in cell ingrowth and proliferation [208].

3.6.2 Mass loss

Figure 53 provides the 6 week mass loss responses of mechanically tested samples and drug elution samples. The degradation mechanical samples (Figure 53A) were used for illustrative purposes only, to establish whether an apparent trend occurred for mass loss over the 6-week period. From the trend in groups, it was assumed that the observed mass loss for the first three weeks was likely due to fibre loss as loose fibres were seen floating in the PBS after removal of samples. The significant average drop from 3.3±0.6 % to 5.5±1.1 % (P = 0.03) between weeks 3 and 6, however, could be due to hydrolytic degradation combined with fibre loss.

The drug elution samples provided a more accurate quantitative representation of the mass loss since there was no fibre loss caused by mechanical testing, and the replacing of fresh PBS at each time point closer resembles physiological conditions. After 6 weeks, all groups had similar mass loss with an average of 2.5±2.1 % (P = 0.06). For both experiments (Figure 53A and B), the coaxial groups seemed to exhibit more mass loss.
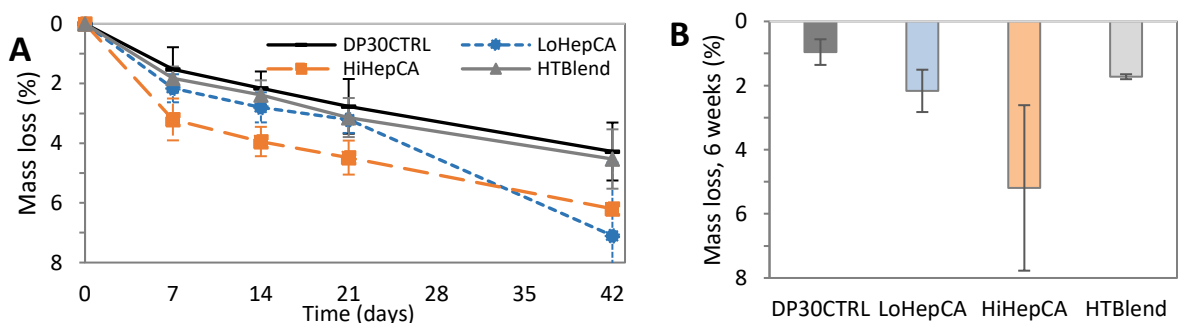
Figure 53: Mass loss (%) over time. A) Mechanical loss samples at W0, 1, 2, 3, 6. B) Drug elution samples at W6.

3.6.3 Change in thermal properties (DSC)

The DSC thermograms for scaffold groups at various degradation time points (Week 0, 3 and 6) are illustrated in Figure 54.
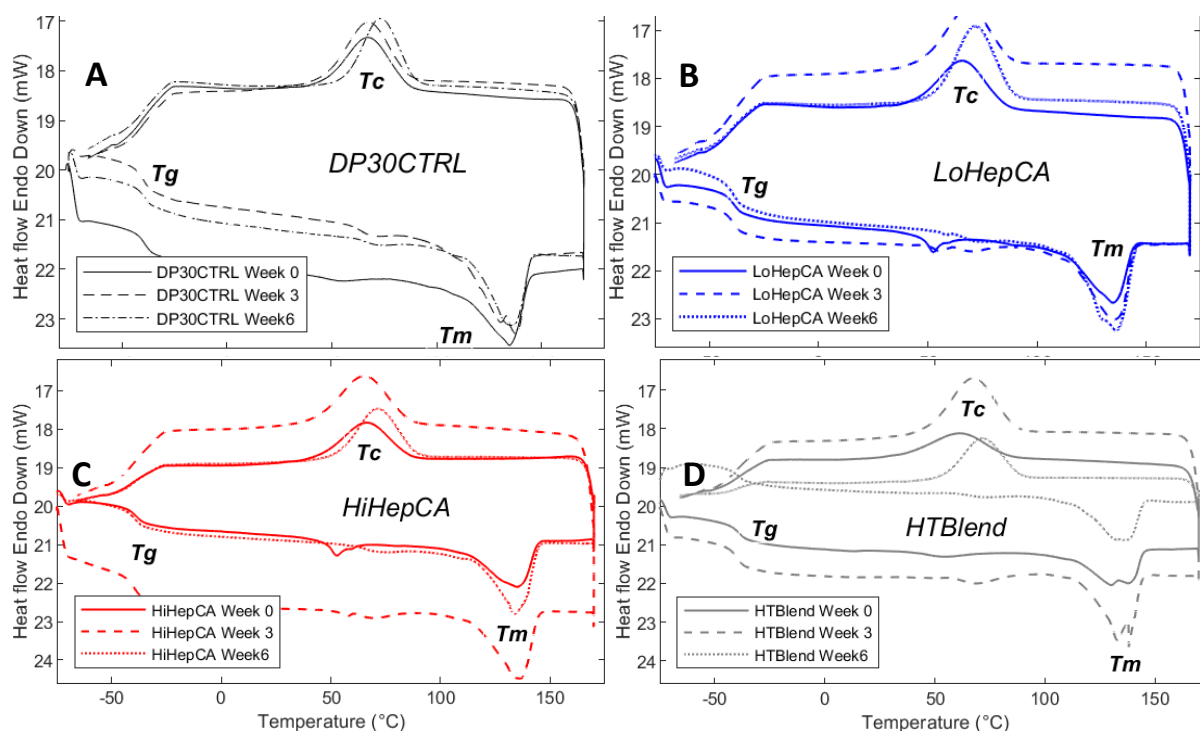
Figure 54: DSC thermograms after 0, 3 and 6 weeks of degradation for scaffold groups A) DP30CTRL, B) LoHepCA, C) HiHepCA and D) HTBlend.

Through visual comparison, it was evident that the slight endothermal peaks around 55 °C observed at Week 0 for coaxial groups (HiHepCA and LoHepCA) dissipated over the 6-week period. The peaks became smaller at Week 3 and were not present at Week 6, indicating that the HepNa$^+$/PEO cores responsible for this phenomenon eluted completely from the scaffolds after 6 weeks.

The change in enthalpies and temperatures at glass transition, melting and crystallisation are shown in Figure 55 and Figure 56. The enthalpy change at melting (ΔH_m) was between -27.7 J/g and -24.5 J/g for all groups and between 20.4 J/g and 32.9 J/g at crystallisation (ΔH_c) with no obvious overall trend over the 6 week degradation period.
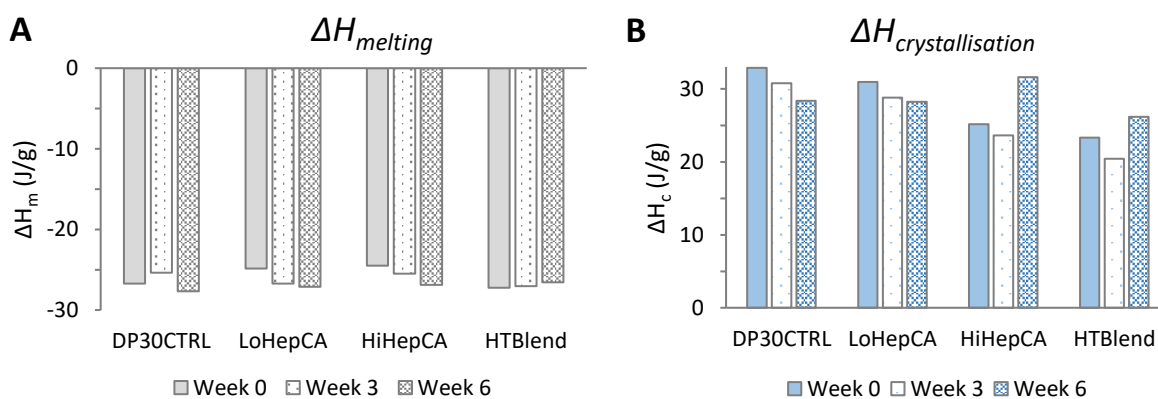
Figure 55: Enthalpy at Week 0, 3 and 6. A) Melting. B) Crystallisation.

Figure 56A shows the glass transition temperatures (T_g) of all groups increased after 3 weeks from a range between -39.8 °C and -39.1 °C to between -40.9 °C and -40.1 °C. Thereafter, T_g for coaxial groups were between -43.49 °C and -42.99 °C after 6 weeks while T_g for DP30CTRL and HTBlend were between 39.5 °C and -39.3 °C.

The melting temperatures (T_m) after 3 and 6 weeks of degradation were within the range of 135.1-137.8 °C and 133.6-136.5 °C, respectively as provided in Figure 56B.

Overall, the crystallisation temperature (T_c) of all groups seemed to increased over time. T_c was between 65.0 and 68.4 °C after 3 weeks and between 71.3 and 73.1 °C after 6 weeks.
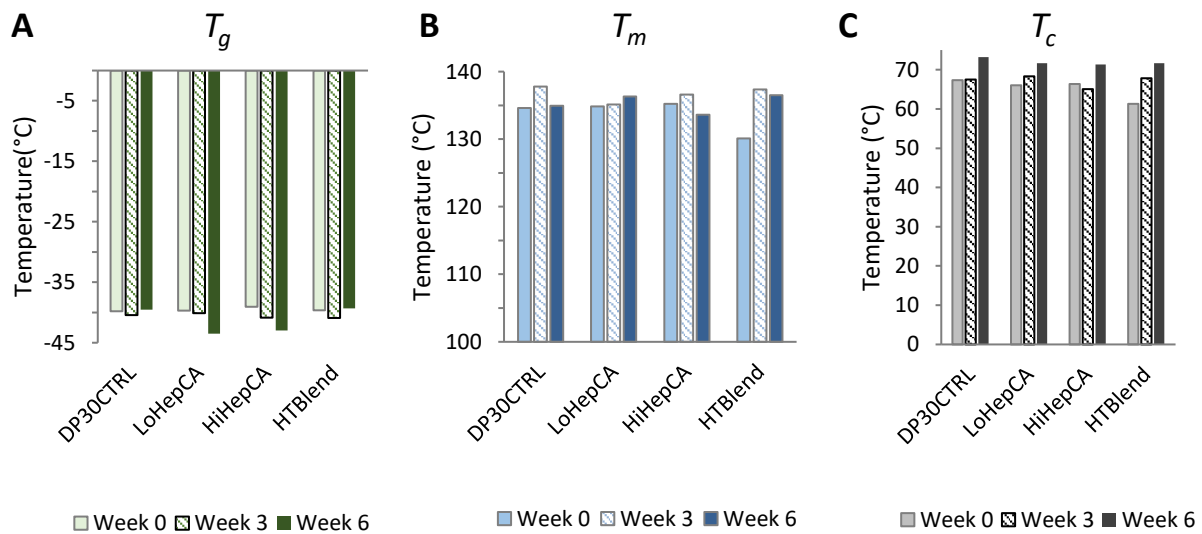
Figure 56: Temperature at Week 0, 3 and 6. A) Glass transition. B) Melting. C) Crystallisation.

With the exception of some minor apparent trends discussed above, there were no obvious major changes in the thermal properties after the 6-week degradation period.

3.7 Vascular grafts

This section summarises the morphological and mechanical properties of vascular grafts produced in the translational study. The two vascular graft types will be referred to as DP30CVG (DP30 control vascular graft) and HepCAVG (heparin containing coaxial electrospun vascular graft). The wall thickness of DP30CVG and HepCAVG ranged from 0.33-0.48 mm and 0.25-0.4 mm, respectively.

3.7.1 Fibre morphology

SEM images of the scaffolds are displayed in Figure 57.
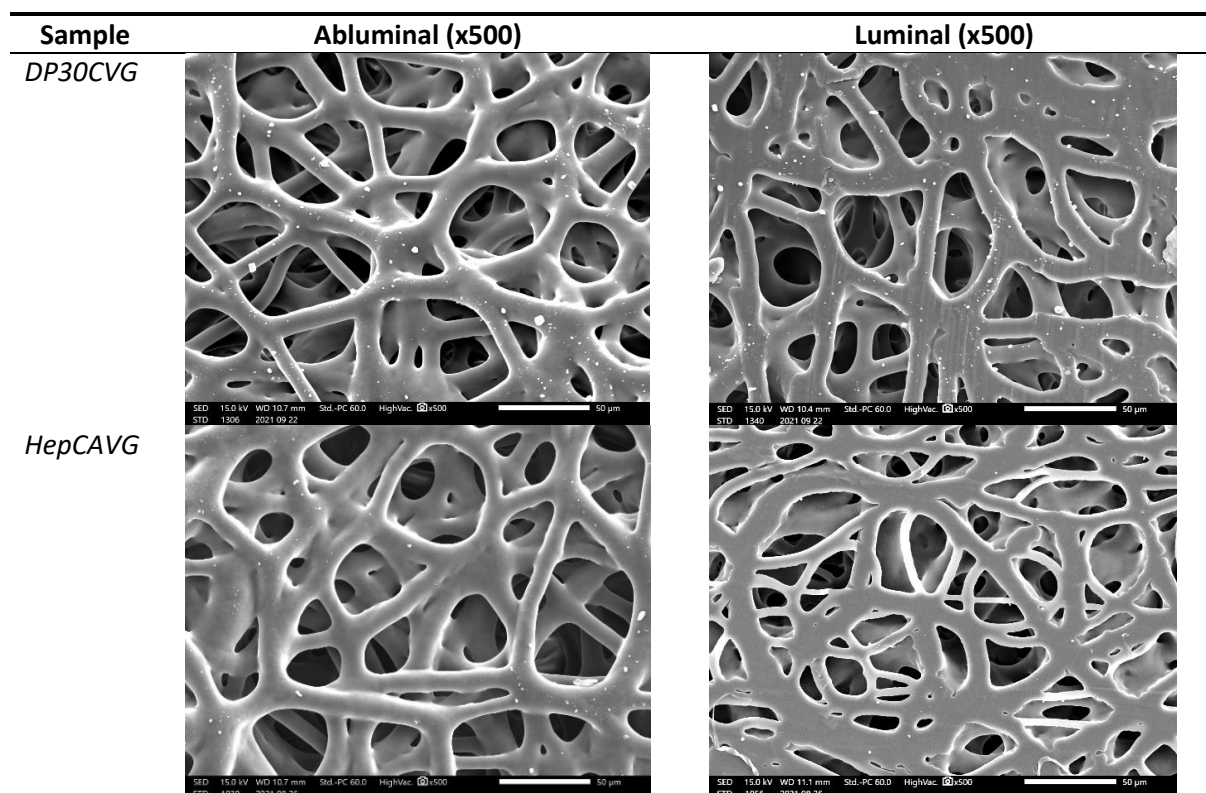
Figure 57: SEM images of vascular grafts (Scale bar = 50 µm).

3.7.1.1 Fibre diameter

The DP30CVG group had significantly (P = 2×10^{-7}), but only slightly (11.9 %), larger fibres on its luminal surface compared to its abluminal surface (10.3±1.8 µm vs 9.2±1.6 µm) and the HepCAVG group exhibited similar mean abluminal and luminal fibre diameters of 7.9±2.6 µm and 7.7±3.5 µm (P = 0.8).

The addition of heparin containing water cores resulted in a significant 19.6 % (P < 10^{-6}) decrease in mean fibre diameter from the control group (DP30CVG) to the coaxial group (HepCAVG). This agrees with the trend observed previously in Section 3.2.1.1 for scaffold sheets and can be attributed to the increased electrical properties causing more whipping and jet stretching [255].

Through visual comparison, it is clear that the DP30CVG experienced 'wet landing', which was confirmed by the significantly flatter (apparently thicker) fibres on the luminal side. Visually, the degree of wet landing on the HepCAVG lumen was notably less than on the DP30CVG lumen, which could be ascribed to the heparin/water presence causing more whipping and resulting in fibres landing 'dryer'.

Compared to sheets cut from 25 mm tubes, the produced vascular grafts had significantly larger fibre diameters for both groups ($P < 10^{-8}$) with DP30 control fibres exhibiting a 24.6 % increase from DP30CTRL to DP30CVG while the coaxial electrospun fibre diameters were more than double (119 % increase) from LoHepCA to HepCAVG. This could be explained by the higher negative voltage required to ensure fibre deposition on the smaller mandrel, which in turn results in less whipping and jet stretching. The significant reduction in mandrel area for fibre deposition would also affect the fibre landing.
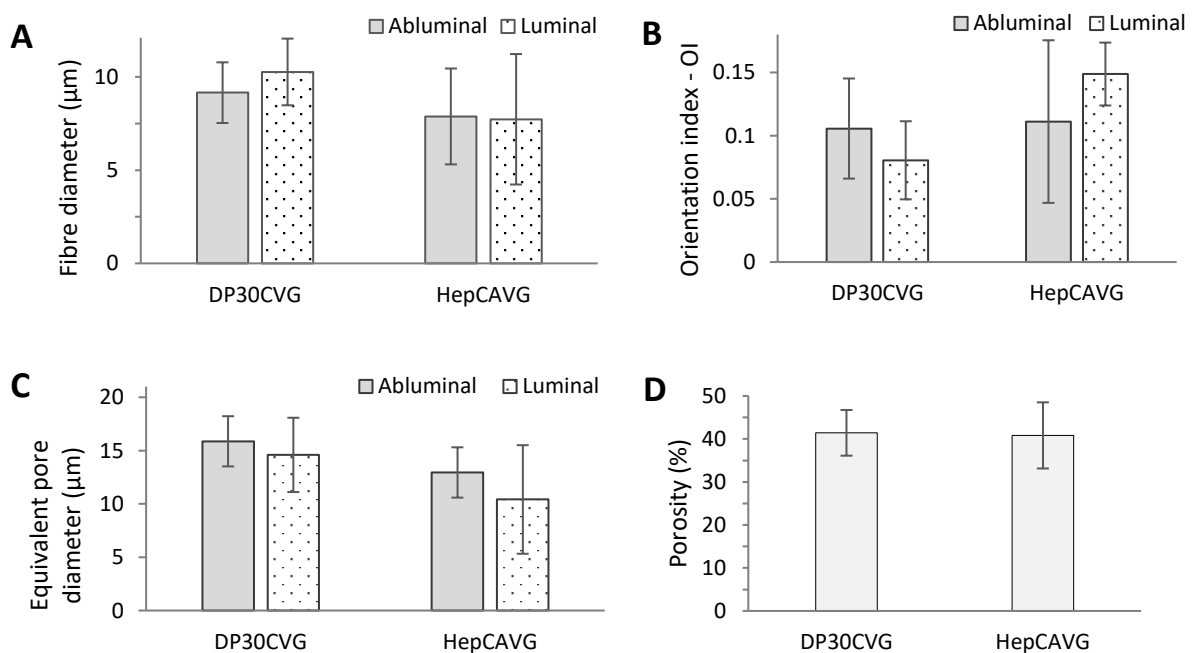
Figure 58: Morphological characteristics of DP30CVG and HepCAVG. A) Fibre diameter.   B) Orientation index. C) Pore size. D) Porosity.

3.7.1.2 Fibre orientation

There was no statistically significant difference (P = 0.2) in fibre orientation index between the two groups of vascular grafts which had a mean fibre OI (Figure 58B) of 0.11 ± 0.05. Even though more randomly aligned fibres (lower OI) were expected among the coaxial group compared to the control group on account of increased whipping and jet stretching due to the addition of water and heparin, this was probably negated by the small mandrel diameter and slow rotational speed, producing similar OIs for the two groups.

No statistical difference was observed between the OI of coaxial scaffold sheets (LoHepCA) and vascular grafts (HepCAVG). The DP30CTRL scaffold sheets however had a 35.6 % (P = 0.5) and 54.3 % (P = 0.02) larger mean OI on its abluminal and luminal surfaces respectively, compared to its vascular graft counterpart (DP30CVG). Therefore, it was possible to translate the electrospinning processes to smaller mandrels without resulting in an OI increase. With

low mean OIs (< 0.2), the vascular grafts indicated little sign of fibre alignment. The randomly aligned fibres mimic the natural ECM and suggest anisotropic mechanical behaviour.

3.7.1.3   Pore size

The vascular grafts had mean equivalent pore diameters of 15.9±2.4 µm and 14.6±3.5 µm on the abluminal and luminal surface respectively of DP30CVG, and 13.0±2.4 µm and 10.4±5.1 µm on the abluminal and luminal surface of HepCAVG. There were no statistically significant differences between the pore sizes of the groups or surfaces.

The translation of DP30 control scaffolds from sheets to grafts did not result in a difference in pore size while coaxial grafts presented a significant 43.8 % (P = 10^{-4}) increase in pore size. This increase in pore size is ascribed to the significantly larger fibre diameters of the coaxial vascular grafts (HepCAVG) compared to sheets obtained from spinning on a larger mandrel (LoHepCA).

3.7.1.4   Porosity

The DP30CVG and HepCAVG group had similar mean porosities of 41.4±5.3 % and 40.8±7.7 % (P = 0.9) as illustrated in Figure 58D.

Contrary to scaffold sheets, the produced vascular grafts had no difference in porosity between control and coaxial groups. Both sets of grafts, however, presented a decrease in porosity with the translation from scaffold sheets to vascular grafts. Porosities were approximately 35 % lower (P = 5 × 10^{-5}) for the control group (DP30CTRL to DP30CVG) and 23 % lower (P = 0.04) for the coaxial group (LoHepCA to HepCAVG). These lower porosities suggest a higher magnitude of fibre fusion (confirmed by observing Figure 57). These lower porosities agree with a previous unpublished thesis conducted by this research group, where DP30/CHCl$_3$ vascular grafts had porosities of 44±7 % [206].

3.7.2   Mechanical properties

3.7.2.1   Ultimate tensile stress

The ultimate tensile stresses of produced vascular grafts are shown in Figure 59A. Longitudinal UTS of 1.80±0.43 MPa and 1.77±0.62 MPa were exhibited by the DP30CVG and HepCAVG groups respectively. For tubular structures such as grafts, the circumferential UTS is equal to the hoop stress and therefore DP30CVG and HepCAVG had mean hoop stresses of 2.75±0.23 MPa and the 3.54±0.72 MPa.

There was no statistically significant difference between the circumferential (P = 0.2) or longitudinal (P = 0.96) stresses of groups. When comparing the directional stresses within groups, DP30CVG and HepCAVG respectively had 52.5 % (P = 0.02) and 99.6 % (P = 0.1) higher UTS in the circumferential direction.

Similar to scaffold sheets, there was no difference between the groups in the same direction. However, unlike scaffold sheets, the notably higher UTS in the circumferential direction suggests some alignment of fibres in the circumferential direction rather than the longitudinal (corresponding to the OI = 0.1 - 0.2).
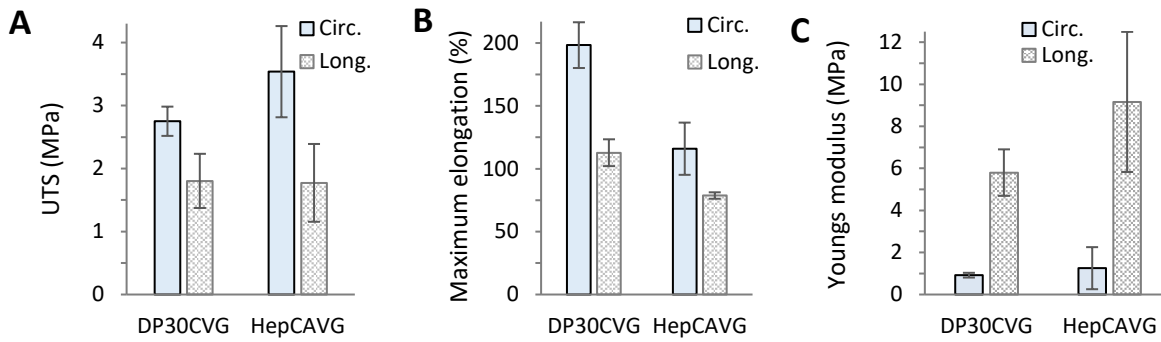
Figure 59: Circumferential and longitudinal A) ultimate tensile stress, B) maximum elongation (%) and C) Youngs modulus of produced vascular grafts.

The translation from sheets to grafts resulted in no change in the longitudinal UTS but resulted in an increase in the circumferential UTS. DP30CVG exhibited a two-and-a-half-fold increase (P = 0.0001) in the circumferential UTS and HepCAVG exhibited a three-fold increase (P = 0.01). When compared to scaffold sheets from the larger mandrel, the overall higher UTS of vascular grafts indicate the higher degree of fibre fusion, which is known to affect UTS. These higher UTSs are more comparable to native vasculature compared to cut sheets [40].

3.7.2.2 Maximum elongation

The maximum elongation (ε_{max}) of the DP30CVG and HepCAVG groups (Figure 59B) were 198.3±18.2 % and 116.0±20.8 % in the circumferential direction and 112.8±10.7 % and 78.7±2.6 % in the longitudinal direction respectively. Compared to HepCAVG, DP30 control grafts showed significantly superior ε_{max}, with the circumferential and longitudinal ε_{max} of HepCAVG, respectively 41.5 % (P = 0.0006) and 30.2 % (P = 0.2) less than the DP30CVGs'. To some extent, this decrease could be explained by a higher degree of fibre fusion (motivated by the corresponding higher UTS).

The translation of the DP30 control group from sheets to grafts resulted in a significant decrease of 25.5 % in the longitudinal percentage of maximum elongation. Otherwise, the translation did not affect ε_{max}. The noteworthy lower ε_{max} in the longitudinal direction suggests alignment in the circumferential direction. Even though the maximum elongation in the longitudinal direction might seem low, it is important to note that it is common in native vasculature for the longitudinal strain at failure to be only a fraction of the circumferential direction's e.g. the ratio $\frac{long.\varepsilon_{max}}{circ.\varepsilon_{max}}$ is 0.44 for IMA and 0.46 for SV [312].

3.7.2.3 Youngs modulus

The Youngs modulus was higher (P < 0.004) in the longitudinal direction for both groups (6× for DP30VG and 7x for HepCAVG). There was no difference between the groups in the same direction with a mean E_Y of 1.06±0.87 MPa and 6.92±2.65 MPa in the circumferential and longitudinal direction, respectively. When consulting the E_Y values in Table 1 for native vasculature, it is evident that it is normal for the longitudinal direction of a tubular structure to have a higher E_Y, and that E_Y for produced grafts are significantly less compared to native vasculature. The translation from a larger to a smaller mandrel did not affect the longitudinal E_Y but did result in a more than 2.5-fold decrease (P < 0.02) in circumferential E_Y.

3.7.2.4 Burst pressure and compliance

The theoretical burst pressures (Figure 60A) of DP30CVG and HepCAVG were determined to be 54312±119 mmHg and 4322±1680 mmHg. Thin-walled cylinder theory, implemented to confirm the burst pressure, resulted in a slightly lower bust pressure (10.5 % less, P = 0.006) for the DP30 control group. These more conservative values (thin-walled) were selected as the burst pressures (DP30CVG = 4859.07±90.02 MPa, HepCAVG = 4299.54±1546.13 MPa) and the thin-walled cylinder theory was subsequently used to determine compliance.

The compliance estimated for DP30CVG and HepCAVG were 5.3±0.5 %/100mmHg and 7.2±1.2 %/100mmHg as shown in Figure 60B. There was no statistically significant difference between the compliance of the groups (P = 0.1).
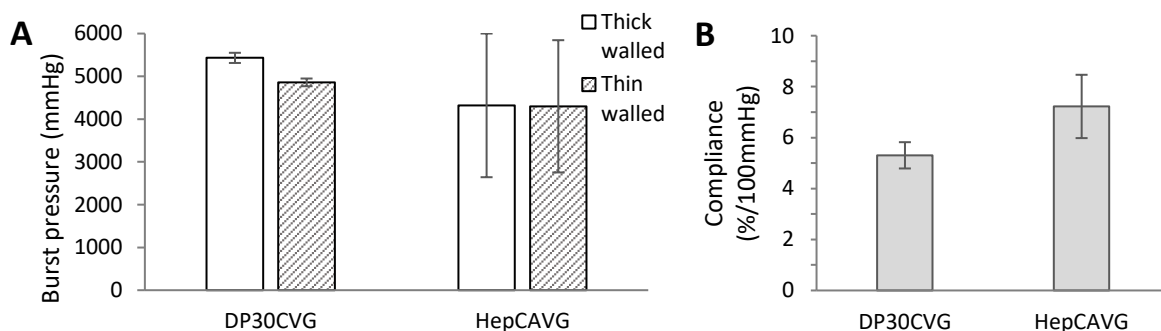
Figure 60: A) Burst pressure using thin and thick-walled cylinder theory and B) compliance of produced vascular grafts

The burst pressures of grafts from the DP30CVG and HepCAVG were respectively, 40 and 35 times higher than the diastolic blood pressure of a healthy human (120 mmHg) and also much higher than burst pressures documented for the human IMA (3196 mmHg) and SV (1680–3900 mmHg) [105, 110]. Previous unpublished studies [206] by this research group showed that decreased porosity, together with increased thickness, results in increased burst pressure, therefore explaining the very high burst pressures observed. Burst pressure is also proportional to the UTS since it is used in the calculation and thus the notably large error of the coaxial groups is a result of the larger error of the circumferential UTS. The burst pressure is furthermore also directly related to the wall thickness to radius ratio.

According to Tai et al., the compliance range for healthy femoral and popliteal arteries is 6 – 12 %/100 mmHg at a normal blood pressure of 120/80 mmHg [112]. The average compliance of the two groups, 6.3 %/100 mmHg, is at the lower end of this, but still within the range. Moreover, the resulting compliances are higher than recently documented compliance values for the SV of 0.7–1.5%/100 mmHg and standard ePTFE grafts of 0.1%/100 mmHg [258, 313]. The compliance should however ideally be higher, as the current low value means the grafts are stiffer than healthy blood vessels and could negatively affect blood flow.

Since the burst pressure is so much higher and the compliance is lower than the required range, a feasible solution might be to balance these two factors. Both are a result of thick walls, low porosity and high fibre fusion subsequently resulting in high UTS and poor elasticity (strain response). Therefore future work should aim to increase porosity, reduce fibre fusion and ultimately find the ideal stress-strain response for healthy compliance and burst pressure.

4 Conclusion

This chapter concludes the investigation on the development of and drug incorporation into degradable tissue engineering scaffolds for vascular graft applications.

- The electrospinning setup was successfully upgraded through replacement of components (motors, drivers, limit switches), altered rig layout and the implementation of coaxial electrospinning technology (designed and manufactured coxial needles) to allow various methods of electrospinning.

- The conditions for coaxial electrospinning of degradable polymers (DP30) with water-soluble cores were determined to produce scaffolds with a core-shell morphology: $\dot{V}_{shell}$ = 2.1-2.6 ml/h, $\dot{V}_{core}$ = 0.3-0.5 ml/h, V_+ = 15-17 kV, V_- = -5 - -1 kV, TCD = 25-30 cm, rH = 30-35 %, Needle size = 17 G × 24 G, $\omega_{rotational}$ = 70-150 RPM.

- Five groups of scaffold sheets (cut grafts with ID = 25 mm) were electrospun including: i) DP30 controls, ii) 0.6wt% HepTBA blend electrospun DP30 scaffolds and coaxially electrospun DP30 scaffolds with iii) 0.6 wt% $HepNa^+$ content, iv) 0.3 wt% $HepNa^+$ content and v) no heparin content in the PEO (400 kDa) core.

- Morphological analysis showed that the coaxial electrospinning of DP30 with a water core and especially the addition of HepNa+ resulted in a decrease in fibre diameter, OI, pore size and porosity, which was most likely resulting due to the addition of water and a charged salt to the polymer solutions increasing the conductivity and dielectric constant.

- Fibres of all coaxially electrospun scaffolds yielded visible holes (washed out cores) in fibres after washing, which confirmed the presence of a distinct core-shell morphology. The cores were most prominent in scaffolds with PEO cores (no heparin included).

- Static water contact angle measurements showed that the electrospun scaffolds were more hydrophobic than cast DP30 films. DP30 was classified as hydrophobic since $\theta > 90\,°$, however, DP30 exhibited a significant magnitude of polymer swelling in water within a short period.

- Similar mechanical properties were obtained when $HepNa^+$ was coaxially incorporated, compared to control samples, (0.85 MPa - 1.87 MPa, ε_{max} = 105 % - 209 %, E = 2.5 MPa - 10 MPa, SR = 2.4 N - 3.7 N). In general, scaffolds did not prove adequate UTS compared to native arteries but did however show similar elongation response. With a few minor exceptions, there was no significant difference between the circumferential and longitudinal mechanical properties, which confirmed the anisotropic nature of the scaffolds.

- Irrespective of the groups, thermal analyses from DSC showed similar thermograms with little variation between groups. The electrospinning process did not unduly affect the thermal properties, and thus crystallinity, of DP30.

- After 6 weeks of in vitro degradation, all scaffolds experienced a decrease in mechanical properties ($UTS_{loss} \approx 40\ \%$, $\varepsilon_{max,loss} \approx 80\ \%$), but no major changes in the Youngs modulus. Samples showed minor changes in thermal properties over time but no obvious changes were observed in transition temperatures and enthalpies.

- Blend electrospun scaffolds showed the expected initial burst release of HepTBA followed by a sustained release. Coaxially incorporated $HepNa^+$ also exhibited burst release for both

the low and high heparin content groups followed by a more obvious sustained release than HepTBA. Coaxial incorporation proved to have a 2× higher heparin encapsulation efficiency than blend incorporation with efficacies approaching 100 %.

- Heparin, post-TBA-modification, did not fully retain its antithrombotic properties, which was further reduced after incorporation by electrospinning and release. HepNa$^+$, however, retained its full antithrombotic properties post coaxial electrospinning as an eluate.

- In a pilot translational study, two sets of electrospun DP30 vascular grafts (ID = 2.6 mm) were produced: i) a control group and ii) a group with coaxially incorporated HepNa$^+$/PEO (400 kDa). Overall, the translation to a smaller mandrel resulted in increased fibre diameters and OIs (alignment in the circumferential direction); and decreased porosities. The vascular grafts proved burst pressures superior to native vasculature and compliances edging upon the lower margin for healthy arteries.

- Although a larger than anticipated initial burst release occurred for coaxially electrospun fibres, a sustained release was obtained over 6 weeks. The coaxial electrospinning process allows the incorporation of heparin without the need for modification, and it also retains the full bioactivity of the heparin after electrospinning incorporation and elution, despite not being as effective (linear sustained release) as expected in this case. Therefore, coaxial electrospinning of heparin in DP30 shows potential for producing small-diameter vascular grafts with properties comparable to small blood vessels.

5 Recommendations

During the development of heparin-eluting scaffolds for vascular graft application, additional opportunities arose that warrant further investigation, some directly related and others outside the scope and time of this project. Therefore, this section provides recommendations for the continuation of the current research concerning specific subtopics.

The suggestions below are to improve knowledge towards developing heparin-eluting polyurethane (DP30) scaffolds for tissue engineering that would promote the desired host healing response as vascular grafts:

Processing parameters for coaxial electrospinning

- Due to the low durability (exposure to organic solvents) of produced coaxial electrospinning needles, it is recommended that coaxial needles should be manufactured and welded to ensure robustness and concentricity. Furthermore, various sets with ranging gauge sizes and combinations at various lengths could be made to investigate the observed effects of needle size and length.

- During the final stages of electrospinning scaffolds, it was observed that an additional parameter, the vertical placement of the mandrel relative to the needle, had a notable influence on the coaxial electrospinning outcome. It was observed that elevating the mandrel (by elevating the translational / rotating stage) ensured a more steady Taylor cone. It is recommended that future studies should conduct a parametric study to determine the effect of elevation and the optimal angle for spinning upwards. This could lower the required negative voltage on the mandrel to ensure fibre deposition and therefore reduce the magnitude of wet landing.

Solution parameters for coaxial electrospinning

- Solvents for DP30, other than $CHCl_3$, have been identified e.g. HFIP, DCE, TFE. Initial investigation proved that the addition of these solvents could allow for further manipulation of electrospinning parameters to acquire desired morphological and mechanical characteristics during the electrospinning process as it could change the dielectric constants, vapour pressure and volatility. Therefore, it is recommended to investigate the possible use of these solvents with various combinations/ratios.

- Establishing the ratio of water to ethanol (EtOH) in the core solution, currently DI Water/EtOH (60:40), is a balancing act between increased water concentration allowing a higher $HepNa^+$ content and increased spinnability (as higher water content makes spinning more unstable). Since the maximum quantity of $HepNa^+$ that could be incorporated was limited by its solubility in EtOH, future studies should focus on reducing the EtOH concentration in the core solution to allow for more drug to be successfully mixed, while investigating parameters that would ease spinnability.

Confirmation of core-shell morphology

- The core-shell morphology can be further investigated through blending (fluorescent) dyes such as Rhodamine B and Fluorescein into electrospinning solutions and observing the resulting scaffolds via fluorescent microscopy.

- The fibres could also be individually imaged by transmission electron microscope (TEM) to confirm the core-shell morphology.

Differential scanning calorimetry (DSC)

- More exact thermal properties and comparison can be determined as well as the effect of degradation by increasing the sample sizes for DSC analysis.

Heparin elution study

- A study that might shed more light on the drug release response of the coaxially electrospun scaffolds, would be to attempt emulsion electrospinning of DP30 and heparin to allow direct comparison. This could test the superiority of the coaxial incorporation method.

- It is recommended that the elution study should be performed until the scaffolds have completely degraded to confirm the drug release efficacy associated with scaffold production techniques (blend vs coaxial). The remaining quantity of heparin after the 6 week period would be known as well as the percentage released of the total incorporated.

- A portion of the initial burst release of coaxial groups might be due to the cross-sections not being sealed off. It is important to note that 48h of (vigorous) washing resulted in visible holes in cut fibres. Therefore, to some extent, the initial release might not only be due to diffusion through the fibres shell but leaking at the open end of a fibre as well. It is suggested that to exclude this release, the edges of scaffold samples should be dipped in a non-degradable polyurethane solution (e.g. Pellethane®) to ensure cut fibre edges are sealed off.

Heparin activity

- Future studies establishing heparin activity using TEG are recommended to include larger samples sizes for improving statistical power.

- The use of various concentrations of blood treatment groups are suggested when performing TEGs to confirm the validity of bioactivity results (e.g. 0.05 mg/ml and 0.18 mg/ml of each treatment).

- The effect of time on the activity of heparin eluted from scaffolds can be determined by performing TEGs on eluates from different days of the elution study (e.g. days 2, 14 and 42).

Future in vivo studies

- The short-term in vivo healing response can be evaluated by implanting the vascular grafts in a rat infrarenal aortic implantation model. This will also act as confirmation of whether an adequate quantity of drug has been incorporated and whether it is still active by comparison of patency and healing response.

- Subsequently, the effects of heparin (HepNa+ and HepTBA) incorporated scaffolds in a long-term study can be investigated with the isolated intrarenal loop model (previously established by this research group [116, 314]) to determine its healing response and to distinguish between transanastomotic (TA) and transmural (TM) endothelialisation.

References

1.   Roth GA, Abate D, Abate KH, Abay SM, Abbafati C, Abbasi N, et al. Global, regional, and national age-sex-specific mortality for 282 causes of death in 195 countries and territories, 1980-2017: a systematic analysis for the Global Burden of Disease Study 2017. The Lancet. 2018; 392(10159): p. 1736-1788.

2.   Kaptoge S, Pennells L, De Bacquer D, Cooney MT, Kavousi M, Stevens G, et al. World Health Organization cardiovascular disease risk charts: revised models to estimate risk in 21 global regions. The Lancet Global Health. 2019; 7(10): p. e1332-e1345.

3.   Wyk V, Laubscher R, Msemburi W, Dorrington R, Groenewald P, Vos T, et al. Second South African National Burden of Disease Study: Cause-of-death profile for South Africa. 2014. Cape Town: South African Medical Research Council.

4.   Sivadasanpillai H, Leeder S, M H, Jeemon P, Dorairaj P. A race against time: The Challenge of Cardiovascular Diseases in Developing Economies. 2015. New York: Columbia University.

5.   Wilkins E, Wilson L, Wickramasinghe K, Bhatnagar P, Leal J, Luengo-Fernandez R, et al. European Cardiovascular Disease Statistics 2017. 2017. European Heart Network: Brussels.

6.   Movsisyan NK, Vinciguerra M, Medina-Inojosa JR, Lopez-Jimenez F. Cardiovascular Diseases in Central and Eastern Europe: A Call for More Surveillance and Evidence-Based Health Promotion. Annals of global health. 2020; 86(1): p. 21-21.

7.   Virani SS, Alonso A, Benjamin EJ, Bittencourt MS, Callaway CW, Carson AP, et al. Heart Disease and Stroke Statistics 2020 Update: A Report From the American Heart Association. Circulation. 2020; 141(9): p. e139-e596.

8.   Benjamin EJ, Virani SS, Callaway CW, Chamberlain AM, Chang AR, Cheng S, et al. Heart Disease and Stroke Statistics-2018 Update: A Report From the American Heart Association. Circulation. 2018; 137(12): p. e67-e492.

9.   World Health Organization. Global status report on noncommunicable diseases 2014. WHO. 2014(18 August).

10.   Schoen FJ, Fioretta ES, Mallone A, Smits AIPM, Klouda L, Bouten CVC. Vascular Tissue Engineering: Pathological Considerations, Mechanisms, and Translational Implications. in Tissue-Engineered Vascular Grafts. B.H. Walpoth, et al. Editors. 2020. Springer International Publishing: Cham. p. 95-134.

11.   Wagenseil JE, Mecham RP. Vascular extracellular matrix and arterial mechanics. Physiological reviews. 2009; 89(3): p. 957-989.

12.   Chow M-J, Turcotte R, Lin CP, Zhang Y. Arterial extracellular matrix: a mechanobiological study of the contributions and interactions of elastin and collagen. Biophysical journal. 2014; 106(12): p. 2684-2692.

13.   ER Services. Structure and Function of Blood Vessels. Module 4: The Cardiovascular System: Blood Vessels and Circulation 2020 [cited 2020 20 November 2020]; Available from: https://courses.lumenlearning.com/suny-ap2/chapter/structure-and-function-of-blood-vessels/.

14.   Khan OF, Sefton MV. Endothelialized biomaterials for tissue engineering applications in vivo. Trends in biotechnology. 2011; 29(8): p. 379-387.

15.   Li S, Henry JJD. Nonthrombogenic Approaches to Cardiovascular Bioengineering. Annual Review of Biomedical Engineering. 2011; 13(1): p. 451-475.

16. Mitchell R. Blood Vessels. in Robbins and Cotran pathologic basis of disease. V. Kumar, et al. Editors. 2015. Elsevier/Saunders: Philadelphia, PA.

17. Ross R. Atherosclerosis — An Inflammatory Disease. New England Journal of Medicine. 1999; 340(2): p. 115-126.

18. Moore Kathryn J, Tabas I. Macrophages in the Pathogenesis of Atherosclerosis. Cell. 2011; 145(3): p. 341-355.

19. Fowkes FGR, Rudan D, Rudan I, Aboyans V, Denenberg JO, McDermott MM, et al. Comparison of global estimates of prevalence and risk factors for peripheral artery disease in 2000 and 2010: a systematic review and analysis. The Lancet. 2013; 382(9901): p. 1329-1340.

20. Libby P, Theroux P. Pathophysiology of coronary artery disease. Circulation. 2005; 111(25): p. 3481-8.

21. Kreatsoulas C, Shannon HS, Giacomini M, Velianou JL, Anand SS. Reconstructing angina: cardiac symptoms are the same in women and men. JAMA Intern Med. 2013; 173(9): p. 829-31.

22. Pennel T, Zilla P. Clinical Applications and Limitations of Vascular Grafts. in Tissue-Engineered Vascular Grafts. B.H. Walpoth, et al. Editors. 2020. Springer International Publishing: Cham. p. 3-34.

23. Hirsch AT, Criqui MH, Treat-Jacobson D, Regensteiner JG, Creager MA, Olin JW, et al. Peripheral arterial disease detection, awareness, and treatment in primary care. Jama. 2001; 286(11): p. 1317-24.

24. Mallis P, Kostakis A, Stavropoulos-Giokas C, Michalopoulos E. Future Perspectives in Small-Diameter Vascular Graft Engineering. Bioengineering. 2020; 7(4): p. 160.

25. Bhat TM, Afari ME, Garcia LA. Atherectomy in Peripheral Artery Disease: A Review. J Invasive Cardiol. 2017; 29(4): p. 135-144.

26. Matsuzaki Y, John K, Shoji T, Shinoka T. The Evolution of Tissue Engineered Vascular Graft Technologies: From Preclinical Trials to Advancing Patient Care. Appl Sci (Basel). 2019; 9(7).

27. Pashneh-Tala S, MacNeil S, Claeyssens F. The Tissue-Engineered Vascular Graft-Past, Present, and Future. Tissue Eng Part B Rev. 2016; 22(1): p. 68-100.

28. Patel MR, Calhoon JH, Dehmer GJ, Grantham JA, Maddox TM, Maron DJ, et al. ACC/AATS/AHA/ASE/ASNC/SCAI/SCCT/STS 2017 Appropriate Use Criteria for Coronary Revascularization in Patients With Stable Ischemic Heart Disease: A Report of the American College of Cardiology Appropriate Use Criteria Task Force, American Association for Thoracic Surgery, American Heart Association, American Society of Echocardiography, American Society of Nuclear Cardiology, Society for Cardiovascular Angiography and Interventions, Society of Cardiovascular Computed Tomography, and Society of Thoracic Surgeons. Journal of the American College of Cardiology. 2017; 69(17): p. 2212-2241.

29. NN Medical Services Ltd. Angioplasty and Stenting - Pain Free Walking. 2021 [cited 2021 27 March]; Available from: https://radiology.wales/angioplasty-and-stenting/.

30. National Heart, Lung, and Blood Institute (NHLBI). Stents. [cited 2021 28 January]; Available from: https://www.nhlbi.nih.gov/health-topics/stents.

31. Allina Health. Coronary artery bypass surgery (CAB). 2017; Available from: https://www.allinahealth.org/health-conditions-and-treatments/health-library/patient-education/helping-your-heart/tests-and-procedures/coronary-artery-bypass-surgery.

32. Grand View Research. Vascular Grafts Market Size, Share & Trends Analysis Report By Product (Peripheral, Endovascular Stent), By Application (Vascular Occlusion, Cardiac Aneurysms), By Raw Material (PTFE, Polyester), And Segment Forecasts, 2019 - 2026. 2019. Grand View Research: San Francisco. p. 1 - 80.

33. Harskamp RE, Lopes RD, Baisden CE, de Winter RJ, Alexander JH. Saphenous vein graft failure after coronary artery bypass surgery: pathophysiology, management, and future directions. Ann Surg. 2013; 257(5): p. 824-33.

34. Simionescu A, Schulte JB, Fercana G, Simionescu DT. Inflammation in cardiovascular tissue engineering: the challenge to a promise: a minireview. International journal of inflammation. 2011; 2011: p. 958247-958247.

35. Gong W, Lei D, Li S, Huang P, Qi Q, Sun Y, et al. Hybrid small-diameter vascular grafts: Anti-expansion effect of electrospun poly ε-caprolactone on heparin-coated decellularized matrices. Biomaterials. 2016; 76: p. 359-70.

36. Ravi S, Chaikof EL. Biomaterials for vascular tissue engineering. Regenerative medicine. 2010; 5(1): p. 107-120.

37. G N, Tan A, Gundogan B, Farhatnia Y, Nayyer L, Mahdibeiraghdar S, et al. Tissue engineering vascular grafts a fortiori: looking back and going forward. Expert Opinion on Biological Therapy. 2015; 15(2): p. 231-244.

38. Carrabba M, Madeddu P. Current Strategies for the Manufacture of Small Size Tissue Engineering Vascular Grafts. Frontiers in bioengineering and biotechnology. 2018; 6: p. 41-41.

39. Catto V, Farè S, Freddi G, Tanzi MC. Vascular Tissue Engineering: Recent Advances in Small Diameter Blood Vessel Regeneration. ISRN Vascular Medicine. 2014; 2014: p. 923030.

40. Hasan A, Memic A, Annabi N, Hossain M, Paul A, Dokmeci MR, et al. Electrospun scaffolds for tissue engineering of vascular grafts. Acta Biomaterialia. 2014; 10(1): p. 11-25.

41. Elliott MB, Ginn B, Fukunishi T, Bedja D, Suresh A, Chen T, et al. Regenerative and durable small-diameter graft as an arterial conduit. Proceedings of the National Academy of Sciences. 2019; 116(26): p. 12710-12719.

42. Carrel A, Guthrie CC. Uniterminal and biterminal venous transplantations. Surg Gynecol Obstet. 1906; 2: p. 266-268.

43. Carrel A. RESULTS OF THE TRANSPLANTATION OF BLOOD VESSELS, ORGANS AND LIMBS. Journal of the American Medical Association. 1908; LI(20): p. 1662-1667.

44. Gross RE, Hurwitt ES, Bill AH, Peirce EC. Preliminary Observations on the Use of Human Arterial Grafts in the Treatment of Certain Cardiovascular Defects. New England Journal of Medicine. 1948; 239(16): p. 578-579.

45. Kunlin J. Le traitement de l'ischémie artéritique par la greffe veineuse longue [Long vein transplantation in treatment of ischemia caused by arteritis]. Rev Chir. 1951; 70(7-8): p. 206-35.

46. Dubost C, Allary M, Oeconomos N. Resection of an aneurysm of the abdominal aorta: reestablishment of the continuity by a preserved human arterial graft, with result after five months. AMA Arch Surg. 1952; 64(3): p. 405-8.

47. Cooper DKC, Ekser B, Tector AJ. A brief history of clinical xenotransplantation. Int J Surg. 2015; 23(Pt B): p. 205-210.

48. Lindsey P, Echeverria A, Cheung M, Kfoury E, Bechara CF, Lin PH. Lower Extremity Bypass Using Bovine Carotid Artery Graft (Artegraft): An Analysis of 124 Cases with Long-Term Results. World J Surg. 2018; 42(1): p. 295-301.

49. Gharamti A, Kanafani ZA. Vascular Graft Infections: An update. Infect Dis Clin North Am. 2018; 32(4): p. 789-809.

50. Reilly B, Khan S, Dosluoglu H, Harris L, O'Brien-Irr M, Lukan J, et al. Comparison of Autologous Vein and Bovine Carotid Artery Graft as a Bypass Conduit in Arterial Trauma. Ann Vasc Surg. 2019; 61: p. 246-253.

51. Desai M, Hamilton G. Graft materials past and future. in Mechanisms of Vascular Disease: A Reference Book for Vascular Specialists. M. Thompson and R. Fitridge. Editors. 2011. The University of Adelaide Press. p. 511-536.

52. Iyer KS. The Contegra bovine jugular valved conduit: Living up to expectations? Annals of pediatric cardiology. 2012; 5(1): p. 34-35.

53. Blakemore AH, Voorhees AB, Jr. The use of tubes constructed from vinyon N cloth in bridging arterial defects; experimental and clinical. Annals of surgery. 1954; 140(3): p. 324-334.

54. Voorhees AB, Jr., Jaretzki A, 3rd, Blakemore AH. The use of tubes constructed from vinyon "N" cloth in bridging arterial defects. Annals of surgery. 1952; 135(3): p. 332-336.

55. Hacker MC, Mikos AG. 35 - Synthetic Polymers. in Principles of Regenerative Medicine. A. Atala, et al. Editors. 2008. Academic Press: San Diego. p. 604-635.

56. DeBakey ME. Clinical application of a new flexible knitted Dacron arterial substitute. Am Surg. 2008; 74(5): p. 387.

57. Goldman M, McCollum CN, Hawker RJ, Drolc Z, Slaney G. Dacron arterial grafts: the influence of porosity, velour, and maturity on thrombogenicity. Surgery. 1982; 92(6): p. 947-52.

58. Xue L, Greisler HP. Biomaterials in the development and future of vascular grafts. J Vasc Surg. 2003; 37(2): p. 472-80.

59. Xue J, Wu T, Dai Y, Xia Y. Electrospinning and Electrospun Nanofibers: Methods, Materials, and Applications. Chemical Reviews. 2019; 119(8): p. 5298-5415.

60. Yao JS, Eskandari MK. Accidental discovery: the polytetrafluoroethylene graft. Surgery. 2012; 151(1): p. 126-8.

61. Soyer T, Lempinen M, Cooper P, Norton L, Eiseman B. A new venous prosthesis. Surgery. 1972; 72(6): p. 864-72.

62. Al Meslmani B, Mahmoud G, Strehlow B, Mohr E, Leichtweiß T, Bakowsky U. Development of thrombus-resistant and cell compatible crimped polyethylene terephthalate cardiovascular grafts using surface co-immobilized heparin and collagen. Materials science & engineering. C, Materials for biological applications. 2014; 43C: p. 538-546.

63. Fischer P, Fabian T, De Rijk W, Edwards N, DeCuypere M, Landis R, et al. Prosthetic Vascular Conduit in Contaminated Fields: A New Technology to Decrease ePTFE Infections. The American surgeon. 2008; 74: p. 524-8; discussion 528.

64. Friedman SG, Lazzaro RS, Spier LN, Moccio C, Tortolani AJ. A prospective randomized comparison of Dacron and polytetrafluoroethylene aortic bifurcation grafts. Surgery. 1995; 117(1): p. 7-10.

65. Green RM, Abbott WM, Matsumoto T, Wheeler JR, Miller N, Veith FJ, et al. Prosthetic above-knee femoropopliteal bypass grafting: five-year results of a randomized trial. J Vasc Surg. 2000; 31(3): p. 417-25.

66. King WE, Minden-Birkenmaier BA, Bowlin GL. Synthetic Materials: Processing and Surface Modifications for Vascular Tissue Engineering. in Tissue-Engineered Vascular Grafts. B.H. Walpoth, et al. Editors. 2020. Springer International Publishing: Cham. p. 137-186.

67. Post S, Kraus T, Müller-Reinartz U, Weiss C, Kortmann H, Quentmeier A, et al. Dacron vs. polytetrafluoroethylene grafts for femoropopliteal bypass: a prospective randomised multicentre trial. Eur J Vasc Endovasc Surg. 2001; 22(3): p. 226-31.

68. Roll S, Müller-Nordhorn J, Keil T, Scholz H, Eidt D, Greiner W, et al. Dacron vs. PTFE as bypass materials in peripheral vascular surgery--systematic review and meta-analysis. BMC surgery. 2008; 8: p. 22-22.

69. Salacinski HJ, Goldner S, Giudiceandrea A, Hamilton G, Seifalian AM, Edwards A, et al. The mechanical behavior of vascular grafts: a review. J Biomater Appl. 2001; 15(3): p. 241-78.

70. Dahl SLM, Kypson AP, Lawson JH, Blum JL, Strader JT, Li Y, et al. Readily Available Tissue-Engineered Vascular Grafts. Science Translational Medicine. 2011; 3(68): p. 68ra9.

71. Pennel T, Zilla P, Bezuidenhout D. Biomaterials in vascular graft surgery. 2016.

72. Kannan RY, Salacinski HJ, Butler PE, Hamilton G, Seifalian AM. Current status of prosthetic bypass grafts: A review. Journal of Biomedical Materials Research Part B: Applied Biomaterials. 2005; 74B(1): p. 570-581.

73. Bezuidenhout D, Davies N, Zilla P. Effect of well defined dodecahedral porosity on inflammation and angiogenesis. Asaio j. 2002; 48(5): p. 465-71.

74. Lanza R, Langer R, Vacanti JP, Atala A. Principles of tissue engineering. 2020: Academic press.

75. Weinberg CB, Bell E. A blood vessel model constructed from collagen and cultured vascular cells. Science. 1986; 231(4736): p. 397-400.

76. Niklason LE, Langer RS. Advances in tissue engineering of blood vessels and other tissues. Transplant Immunology. 1997; 5(4): p. 303-306.

77. Vacanti JP, Langer R. Tissue engineering: the design and fabrication of living replacement devices for surgical reconstruction and transplantation. The Lancet. 1999; 354: p. S32-S34.

78. Dzobo K, Thomford NE, Senthebane D, Shipanga H, Rowe A, Dandara C, et al. Advances in Regenerative Medicine and Tissue Engineering: Innovation and Transformation of Medicine. Stem Cells International. 2018; 2018: p. 1-24.

79. Yuan H, Chen C, Liu Y, Lu T, Wu Z. Strategies in cell-free tissue-engineered vascular grafts. J Biomed Mater Res A. 2020; 108(3): p. 426-445.

80. Bezuidenhout D, Human P, Zilla P. Prosthetic vascular grafts: wrong models, wrong questions and no healing. Biomaterials. 2007; 28(34): p. 5009-27.

81. Roh JD, Sawh-Martinez R, Brennan MP, Jay SM, Devine L, Rao DA, et al. Tissue-engineered vascular grafts transform into mature blood vessels via an inflammation-mediated process of vascular remodeling. Proceedings of the National Academy of Sciences. 2010; 107(10): p. 4669-4674.

82.   Walpoth BH, de Valence S, Tille J-C, Mugnai D, Sologashvili T, Mrówczyński W, et al. In Vivo Tissue-Engineered Vascular Grafts. in Tissue-Engineered Vascular Grafts. B.H. Walpoth, et al. Editors. 2020. Springer International Publishing: Cham. p. 187-206.

83.   de Valence S, Tille J-C, Mugnai D, Mrowczynski W, Gurny R, Möller M, et al. Long term performance of polycaprolactone vascular grafts in a rat abdominal aorta replacement model. Biomaterials. 2012; 33(1): p. 38-47.

84.   Mugnai D, Tille JC, Mrówczyński W, de Valence S, Montet X, Möller M, et al. Experimental noninferiority trial of synthetic small-caliber biodegradable versus stable vascular grafts. J Thorac Cardiovasc Surg. 2013; 146(2): p. 400-7.e1.

85.   Dimitrievska S, Niklason LE. Historical Perspective and Future Direction of Blood Vessel Developments. Cold Spring Harb Perspect Med. 2018; 8(2).

86.   Niklason LE, Lawson JH. Bioengineered human blood vessels. Science. 2020; 370(6513).

87.   Boethig D, Horke A, Hazekamp M, Meyns B, Rega F, Van Puyvelde J, et al. A European study on decellularized homografts for pulmonary valve replacement: initial results from the prospective ESPOIR Trial and ESPOIR Registry data†. Eur J Cardiothorac Surg. 2019; 56(3): p. 503-509.

88.   Schmidli J, Savolainen H, Heller G, Widmer MK, Then-Schlagau U, Baumgartner I, et al. Bovine mesenteric vein graft (ProCol) in critical limb ischaemia with tissue loss and infection. Eur J Vasc Endovasc Surg. 2004; 27(3): p. 251-3.

89.   Katsimpoulas M, Morticelli L, Gontika I, Kouvaka A, Mallis P, Dipresa D, et al. Biocompatibility and Immunogenicity of Decellularized Allogeneic Aorta in the Orthotopic Rat Model. Tissue Eng Part A. 2019; 25(5-6): p. 399-415.

90.   Roy S, Silacci P, Stergiopulos N. Biomechanical proprieties of decellularized porcine common carotid arteries. American Journal of Physiology-Heart and Circulatory Physiology. 2005; 289(4): p. H1567-H1576.

91.   Geelhoed WJ, Moroni L, Rotmans JI. Utilizing the Foreign Body Response to Grow Tissue Engineered Blood Vessels in Vivo. J Cardiovasc Transl Res. 2017; 10(2): p. 167-179.

92.   Geelhoed WJ, van der Bogt KEA, Rothuizen TC, Damanik FFR, Hamming JF, Mota CD, et al. A novel method for engineering autologous non-thrombogenic in situ tissue-engineered blood vessels for arteriovenous grafting. Biomaterials. 2020; 229: p. 119577.

93.   Kato N, Yamagishi M, Kanda K, Miyazaki T, Maeda Y, Yamanami M, et al. First Successful Clinical Application of the In Vivo Tissue-Engineered Autologous Vascular Graft. Ann Thorac Surg. 2016; 102(4): p. 1387-90.

94.   L'Heureux N, Pâquet S, Labbé R, Germain L, Auger FA. A completely biological tissue-engineered human blood vessel. Faseb j. 1998; 12(1): p. 47-56.

95.   Maina RM, Barahona MJ, Finotti M, Lysyy T, Geibel P, D'Amico F, et al. Generating vascular conduits: from tissue engineering to three-dimensional bioprinting. Innovative surgical sciences. 2018; 3(3): p. 203-213.

96.   McAllister TN, Maruszewski M, Garrido SA, Wystrychowski W, Dusserre N, Marini A, et al. Effectiveness of haemodialysis access with an autologous tissue-engineered vascular graft: a multicentre cohort study. Lancet. 2009; 373(9673): p. 1440-6.

97.   Levit RD. Engineering Vessels as Good as New? JACC. Basic to translational science, 2018; 3, 119-121 DOI: 10.1016/j.jacbts.2017.11.008.

98. Kirkton RD, Santiago-Maysonet M, Lawson JH, Tente WE, Dahl SLM, Niklason LE, et al. Bioengineered human acellular vessels recellularize and evolve into living blood vessels after human implantation. Sci Transl Med. 2019; 11(485).

99. Lawson JH, Glickman MH, Ilzecki M, Jakimowicz T, Jaroszynski A, Peden EK, et al. Bioengineered human acellular vessels for dialysis access in patients with end-stage renal disease: two phase 2 single-arm trials. Lancet. 2016; 387(10032): p. 2026-34.

100. Chester JF. The causes of synthetic vascular graft failure. Annals of the College of Surgeons of Hong Kong. 2002; 6(4): p. 97-101.

101. van Andel CJ, Pistecky PV, Borst C. Mechanical properties of porcine and human arteries: implications for coronary anastomotic connectors. The Annals of Thoracic Surgery. 2003; 76(1): p. 58-64.

102. van Son JA, Smedts F, Vincent JG, van Lier HJ, Kubat K. Comparative anatomic studies of various arterial conduits for myocardial revascularization. J Thorac Cardiovasc Surg. 1990; 99(4): p. 703-7.

103. van der Lugt A, Gussenhoven EJ, The SH, van Essen J, Honkoop J, Blankensteijn JD, et al. Femorodistal venous bypass evaluated with intravascular ultrasound. Eur J Vasc Endovasc Surg. 1995; 9(4): p. 394-402.

104. Varty K, Porter K, Bell PR, London NJ. Vein morphology and bypass graft stenosis. Br J Surg. 1996; 83(10): p. 1375-9.

105. Stekelenburg M, Rutten MCM, Snoeckx LHEH, Baaijens FPT. Dynamic Straining Combined with Fibrin Gel Cell Seeding Improves Strength of Tissue-Engineered Small-Diameter Vascular Grafts. Tissue Engineering Part A. 2008; 15(5): p. 1081-1089.

106. Donovan DL, Schmidt SP, Townshend SP, Njus GO, Sharp WV. Material and structural characterization of human saphenous vein. Journal of Vascular Surgery. 1990; 12(5): p. 531-537.

107. L'Heureux N, Dusserre N, Konig G, Victor B, Keire P, Wight TN, et al. Human tissue-engineered blood vessels for adult arterial revascularization. Nature medicine. 2006; 12(3): p. 361-365.

108. Yu A, Dardik H, Wolodiger F, Raccuia J, Kapadia I, Sussman B, et al. Everted cervical vein for carotid patch angioplasty. Journal of Vascular Surgery. 1990; 12(5): p. 523-526.

109. Yin AL, Li J, Mo X, Luo R, Zhang X, Wang Y. Fabrication and characterization of coaxial electrospun multicomponent fibrous graft for vascular tissue engineering. Journal Of Controlled Release. 2017; 259: p. E8-E8.

110. Konig G, McAllister TN, Dusserre N, Garrido SA, Iyican C, Marini A, et al. Mechanical properties of completely autologous human tissue engineered blood vessels compared to human saphenous vein and mammary artery. Biomaterials. 2009; 30(8): p. 1542-1550.

111. Hasegawa M, Azuma T. Mechanical properties of synthetic arterial grafts. Journal of Biomechanics. 1979; 12(7): p. 509-517.

112. Tai NR, Giudiceandrea A, Salacinski HJ, Seifalian AM, Hamilton G. In vivo femoropopliteal arterial wall compliance in subjects with and without lower limb vascular disease. J Vasc Surg. 1999; 30(5): p. 936-45.

113. Claes E, Atienza JM, Guinea GV, Rojo FJ, Bernal JM, Revuelta JM, et al. Mechanical properties of human coronary arteries. in 2010 Annual International Conference of the IEEE Engineering in Medicine and Biology. 2010.

114. Holzapfel GA, Sommer G, Gasser CT, Regitnig P. Determination of layer-specific mechanical properties of human coronary arteries with nonatherosclerotic intimal thickening and related constitutive modeling. Am J Physiol Heart Circ Physiol. 2005; 289(5): p. H2048-58.

115. Yalcin Enis I, Gok Sadikoglu T. Design parameters for electrospun biodegradable vascular grafts. Journal of Industrial Textiles. 2016; 47(8): p. 2205-2227.

116. Pennel T, Bezuidenhout D, Koehne J, Davies NH, Zilla P. Transmural capillary ingrowth is essential for confluent vascular graft healing. Acta Biomaterialia. 2018; 65: p. 237-247.

117. Strobel HA, Qendro EI, Alsberg E, Rolle MW. Targeted Delivery of Bioactive Molecules for Vascular Intervention and Tissue Engineering. Frontiers in Pharmacology. 2018; 9(1329).

118. Doostmohammadi M, Forootanfar H, Ramakrishna S. Regenerative medicine and drug delivery: Progress via electrospun biomaterials. Materials Science and Engineering: C. 2020; 109: p. 110521.

119. Teo WE, Ramakrishna S. A review on electrospinning design and nanofibre assemblies. Nanotechnology. 2006; 17(14): p. R89-r106.

120. Anka FH, Balkus KJ. Novel Nanofiltration Hollow Fiber Membrane Produced via Electrospinning. Industrial & Engineering Chemistry Research. 2013; 52(9): p. 3473-3480.

121. Grasl C, Bergmeister H, Stoiber M, Schima H, Weigel G. Electrospun polyurethane vascular grafts: In vitro mechanical behavior and endothelial adhesion molecule expression. Journal of Biomedical Materials Research Part A. 2010; 93A(2): p. 716-723.

122. Spadaccio C, Chello M, Trombetta M, Rainer A, Toyoda Y, Genovese JA. Drug releasing systems in cardiovascular tissue engineering. Journal of cellular and molecular medicine. 2009; 13(3): p. 422-439.

123. Rathore A, Cleary M, Naito Y, Rocco K, Breuer C. Development of tissue engineered vascular grafts and application of nanomedicine. Wiley Interdiscip Rev Nanomed Nanobiotechnol. 2012; 4(3): p. 257-72.

124. Zamani M, Prabhakaran MP, Ramakrishna S. Advances in drug delivery via electrospun and electrosprayed nanomaterials. Int J Nanomedicine. 2013; 8: p. 2997-3017.

125. Tucker N, Stanger JJ, Staiger MP, Razzaq H, Hofman K. The History of the Science and Technology of Electrospinning from 1600 to 1995. Journal of Engineered Fibers and Fabrics. 2012; 7(2_suppl): p. 155892501200702S10.

126. Huang Z-M, Zhang YZ, Kotaki M, Ramakrishna S. A review on polymer nanofibers by electrospinning and their applications in nanocomposites. Composites Science and Technology. 2003; 63(15): p. 2223-2253.

127. Reneker DH, Yarin AL. Electrospinning jets and polymer nanofibers. Polymer. 2008; 49(10): p. 2387-2425.

128. Yoon J, Yang HS, Lee BS, Yu WR. Recent Progress in Coaxial Electrospinning: New Parameters, Various Structures, and Wide Applications. Advanced Materials. 2018; 30(42): p. n/a-n/a.

129. Quek SY, Hadi J, Tanambell H. Application of Electrospinning as Bioactive Delivery System. in Encyclopedia of Food Chemistry. L. Melton, F. Shahidi, and P. Varelis. Editors. 2019. Academic Press: Oxford. p. 145-149.

130. Basson N. Free volume of electrospun organic-inorganic copolymers. 2014.

131.   Baumgarten PK. Electrostatic spinning of acrylic microfibers. Journal of Colloid and Interface Science. 1971; 36(1): p. 71-79.

132.   Chong EJ, Phan TT, Lim IJ, Zhang YZ, Bay BH, Ramakrishna S, et al. Evaluation of electrospun PCL/gelatin nanofibrous scaffold for wound healing and layered dermal reconstitution. Acta Biomaterialia. 2007; 3(3): p. 321-330.

133.   Haghi AK, Akbari M. Trends in electrospinning of natural nanofibers. physica status solidi (a). 2007; 204(6): p. 1830-1834.

134.   Tan SH, Inai R, Kotaki M, Ramakrishna S. Systematic parameter study for ultra-fine fiber fabrication via electrospinning process. Polymer. 2005; 46(16): p. 6128-6134.

135.   Burger C, Hsiao BS, Chu B. Nanofibrous materials and their applications. Annual Review of Materials Research. 2006; 36(1): p. 333-368.

136.   Bhardwaj N, Kundu SC. Electrospinning: A fascinating fiber fabrication technique. Biotechnology Advances. 2010; 28(3): p. 325-347.

137.   Deitzel JM, Kleinmeyer J, Harris D, Beck Tan NC. The effect of processing variables on the morphology of electrospun nanofibers and textiles. Polymer. 2001; 42(1): p. 261-272.

138.   Liu H, Hsieh Y-L. Ultrafine fibrous cellulose membranes from electrospinning of cellulose acetate. Journal of Polymer Science Part B: Polymer Physics. 2002; 40(18): p. 2119-2129.

139.   Sukigara S, Gandhi M, Ayutsede J, Micklus M, Ko F. Regeneration of Bombyx mori silk by electrospinning—part 1: processing parameters and geometric properties. Polymer. 2003; 44(19): p. 5721-5727.

140.   McKee MG, Wilkes GL, Colby RH, Long TE. Correlations of Solution Rheology with Electrospun Fiber Formation of Linear and Branched Polyesters. Macromolecules. 2004; 37(5): p. 1760-1767.

141.   Ki CS, Baek DH, Gang KD, Lee KH, Um IC, Park YH. Characterization of gelatin nanofiber prepared from gelatin–formic acid solution. Polymer. 2005; 46(14): p. 5094-5102.

142.   Buchko CJ, Chen LC, Shen Y, Martin DC. Processing and microstructural characterization of porous biocompatible protein polymer thin films. Polymer. 1999; 40(26): p. 7397-7407.

143.   Fong H, Chun I, Reneker DH. Beaded nanofibers formed during electrospinning. Polymer. 1999; 40(16): p. 4585-4592.

144.   Deitzel JM, Kosik W, McKnight SH, Beck Tan NC, DeSimone JM, Crette S. Electrospinning of polymer nanofibers with specific surface chemistry. Polymer. 2002; 43(3): p. 1025-1029.

145.   Hohman MM, Shin M, Rutledge G, Brenner MP. Electrospinning and electrically forced jets. II. Applications. Physics of Fluids. 2001; 13(8): p. 2221-2236.

146.   Kim B, Park H, Lee S-H, Sigmund WM. Poly(acrylic acid) nanofibers by electrospinning. Materials Letters. 2005; 59(7): p. 829-832.

147.   Zuo W, Zhu M, Yang W, Yu H, Chen Y, Zhang Y. Experimental study on relationship between jet instability and formation of beaded fibers during electrospinning. Polymer Engineering & Science. 2005; 45(5): p. 704-709.

148.   Hayati I, Bailey AI, Tadros TF. Investigations into the mechanisms of electrohydrodynamic spraying of liquids: I. Effect of electric field and the environment on pendant drops and factors affecting the formation of stable jets and atomization. Journal of Colloid and Interface Science. 1987; 117(1): p. 205-221.

149. Zong X, Kim K, Fang D, Ran S, Hsiao BS, Chu B. Structure and process relationship of electrospun bioabsorbable nanofiber membranes. Polymer. 2002; 43(16): p. 4403-4412.

150. Ibrahim HM, Klingner A. A review on electrospun polymeric nanofibers: Production parameters and potential applications. Polymer Testing. 2020; 90: p. 106647.

151. Angammana CJ, Jayaram SH. Fundamentals of electrospinning and processing technologies. Particulate Science and Technology. 2016; 34(1): p. 72-82.

152. Haider A, Haider S, Kang I-K. A comprehensive review summarizing the effect of electrospinning parameters and potential applications of nanofibers in biomedical and biotechnology. Arabian Journal of Chemistry. 2018; 11(8): p. 1165-1188.

153. Lannutti J, Reneker D, Ma T, Tomasko D, Farson D. Electrospinning for tissue engineering scaffolds. Materials Science and Engineering: C. 2007; 27(3): p. 504-509.

154. Luo CJ, Stride E, Edirisinghe M. Mapping the Influence of Solubility and Dielectric Constant on Electrospinning Polycaprolactone Solutions. Macromolecules. 2012; 45(11): p. 4669-4680.

155. Sun Z, Deitzel JM, Knopf J, Chen X, Gillespie Jr JW. The effect of solvent dielectric properties on the collection of oriented electrospun fibers. Journal of Applied Polymer Science. 2012; 125(4): p. 2585-2594.

156. Agarwal S, Burgard M, Greiner A, Wendorff J. Electrospinning. 2016: De Gruyter.

157. Liu S, White KL, Reneker DH. Electrospinning Polymer Nanofibers With Controlled Diameters. IEEE Transactions on Industry Applications. 2019; 55(5): p. 5239-5243.

158. Yördem OS, Papila M, Menceloğlu YZ. Effects of electrospinning parameters on polyacrylonitrile nanofiber diameter: An investigation by response surface methodology. Materials & Design. 2008; 29(1): p. 34-44.

159. Lin T, Fang J. Fundamentals of Electrospinning & Electrospun Nanofibers. 2017. DEStech Publications.

160. Yuan X, Zhang Y, Dong C, Sheng J. Morphology of ultrafine polysulfone fibers prepared by electrospinning. Polymer International. 2004; 53(11): p. 1704-1710.

161. Wannatong L, Sirivat A, Supaphol P. Effects of solvents on electrospun polymeric fibers: preliminary study on polystyrene. Polymer International. 2004; 53(11): p. 1851-1859.

162. Xu CY, Inai R, Kotaki M, Ramakrishna S. Aligned biodegradable nanofibrous structure: a potential scaffold for blood vessel engineering. Biomaterials. 2004; 25(5): p. 877-86.

163. Ki CS, Kim JW, Hyun JH, Lee KH, Hattori M, Rah DK, et al. Electrospun three-dimensional silk fibroin nanofibrous scaffold. Journal of Applied Polymer Science. 2007; 106(6): p. 3922-3928.

164. Li D, Ouyang G, McCann JT, Xia Y. Collecting electrospun nanofibers with patterned electrodes. Nano Lett. 2005; 5(5): p. 913-6.

165. Jalili R, Morshed M, Ravandi SAH. Fundamental parameters affecting electrospinning of PAN nanofibers as uniaxially aligned fibers. Journal of Applied Polymer Science. 2006; 101(6): p. 4350-4357.

166. Zhang C, Yuan X, Wu L, Han Y, Sheng J. Study on morphology of electrospun poly(vinyl alcohol) mats. European Polymer Journal. 2005; 41(3): p. 423-432.

167. Pham QP, Sharma U, Mikos AG. Electrospun poly(epsilon-caprolactone) microfiber and multilayer nanofiber/microfiber scaffolds: characterization of scaffolds and measurement of cellular infiltration. Biomacromolecules. 2006; 7(10): p. 2796-805.

168.	Huan S, Liu G, Han G, Cheng W, Fu Z, Wu Q, et al. Effect of Experimental Parameters on Morphological, Mechanical and Hydrophobic Properties of Electrospun Polystyrene Fibers. Materials. 2015; 8(5).

169.	Khajavi R, Abbasipour M. 5 - Controlling nanofiber morphology by the electrospinning process. in Electrospun Nanofibers. M. Afshari. Editor. 2017. Woodhead Publishing. p. 109-123.

170.	Thompson CJ, Chase GG, Yarin AL, Reneker DH. Effects of parameters on nanofiber diameter determined from electrospinning model. Polymer. 2007; 48(23): p. 6913-6922.

171.	Mit-uppatham C, Nithitanakul M, Supaphol P. Ultrafine Electrospun Polyamide-6 Fibers: Effect of Solution Conditions on Morphology and Average Fiber Diameter. Macromolecular Chemistry and Physics. 2004; 205(17): p. 2327-2338.

172.	Ramos C, Lanno G-M, Laidmäe I, Meos A, Härmas R, Kogermann K. High humidity electrospinning of porous fibers for tuning the release of drug delivery systems. International Journal of Polymeric Materials and Polymeric Biomaterials. 2021; 70(12): p. 880-892.

173.	Park JY, Lee IH. Relative humidity effect on the preparation of porous electrospun polystyrene fibers. J Nanosci Nanotechnol. 2010; 10(5): p. 3473-7.

174.	Zhang D, Davoodi P, Li X, Liu Y, Wang W, Huang YYS. An empirical model to evaluate the effects of environmental humidity on the formation of wrinkled, creased and porous fibre morphology from electrospinning. Scientific Reports. 2020; 10(1): p. 18783.

175.	Nezarati RM, Eifert MB, Cosgriff-Hernandez E. Effects of humidity and solution viscosity on electrospun fiber morphology. Tissue engineering. Part C, Methods. 2013; 19(10): p. 810-819.

176.	Ghorani B, Tucker N. Fundamentals of electrospinning as a novel delivery vehicle for bioactive compounds in food nanotechnology. Food Hydrocolloids. 2015; 51: p. 227-240.

177.	Huang X, Jiao T, Liu Q, Zhang L, Zhou J, Li B, et al. Hierarchical electrospun nanofibers treated by solvent vapor annealing as air filtration mat for high-efficiency PM2.5 capture. Science China Materials. 2019; 62(3): p. 423-436.

178.	Casper CL, Stephens JS, Tassi NG, Chase DB, Rabolt JF. Controlling Surface Morphology of Electrospun Polystyrene Fibers: Effect of Humidity and Molecular Weight in the Electrospinning Process. Macromolecules. 2004; 37(2): p. 573-578.

179.	Huang L, Bui N-N, Manickam SS, McCutcheon JR. Controlling electrospun nanofiber morphology and mechanical properties using humidity. Journal of Polymer Science Part B: Polymer Physics. 2011; 49(24): p. 1734-1744.

180.	Sun Z, Zussman E, Yarin AL, Wendorff JH, Greiner A. Compound Core–Shell Polymer Nanofibers by Co-Electrospinning. Advanced Materials. 2003; 15(22): p. 1929-1932.

181.	Li D, Xia Y. Direct Fabrication of Composite and Ceramic Hollow Nanofibers by Electrospinning. Nano Letters. 2004; 4(5): p. 933-938.

182.	Wang D, Wang X, Zhang Z, Wang L, Li X, Xu Y, et al. Programmed Release of Multimodal, Cross-Linked Vascular Endothelial Growth Factor and Heparin Layers on Electrospun Polycaprolactone Vascular Grafts. ACS Applied Materials & Interfaces. 2019; 11(35): p. 32533-32542.

183.	Sahay R, Thavasi V, Ramakrishna S. Design Modifications in Electrospinning Setup for Advanced Applications. Journal of Nanomaterials. 2011; 2011: p. 317673.

184. Naeimirad M, Zadhoush A, Kotek R, Esmaeely Neisiany R, Nouri Khorasani S, Ramakrishna S. Recent advances in core/shell bicomponent fibers and nanofibers: A review. Journal of Applied Polymer Science. 2018; 135(21): p. 46265.

185. Jiang H, Wang L, Zhu K. Coaxial electrospinning for encapsulation and controlled release of fragile water-soluble bioactive agents. Journal of Controlled Release. 2014; 193: p. 296-303.

186. Duan N, Geng X, Ye L, Zhang A, Feng Z, Guo L, et al. A vascular tissue engineering scaffold with core–shell structured nano-fibers formed by coaxial electrospinning and its biocompatibility evaluation. Biomedical Materials. 2016; 11(3): p. 035007.

187. Abdullah MF, Nuge T, Andriyana A, Ang BC, Muhamad F. Core-Shell Fibers: Design, Roles, and Controllable Release Strategies in Tissue Engineering and Drug Delivery. Polymers. 2019; 11(12): p. 2008.

188. Ye K, Kuang H, You Z, Morsi Y, Mo X. Electrospun Nanofibers for Tissue Engineering with Drug Loading and Release. Pharmaceutics. 2019; 11(4).

189. Pant B, Park M, Park S-J. Drug Delivery Applications of Core-Sheath Nanofibers Prepared by Coaxial Electrospinning: A Review. Pharmaceutics. 2019; 11(7): p. 305.

190. Liao IC, Chen S, Liu JB, Leong KW. Sustained viral gene delivery through core-shell fibers. J Control Release. 2009; 139(1): p. 48-55.

191. Liao IC, Leong KW. Efficacy of engineered FVIII-producing skeletal muscle enhanced by growth factor-releasing co-axial electrospun fibers. Biomaterials. 2011; 32(6): p. 1669-1677.

192. Yu D-G, Branford-White C, Bligh SWA, White K, Chatterton NP, Zhu L-M. Improving Polymer Nanofiber Quality Using a Modified Co-axial Electrospinning Process. Macromolecular Rapid Communications. 2011; 32(9-10): p. 744-750.

193. Rahimi M, Mokhtari J. Fabrication of thermo-regulating hexadecane-polyurethane core-shell composite nanofibrous mat as advanced technical layer: Effect of coaxial nozzle geometry. Journal of Industrial Textiles. 2016; 47(6): p. 1134-1151.

194. Lee BS, Jeon SY, Park H, Lee G, Yang HS, Yu WR. New electrospinning nozzle to reduce jet instability and its application to manufacture of multi-layered nanofibers. Sci Rep. 2014; 4: p. 6758.

195. Tong X, Bin-Jie X. Preparation and characterization of coaxial electrospun polysulfone amide/polyurethane. Journal of Industrial Textiles. 2016; 46(8): p. 1581-1597.

196. Wu H, Bian F, Gong RH, Zeng Y. Effects of Electric Field and Polymer Structure on the Formation of Helical Nanofibers via Coelectrospinning. Industrial & Engineering Chemistry Research. 2015; 54(39): p. 9585-9590.

197. Kaerkitcha N, Chuangchote S, Hachiya K, Sagawa T. Influence of the viscosity ratio of polyacrylonitrile/poly(methyl methacrylate) solutions on core–shell fibers prepared by coaxial electrospinning. Polymer Journal. 2017; 49(6): p. 497-502.

198. Tiwari SK, Venkatraman SS. Importance of viscosity parameters in electrospinning: Of monolithic and core–shell fibers. Materials Science and Engineering: C. 2012; 32(5): p. 1037-1042.

199. Yarin AL. Coaxial electrospinning and emulsion electrospinning of core–shell fibers. Polymers for Advanced Technologies. 2011; 22(3): p. 310-317.

200. Yang L, Korom S, Welti M, Hoerstrup SP, Zünd G, Jung FJ, et al. Tissue engineered cartilage generated from human trachea using DegraPol scaffold. Eur J Cardiothorac Surg. 2003; 24(2): p. 201-7.

201.   Saad B, Ciardelli G, Matter S, Welti M, Uhlschmid GK, Neuenschwander P, et al. Degradable and highly porous polyesterurethane foam as biomaterial: effects and phagocytosis of degradation products in osteoblasts. J Biomed Mater Res. 1998; 39(4): p. 594-602.

202.   Kucinska-Lipka J, Gubanska I, Janik H, Sienkiewicz M. Fabrication of polyurethane and polyurethane based composite fibres by the electrospinning technique for soft tissue engineering of cardiovascular system. Materials Science and Engineering: C. 2015; 46: p. 166-176.

203.   Borkenhagen M, Stoll RC, Neuenschwander P, Suter UW, Aebischer P. In vivo performance of a new biodegradable polyester urethane system used as a nerve guidance channel. Biomaterials. 1998; 19(23): p. 2155-2165.

204.   Lendlein A, Colussi M, Neuenschwander P, Suter UW. Hydrolytic Degradation of Phas... Segregated Multiblock Copoly(ester urethane)s Containing Weak Links. Macromolecular Chemistry and Physics. 2001; 202: p. 2702-2711.

205.   Lendlein A, Neuenschwander P, Suter UW. Tissue-compatible multiblock copolymers for medical applications, controllable in degradation rate and mechanical properties. Macromolecular Chemistry and Physics. 1998; 199(12): p. 2785-2796.

206.   Hülk VM. Electrospun Tissue Engineered Vascular Grafts. in Cardiovascular Research Unit. 2019. University of Cape Town: Cape Town.

207.   Evrova O, Houska J, Welti M, Bonavoglia E, Calcagni M, Giovanoli P, et al. Bioactive, Elastic, and Biodegradable Emulsion Electrospun DegraPol Tube Delivering PDGF-BB for Tendon Rupture Repair. Macromolecular Bioscience. 2016; 16(7): p. 1048-1063.

208.   Henry JA, Simonet M, Pandit A, Neuenschwander P. Characterization of a slowly degrading biodegradable polyester-urethane for tissue engineering scaffolds. J Biomed Mater Res A. 2007; 82(3): p. 669-79.

209.   Van den Bergh WJW. Drug eluting electrospun scaffolds for tissue regeneration. 2018. University of Cape Town.

210.   Krynauw H, Bruchmüller L, Bezuidenhout D, Zilla P, Franz T. Degradation-induced changes of mechanical properties of an electro-spun polyester-urethane scaffold for soft tissue regeneration. Journal of Biomedical Materials Research Part B: Applied Biomaterials. 2011; 99B(2): p. 359-368.

211.   Milleret V, Hefti T, Hall H, Vogel V, Eberli D. Influence of the fiber diameter and surface roughness of electrospun vascular grafts on blood activation. Acta Biomaterialia. 2012; 8(12): p. 4349-4356.

212.   Limbert G, Omar R, Krynauw H, Bezuidenhout D, Franz T. The anisotropic mechanical behaviour of electro-spun biodegradable polymer scaffolds: Experimental characterisation and constitutive formulation. Journal of the Mechanical Behavior of Biomedical Materials. 2016; 53: p. 21-39.

213.   Brizzola S, de Eguileor M, Brevini T, Grimaldi A, Congiu T, Neuenschwander P, et al. Morphologic features of biocompatibility and neoangiogenesis onto a biodegradable tracheal prosthesis in an animal model. Interact Cardiovasc Thorac Surg. 2009; 8(6): p. 610-4.

214.   Horst M, Milleret V, Noetzli S, Gobet R, Sulser T, Eberli D. Polyesterurethane and acellular matrix based hybrid biomaterial for bladder engineering. J Biomed Mater Res B Appl Biomater. 2017; 105(3): p. 658-667.

215.   Buschmann J, Meier-Bürgisser G, Bonavoglia E, Neuenschwander P, Milleret V, Giovanoli P, et al. Cellular response of healing tissue to DegraPol tube implantation in

rabbit Achilles tendon rupture repair: an in vivo histomorphometric study. J Tissue Eng Regen Med. 2013; 7(5): p. 413-20.

216. Meier Bürgisser G, Calcagni M, Müller A, Bonavoglia E, Fessel G, Snedeker JG, et al. Prevention of peritendinous adhesions using an electrospun DegraPol polymer tube: a histological, ultrasonographic, and biomechanical study in rabbits. BioMed research international. 2014; 2014: p. 656240-656240.

217. Buschmann J, Calcagni M, Bürgisser GM, Bonavoglia E, Neuenschwander P, Milleret V, et al. Synthesis, characterization and histomorphometric analysis of cellular response to a new elastic DegraPol® polymer for rabbit Achilles tendon rupture repair. J Tissue Eng Regen Med. 2015; 9(5): p. 584-94.

218. Evrova O, Bürgisser GM, Ebnöther C, Adathala A, Calcagni M, Bachmann E, et al. Elastic and surgeon friendly electrospun tubes delivering PDGF-BB positively impact tendon rupture healing in a rabbit Achilles tendon model. Biomaterials. 2020; 232: p. 119722.

219. Evrova O, Buschmann J. In vitro and in vivo effects of PDGF-BB delivery strategies on tendon healing: a review. Eur Cell Mater. 2017; 34: p. 15-39.

220. Milleret V, Bittermann AG, Mayer D, Hall H. Analysis of Effective Interconnectivity of DegraPol-foams Designed for Negative Pressure Wound Therapy. Materials. 2009; 2(1): p. 292-306.

221. Simonet M, Schneider OD, Neuenschwander P, Stark WJ. Ultraporous 3D polymer meshes by low-temperature electrospinning: Use of ice crystals as a removable void template. Polymer Engineering & Science. 2007; 47(12): p. 2020-2026.

222. Milleret V, Simona B, Neuenschwander P, Hall H. Tuning electrospinning parameters for production of 3D-fiber-fleeces with increased porosity for soft tissue engineering applications. Eur Cell Mater. 2011; 21: p. 286-303.

223. Absar S, Khan M, Edwards K, Neumann J. Investigation of synthesis and processing of cellulose, cellulose acetate and poly(ethylene oxide) nanofibers incorporating anti-cancer/tumor drug cis-diammineplatinum (II) dichloride using electrospinning techniques. Journal of Polymer Engineering. 2015; 35(9): p. 867-878.

224. Deb S. 2 - Degradable polymers and polymer composites for tissue engineering. in Cellular Response to Biomaterials. L. Di Silvio. Editor. 2009. Woodhead Publishing. p. 28-60.

225. Dhawan S, Dhawan K, Varma M, Sinha V. Applications of Poly(ethylene oxide) in Drug Delivery Systems Part II. Pharm Technol. 2005; 29.

226. Ma L, Deng L, Chen J. Applications of poly(ethylene oxide) in controlled release tablet systems: a review. Drug Dev Ind Pharm. 2014; 40(7): p. 845-51.

227. Zhang Y, Sun T, Jiang C. Biomacromolecules as carriers in drug delivery and tissue engineering. Acta Pharm Sin B. 2018; 8(1): p. 34-50.

228. Schneider HE, Steuber JG, Du W, Mortazavi M, Bullock DW. Polyethylene Oxide Nanofiber Production by Electrospinning. Journal of the Arkansas Academy of Science. 2016; 70.

229. Son W-K, Youk J, Lee T, Park WH. The effects of solution properties and polyelectrolyte on electrospinning of ultrafine poly(ethylene oxide) fibers. Polymer. 2004; 45: p. 2959-2966.

230. Jiang H, Hu Y, Zhao P, Li Y, Zhu K. Modulation of protein release from biodegradable core-shell structured fibers prepared by coaxial electrospinning. J Biomed Mater Res B Appl Biomater. 2006; 79(1): p. 50-7.

231. Nguyen TTT, Lee JG, Park JS. Fabrication and characterization of coaxial electrospun polyethylene glycol/polyvinylidene fluoride (Core/Sheath) composite non-woven mats. Macromolecular Research. 2011; 19(4): p. 370-378.

232. Saraf A, Lozier G, Haesslein A, Kasper FK, Raphael RM, Baggett LS, et al. Fabrication of Nonwoven Coaxial Fiber Meshes by Electrospinning. Tissue Engineering Part C: Methods. 2009; 15(3): p. 333-344.

233. Srouji S, Ben-David D, Lotan R, Livne E, Avrahami R, Zussman E. Slow-Release Human Recombinant Bone Morphogenetic Protein-2 Embedded Within Electrospun Scaffolds for Regeneration of Bone Defect: In Vitro and In Vivo Evaluation. Tissue Engineering Part A. 2010; 17(3-4): p. 269-277.

234. Wu Y-H, Yu D-G, Li H-P, Wu X-Y, Li X-Y. Medicated structural PVP/PEG composites fabricated using coaxial electrospinning. e-Polymers. 2017; 17(1): p. 39-44.

235. Zhang YZ, Wang X, Feng Y, Li J, Lim CT, Ramakrishna S. Coaxial Electrospinning of (Fluorescein Isothiocyanate-Conjugated Bovine Serum Albumin)-Encapsulated Poly(ε-caprolactone) Nanofibers for Sustained Release. Biomacromolecules. 2006; 7(4): p. 1049-1057.

236. Esmaeili A, Haseli M. Electrospinning of thermoplastic carboxymethyl cellulose/poly(ethylene oxide) nanofibers for use in drug-release systems. Mater Sci Eng C Mater Biol Appl. 2017; 77: p. 1117-1127.

237. Jiang H, Hu Y, Li Y, Zhao P, Zhu K, Chen W. A facile technique to prepare biodegradable coaxial electrospun nanofibers for controlled release of bioactive agents. Journal of Controlled Release. 2005; 108(2): p. 237-243.

238. Linhardt RJ, Murugesan S, Xie J. Immobilization of Heparin: Approaches and Applications. Current Topics in Medicinal Chemistry. 2008; 8(2): p. 80-100.

239. Aslani S, Kabiri M, HosseinZadeh S, Hanaee-Ahvaz H, Taherzadeh ES, Soleimani M. The applications of heparin in vascular tissue engineering. Microvascular Research. 2020; 131: p. 104027.

240. Brenner GM, Stevens CW. Antithrombotic and Thrombolytic Drugs. in Brenner and Stevens' Pharmacology. 2018. Elsevier: Philadelphia, PA. p. 171-184.

241. Trevor AJ, Katzung BG, Kruidering-Hall MM, Masters SB. Chapter 34. Drugs Used in Coagulation Disorders. in Katzung & Trevor's Pharmacology: Examination & Board Review, 10e. 2013. The McGraw-Hill Companies: New York, NY.

242. Jia X, Zhao C, Li P, Zhang H, Huang Y, Li H, et al. Sustained Release of VEGF by Coaxial Electrospun Dextran/PLGA Fibrous Membranes in Vascular Tissue Engineering. Journal of Biomaterials Science, Polymer Edition. 2011; 22(13): p. 1811-1827.

243. D'Amore PA. Heparin-endothelial cell interactions. Haemostasis. 1990; 20 Suppl 1: p. 159-65.

244. Oberhoff M, Novak S, Herdeg C, Baumbach A, Kranzhöfer A, Bohnet A, et al. Local and systemic delivery of low molecular weight heparin stimulates the reendothelialization after balloon angioplasty. Cardiovascular research. 1998; 38: p. 751-62.

245. Rosenbaum J, Tobelem G, Molho P, Bârzu T, Caen JP. Modulation of endothelial cells growth induced by heparin. Cell Biology International Reports. 1986; 10(6): p. 437-446.

246. Khorana AA, Sahni A, Altland OD, Francis CW. Heparin Inhibition of Endothelial Cell Proliferation and Organization Is Dependent on Molecular Weight. Arteriosclerosis, Thrombosis, and Vascular Biology. 2003; 23(11): p. 2110-2115.

247. Zhang C, Feng F, Zhang H. Emulsion electrospinning: Fundamentals, food applications and prospects. Trends in Food Science & Technology. 2018; 80: p. 175-186.

248. Chaparro F. Bioactive Incorporation into Spun Scaffolds. Electrospinning & Electrospraying Equipment [cited 2021 2 April]; Available from: https://www.nanoscience.com/applications/medical/bioactive-incorporation-spun-scaffolds/.

249. Chen X, Wang J, An Q, Li D, Liu P, Zhu W, et al. Electrospun poly(l-lactic acid-co-ε-caprolactone) fibers loaded with heparin and vascular endothelial growth factor to improve blood compatibility and endothelial progenitor cell proliferation. Colloids and Surfaces B: Biointerfaces. 2015; 128: p. 106-114.

250. Antonova LV, Mironov AV, Yuzhalin AE, Krivkina EO, Shabaev AR, Rezvova MA, et al. A Brief Report on an Implantation of Small-Caliber Biodegradable Vascular Grafts in a Carotid Artery of the Sheep. Pharmaceuticals. 2020; 13(5).

251. Matsuzaki Y, Miyamoto S, Miyachi H, Iwaki R, Shoji T, Blum K, et al. Improvement of a Novel Small-diameter Tissue-engineered Arterial Graft With Heparin Conjugation. The Annals of Thoracic Surgery. 2021; 111(4): p. 1234-1241.

252. Cremers HFM, Kwon G, Bae YH, Kim SW, Verrijk R, Noteborn HPJM, et al. Preparation and characterization of albumin-heparin microspheres. Biomaterials. 1994; 15(1): p. 38-48.

253. Hoshi RA, Van Lith R, Jen MC, Allen JB, Lapidos KA, Ameer G. The blood and vascular cell compatibility of heparin-modified ePTFE vascular grafts. Biomaterials. 2013; 34(1): p. 30-41.

254. Chen F, Huang P, Mo X. Electrospinning of Heparin Encapsulated P(LLA-CL) Core/Shell Nanofibers. Nano Biomedicine and Engineering. 2010; 2(1).

255. Su Y, Li X, Liu Y, Su Q, Qiang MLW, Mo X. Encapsulation and Controlled Release of Heparin from Electrospun Poly(L-Lactide-co-ε-Caprolactone) Nanofibers. Journal of Biomaterials Science, Polymer Edition. 2011; 22(1-3): p. 165-177.

256. Li X, Su Y, Chen R, He C, Wang H, Mo X. Fabrication and properties of core-shell structure P(LLA-CL) nanofibers by coaxial electrospinning. Journal of Applied Polymer Science. 2009; 111(3): p. 1564-1570.

257. Yin A, Zhang K, McClure MJ, Huang C, Wu J, Fang J, et al. Electrospinning collagen/chitosan/poly(L-lactic acid-co-ϵ-caprolactone) to form a vascular graft: Mechanical and biological characterization. Journal of Biomedical Materials Research Part A. 2013; 101A(5): p. 1292-1301.

258. Yin A, Luo R, Li J, Mo X, Wang Y, Zhang X. Coaxial electrospinning multicomponent functional controlled-release vascular graft: Optimization of graft properties. Colloids and Surfaces B: Biointerfaces. 2017; 152: p. 432-439.

259. Huang C, Wang S, Qiu L, Ke Q, Zhai W, Mo X. Heparin Loading and Pre-endothelialization in Enhancing the Patency Rate of Electrospun Small-Diameter Vascular Grafts in a Canine Model. ACS Applied Materials & Interfaces. 2013; 5(6): p. 2220-2226.

260. Wang S, Mo X, Jiang B, Gao C, Wang H, Zhuang Y, et al. Fabrication of small-diameter vascular scaffolds by heparin-bonded P(LLA-CL) composite nanofibers to improve graft patency. International Journal of Nanomedicine. 2013; 8(1): p. 2131-2139.

261. Kuang H, Wang Y, Hu J, Wang C, Lu S, Mo X. A Method for Preparation of an Internal Layer of Artificial Vascular Graft Co-Modified with Salvianolic Acid B and Heparin. ACS Applied Materials & Interfaces. 2018; 10(23): p. 19365-19372.

262. Feng W, Liu P, Yin H, Gu Z, Wu Y, Zhu W, et al. Heparin and rosuvastatin calcium-loaded poly(l-lactide-co-caprolactone) nanofiber-covered stent-grafts for aneurysm treatment. New Journal of Chemistry. 2017; 41(17): p. 9014-9023.

263. Hu Y-T, Pan X-D, Zheng J, Ma W-G, Sun L-Z. In vitro and in vivo evaluation of a small-caliber coaxial electrospun vascular graft loaded with heparin and VEGF. International Journal of Surgery. 2017; 44: p. 244-249.

264. Ye Y-J, Zhou Y-Q, Jing Z-Y, Liu Y-Y, Yin D-C. Electrospun Heparin-Loaded Core–Shell Nanofiber Sutures for Achilles Tendon Regeneration In Vivo. Macromolecular Bioscience. 2018; 18(7): p. 1800041.

265. Hou L, Udangawa WMRN, Pochiraju A, Dong W, Zheng Y, Linhardt RJ, et al. Synthesis of Heparin-Immobilized, Magnetically Addressable Cellulose Nanofibers for Biomedical Applications. ACS Biomaterials Science & Engineering. 2016; 2(11): p. 1905-1913.

266. Assmann U, Szentivanyi A, Stark Y, Scheper T, Berski S, Dräger G, et al. Fiber scaffolds of polysialic acid via electrospinning for peripheral nerve regeneration. J Mater Sci Mater Med. 2010; 21(7): p. 2115-24.

267. Fu Y, Kao WJ. Drug release kinetics and transport mechanisms of non-degradable and degradable polymeric delivery systems. Expert opinion on drug delivery. 2010; 7(4): p. 429-444.

268. Innocente F, Mandracchia D, Pektok E, Nottelet B, Tille JC, de Valence S, et al. Paclitaxel-eluting biodegradable synthetic vascular prostheses: a step towards reduction of neointima formation? Circulation. 2009; 120(11 Suppl): p. S37-45.

269. Luong-Van E, Grøndahl L, Chua KN, Leong KW, Nurcombe V, Cool SM. Controlled release of heparin from poly(ε-caprolactone) electrospun fibers. Biomaterials. 2006; 27(9): p. 2042-2050.

270. Luu YK, Kim K, Hsiao BS, Chu B, Hadjiargyrou M. Development of a nanostructured DNA delivery scaffold via electrospinning of PLGA and PLA-PEG block copolymers. J Control Release. 2003; 89(2): p. 341-53.

271. Sahoo S, Ang LT, Goh JC, Toh SL. Growth factor delivery through electrospun nanofibers in scaffolds for tissue engineering applications. J Biomed Mater Res A. 2010; 93(4): p. 1539-50.

272. Zeng J, Aigner A, Czubayko F, Kissel T, Wendorff JH, Greiner A. Poly(vinyl alcohol) nanofibers by electrospinning as a protein delivery system and the retardation of enzyme release by additional polymer coatings. Biomacromolecules. 2005; 6(3): p. 1484-8.

273. Costa P, Sousa Lobo JM. Modeling and comparison of dissolution profiles. Eur J Pharm Sci. 2001; 13(2): p. 123-33.

274. Ei-Arini SK, Leuenberger H. Modelling of drug release from polymer matrices: Effect of drug loading. International Journal of Pharmaceutics. 1995; 121: p. 141-148.

275. Szentivanyi A, Chakradeo T, Zernetsch H, Glasmacher B. Electrospun cellular microenvironments: Understanding controlled release and scaffold structure. Adv Drug Deliv Rev. 2011; 63(4-5): p. 209-20.

276. Korsmeyer RW, Gurny R, Doelker E, Buri P, Peppas NA. Mechanisms of solute release from porous hydrophilic polymers. International Journal of Pharmaceutics. 1983; 15(1): p. 25-35.

277.   Sell SA, McClure MJ, Garg K, Wolfe PS, Bowlin GL. Electrospinning of collagen/biopolymers for regenerative medicine and cardiovascular tissue engineering. Adv Drug Deliv Rev. 2009; 61(12): p. 1007-19.

278.   Dash S, Murthy PN, Nath L, Chowdhury P. Kinetic modeling on drug release from controlled drug delivery systems. Acta Pol Pharm. 2010; 67(3): p. 217-23.

279.   Kwon IK, Matsuda T. Co-Electrospun Nanofiber Fabrics of Poly(l-lactide-co-ε-caprolactone) with Type I Collagen or Heparin. Biomacromolecules. 2005; 6(4): p. 2096-2105.

280.   Liu C, Zhu C, Li J, Zhou P, Chen M, Yang H, et al. The effect of the fibre orientation of electrospun scaffolds on the matrix production of rabbit annulus fibrosus-derived stem cells. Bone Research. 2015; 3(1): p. 15012.

281.   Stalder AF, Melchior T, Müller M, Sage D, Blu T, Unser M. Low-bond axisymmetric drop shape analysis for surface tension and contact angle measurements of sessile drops. Colloids and Surfaces A: Physicochemical and Engineering Aspects. 2010; 364(1): p. 72-81.

282.   Tai NR, Salacinski HJ, Edwards A, Hamilton G, Seifalian AM. Compliance properties of conduits used in vascular reconstruction. Br J Surg. 2000; 87(11): p. 1516-24.

283.   Jose AD, Collison D. The normal range and determinants of the intrinsic heart rate in man. Cardiovasc Res. 1970; 4(2): p. 160-7.

284.   Weissler AM, Harris WS, Schoenfeld CD. Systolic time intervals in heart failure in man. Circulation. 1968; 37(2): p. 149-59.

285.   International Organization for Standardization. ISO 7198:2016. in Cardiovascular implants and extracorporeal systems — Vascular prostheses — Tubular vascular grafts and vascular patches. 2016.

286.   Walsh M, Fritz S, Hake D, Son M, Greve S, Jbara M, et al. Targeted Thromboelastographic (TEG) Blood Component and Pharmacologic Hemostatic Therapy in Traumatic and Acquired Coagulopathy. Current drug targets. 2016; 17(8): p. 954-970.

287.   TEG® 5000 Hemostasis Analyzer System. H. S.A. Editor. 2010: Switzerland.

288.   Dias J, Haney E, Mathew B, Lopez-Espina C, Orr A, Popovsky M. New-Generation Thromboelastography. Comprehensive Evaluation of Citrated and Heparinized Blood Sample Storage Effect on Clot-Forming Variables. Archives of pathology & laboratory medicine. 2017; 141.

289.   Balguid A, Mol A, van Marion MH, Bank RA, Bouten CV, Baaijens FP. Tailoring fiber diameter in electrospun poly(epsilon-caprolactone) scaffolds for optimal cellular infiltration in cardiovascular tissue engineering. Tissue Eng Part A. 2009; 15(2): p. 437-44.

290.   Miller KS, Khosravi R, Breuer CK, Humphrey JD. A hypothesis-driven parametric study of effects of polymeric scaffold properties on tissue engineered neovessel formation. Acta biomaterialia. 2015; 11: p. 283-294.

291.   Sanders JE, Cassisi DV, Neumann T, Golledge SL, Zachariah SG, Ratner BD, et al. Relative influence of polymer fiber diameter and surface charge on fibrous capsule thickness and vessel density for single-fiber implants. J Biomed Mater Res A. 2003; 65(4): p. 462-7.

292.   Sanders JE, Lamont SE, Mitchell SB, Malcolm SG. Small fiber diameter fibro-porous meshes: Tissue response sensitivity to fiber spacing. Journal of Biomedical Materials Research Part A. 2005; 72A(3): p. 335-342.

293. Sanders JE, Stiles CE, Hayes CL. Tissue response to single-polymer fibers of varying diameters: evaluation of fibrous encapsulation and macrophage density. J Biomed Mater Res. 2000; 52(1): p. 231-7.

294. Nelson MT, Keith JP, Li B-B, Stocum DL, Li J. Electrospun composite polycaprolactone scaffolds for optimized tissue regeneration. Proceedings of the Institution of Mechanical Engineers, Part N: Journal of Nanoengineering and Nanosystems. 2012; 226(3): p. 111-121.

295. Soliman S, Sant S, Nichol JW, Khabiry M, Traversa E, Khademhosseini A. Controlling the porosity of fibrous scaffolds by modulating the fiber diameter and packing density. Journal of Biomedical Materials Research Part A. 2011; 96A(3): p. 566-574.

296. de Valence S, Tille JC, Giliberto JP, Mrowczynski W, Gurny R, Walpoth BH, et al. Advantages of bilayered vascular grafts for surgical applicability and tissue regeneration. Acta Biomaterialia. 2012; 8(11): p. 3914-3920.

297. Voorneveld J, Oosthuysen A, Franz T, Zilla P, Bezuidenhout D. Dual electrospinning with sacrificial fibers for engineered porosity and enhancement of tissue ingrowth. Journal of Biomedical Materials Research Part B: Applied Biomaterials. 2017; 105(6): p. 1559-1572.

298. Campbell CD, Goldfarb D, Roe R. A small arterial substitute: expanded microporous polytetrafluoroethylene: patency versus porosity. Ann Surg. 1975; 182(2): p. 138-43.

299. Contreras MA, Quist WC, Logerfo FW. Effect of porosity on small-diameter vascular graft healing. Microsurgery. 2000; 20(1): p. 15-21.

300. Edwards WS. The effect of porosity in solid plastic artery grafts. Surg Forum. 1957; 8: p. 446-50.

301. FRY WJ, DeWEESE MS, KRAFT RO, ERNST CB. Importance of Porosity in Arterial Prostheses. Archives of Surgery. 1964; 88(5): p. 836-842.

302. Harrison JH, Davalos PA. Influence of porosity on synthetic grafts. Fate in animals. Arch Surg. 1961; 82: p. 8-13.

303. Lee JH, Khang G, Lee HB. Blood Leak-Proof Porous Vascular Grafts. in Biomaterials Engineering and Devices: Human Applications: Volume 1 Fundamentals and Vascular and Carrier Applications. D.L. Wise, et al. Editors. 2000. Humana Press: Totowa, NJ. p. 161-179.

304. Wesolowski SA, Fries CC, Karlson KE, Bakey MD, Sawyer PN. Porosity: primary determinant of ultimate fate ot synthetic vascular grafts. Surgery. 1961; 50(1): p. 91-96.

305. Zhao J, Farhatnia Y, Kalaskar DM, Zhang Y, Bulter PE, Seifalian AM. The influence of porosity on the hemocompatibility of polyhedral oligomeric silsesquioxane poly (caprolactone-urea) urethane. Int J Biochem Cell Biol. 2015; 68: p. 176-86.

306. Lam KH, Schakenraad JM, Groen H, Esselbrugge H, Dijkstra PJ, Feijen J, et al. The influence of surface morphology and wettability on the inflammatory response against poly(L-lactic acid): a semi-quantitative study with monoclonal antibodies. J Biomed Mater Res. 1995; 29(8): p. 929-42.

307. Law K-Y. Definitions for Hydrophilicity, Hydrophobicity, and Superhydrophobicity: Getting the Basics Right. The Journal of Physical Chemistry Letters. 2014; 5(4): p. 686-688.

308. Bergmeister H, Schreiber C, Grasl C, Walter I, Plasenzotti R, Stoiber M, et al. Healing characteristics of electrospun polyurethane grafts with various porosities. Acta Biomaterialia. 2013; 9(4): p. 6032-6040.

309. Camasão DB, Mantovani D. The mechanical characterization of blood vessels and their substitutes in the continuous quest for physiological-relevant performances. A critical review. Materials Today Bio. 2021; 10: p. 100106.

310. Luo X, Qiu D, He B, Wang L, Luo J. Biodegradable Heparin-Loaded Microspheres: Carrier Molecular Composition and Microsphere Structure. Macromolecular Bioscience. 2006; 6(5): p. 373-381.

311. Shoichet MS. Polymer Scaffolds for Biomaterials Applications. Macromolecules. 2010; 43(2): p. 581-591.

312. Awad NK, Niu H, Ali U, Morsi YS, Lin T. Electrospun Fibrous Scaffolds for Small-Diameter Blood Vessels: A Review. Membranes. 2018; 8(1): p. 15.

313. Yin A, Li J, Bowlin GL, Li D, Rodriguez IA, Wang J, et al. Fabrication of cell penetration enhanced poly (l-lactic acid-co-ε-caprolactone)/silk vascular scaffolds utilizing air-impedance electrospinning. Colloids and Surfaces B: Biointerfaces. 2014; 120: p. 47-54.

314. Pennel T, Fercana G, Bezuidenhout D, Simionescu A, Chuang T-H, Zilla P, et al. The performance of cross-linked acellular arterial scaffolds as vascular grafts; pre-clinical testing in direct and isolation loop circulatory models. Biomaterials. 2014; 35(24): p. 6311-6322.

315. Sigma-Aldrich. Heparin sodium salt from porcine intestinal mucosa (H3393). Sigma-Aldrich. Editor. 2015.

316. Santa Cruz Animal Health. Heparin sodium salt (CAS 9041-08-1) 2014 [cited 2021 10 February]; Available from: https://www.scbt.com/p/heparin-sodium-salt-9041-08-1.

317. Colomer I, Chamberlain AER, Haughey MB, Donohoe TJ. Hexafluoroisopropanol as a highly versatile solvent. Nature Reviews Chemistry. 2017; 1(11): p. 0088.

318. Smallwood IM. Chloroform. in Handbook of Organic Solvent Properties. I.M. Smallwood. Editor. 1996. Butterworth-Heinemann: Oxford. p. 141-143.

319. Smallwood IM. 1,2-Dichlorethane. in Handbook of Organic Solvent Properties. I.M. Smallwood. Editor. 1996. Butterworth-Heinemann: Oxford. p. 149-151.

320. Smallwood IM. Water. in Handbook of Organic Solvent Properties. I.M. Smallwood. Editor. 1996. Butterworth-Heinemann: Oxford. p. 301-303.

321. Smallwood IM. Ethanol. in Handbook of Organic Solvent Properties. I.M. Smallwood. Editor. 1996. Butterworth-Heinemann: Oxford. p. 65-67.

322. Smallwood IM. Methylene chloride. in Handbook of Organic Solvent Properties. I.M. Smallwood. Editor. 1996. Butterworth-Heinemann: Oxford. p. 137-139.

323. Washington Uo. Dielectric Constant of Common solvents. [cited 2021 10 June]; Available from: https://depts.washington.edu/eooptic/linkfiles/dielectric_chart%5B1%5D.pdf.

Appendix A   Solvent properties

Identified solvents for DP30 [209]:

- 1,1,1,3,3,3-Hexafluoro-2-propanol (HFIP)
- Chloroform (CHCl₃)
- Dichloromethane (DCM)
- 1,2-Dichloroethane (DCE)
- Trifluoro acedic acid (TFA)
- Trifluoro ethanol (TFE)

Identified solvents for Heparin sodium:

- Water (50 mg/ml [315])
- Ethanol (< 1 mg/ml [316])

Table 17: Solvent properties of possible solvents for DP30 and HepNa⁺. Compiled from data from [317-323].

Solvent	Dielectric constant ε	Surface tension, γ @20°C (dyn/cm)	Electrical conductivity, σ_e (ohm^{-1} m^{-1})	Vapour pressure, V_p @21°C (mmHg)	Polarity, P (water = 100)	Absolute viscosity (@25°C cP)	Boiling point, T_b (°C)	Specific gravity, SG
(CHCl3)	4.8	27.2	1.00E-10	169	25.9	0.57	61	1.48
(TFE)*	8.6	16.5	N/a	N/a	N/a	0.9	74	1.38
(DCM)	9.1	28.1	4.00E-11	376	30.9	0.44	40	1.33
(DCE)	10.5	32.2	4.00E-11	71	32.7	0.9	84	1.25
(HFIP)*	17.8	16.1	N/a	158	N/a	1.02	59	1.596
(TFA)*	42.1	22	N/a	110	N/a	0.74	72.4	1.531
Water	80.1	72.8	5.00E-01	19	100	0.89	100	1
Ethanol	22.4	22.3	1.00E-09	45.7	65.4	1.08	78	0.79
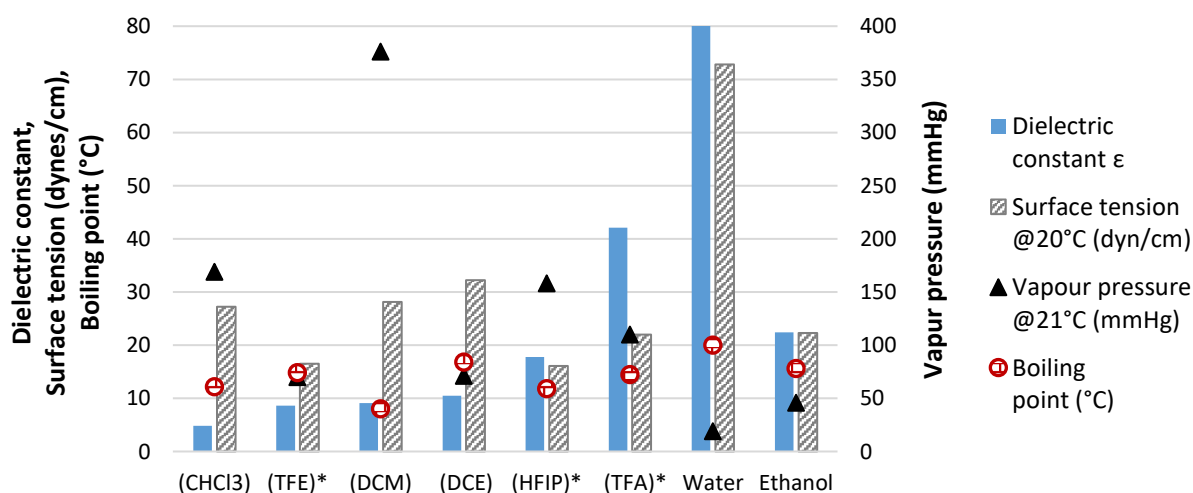
Figure 61: Plotted properties for possible DP30 and HepNa⁺ solvents [317-323].

Appendix B   CAD drawings
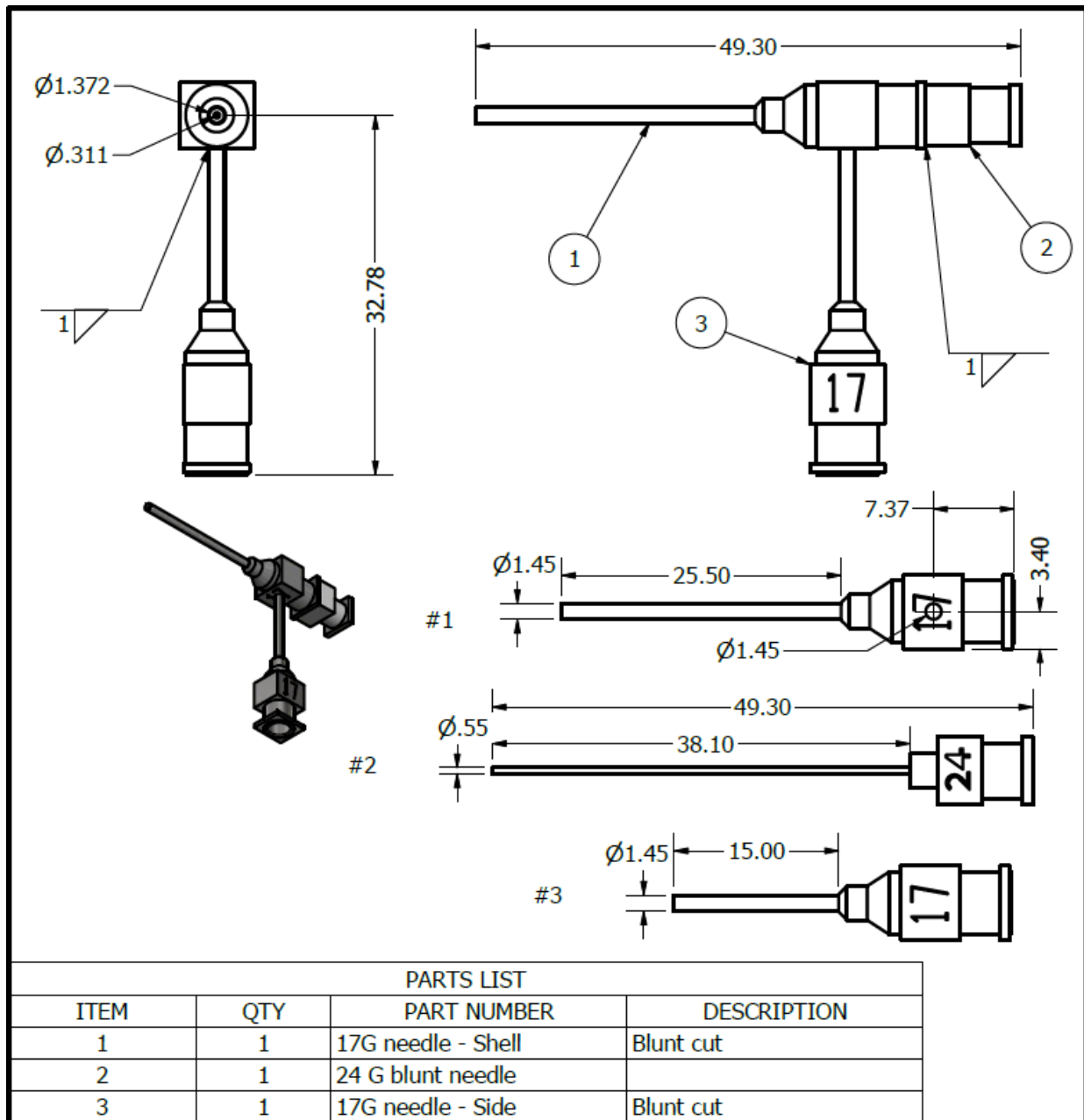
Figure 62: Coaxial needle design drawings

ITEM	QTY	PART NUMBER	DESCRIPTION
PARTS LIST			
1	1	17G needle - Shell	Blunt cut
2	1	24 G blunt needle	
3	1	17G needle - Side	Blunt cut

Appendix C   Coaxial electrospinning iterations

↑ – Increase, ↓ – Decrease

rH – relative humidity (%)

TCD – tip to collector distance (cm)

SS – rotational speed (RPM)

V+ – positive voltage (kV)

V- – negative voltage (kV)

Qs – shell solution flow rate (ml/h)

Qc – core solution flow rate (ml/h)

MW – molecular weight

Solutions

Shell A = 20 % DP30/CHCl₃ wt/wt

Shell B = 22 % DP30/CHCl₃ wt/wt

Core A = 1 % HepNa⁺ / 4% PEO (400kDa)/ DI water: EtOH (60:40) wt/wt

Core B = 0.5 % Hep Na⁺ / 4 % PEO (900kDa)/ DI water wt/wt

Core C = 24 % HepNa⁺ / 4% PEO(400kDa)/ DI water: EtOH (60:40) wt/wt

Core D = 27.5 % HepNa⁺ / 3.5% PEO(400kDa)/ DI water: EtOH (60:40) wt/wt

Core E = 38.5 % HepNa⁺ / 3.75% PEO(400kDa)/ DI water: EtOH (60:40) wt/wt

Table 18: Some highlights of the final coaxial electrospinning iterations illustrating the effect of major parameter changes in the attempt to incorporate more HepNa⁺ into scaffolds whilst maintaining a uniform, dry fibre structure.
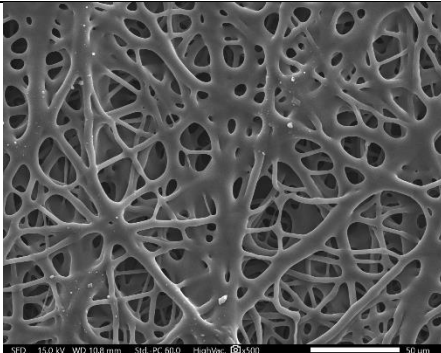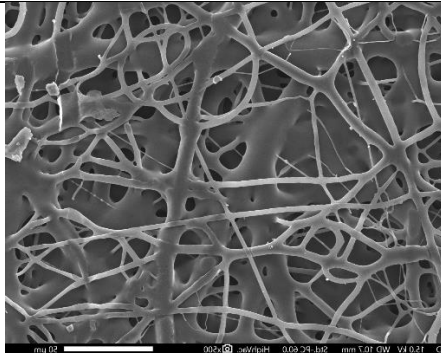
	x500 (abluminal)	x500 (luminal)	Investigated change	Parameters
i			n/a	rH = 35 TCD = 30 SS = 150 Qs = 2.8 Qc = 0.4 V+ = 14.0 V- = -4.0 Shell A Core A
ii			↓ rH ↑ TCD ↓ SS	rH = 33 TCD = 10 SS = 35 Qs = 2.8 Qc = 0.4 V+ = 13.0 V- = -5.0 Shell A Core A
iii			↑ SS	rH = 33 TCD = 35 SS = 25 Qs = 2.8 Qc = 0.4 V+ = 14.0 V- = -5.8 Shell A Core A
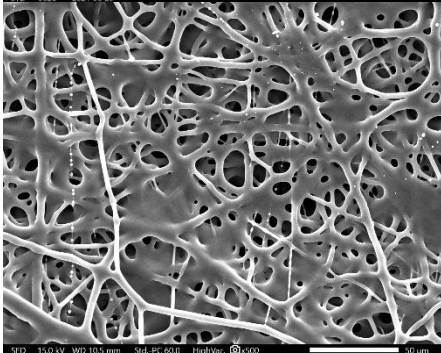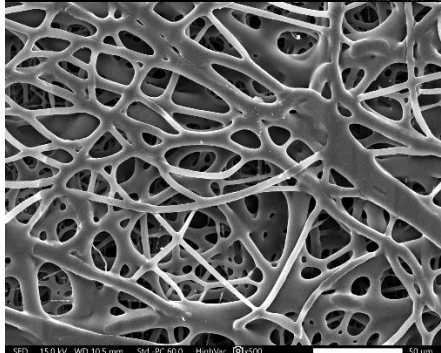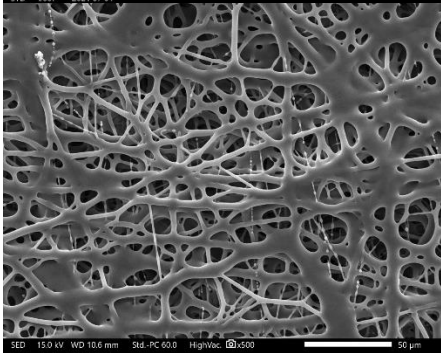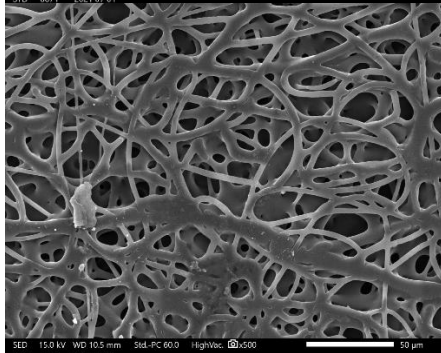
	x500 (abluminal)	x500 (luminal)	Investigated change	Parameters
iv			↑ TCD ↑ SS ↓ Qs	rH = 37 TCD = 40 SS = 40 Qs = 2.2 Qc = 0.4 V+ = 15.0 V- = -8.0 Shell A Core A
v			↑ Qs	rH = 30 TCD = 40 SS = 40 Qs = 3.0 Qc = 0.4 V+ = 14.8 V- = -9.0 Shell A Core A
vi			↓ TCD Different core (higher PEO MW)	rH = 30 TCD = 30 SS = 40 Qs = 2.0 Qc = 0.2 V+ = 11.0 V- = -11.0 Shell A Core B
vii			↑ TCD ↑ SS	rH = 32 TCD = 50 SS = 37 Qs = 2.0 Qc = 0.2 V+ = 12.8 V- = -2.5 Shell A Core B
viii			↓ V- Different core (return to lower MW PEO)	rH = 31 TCD = 41 SS = 40 Qs = 2.0 Qc = 0.4 V+ = 14.0 V- = -4.0 Shell A Core A
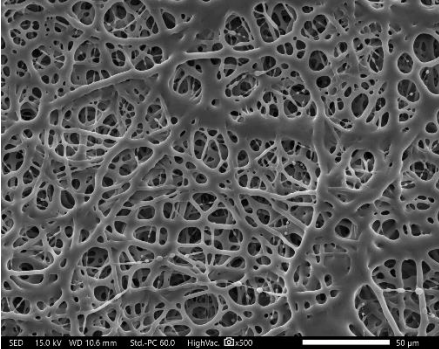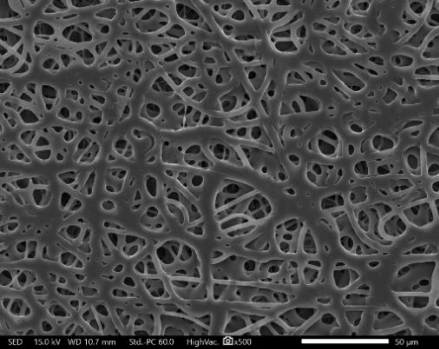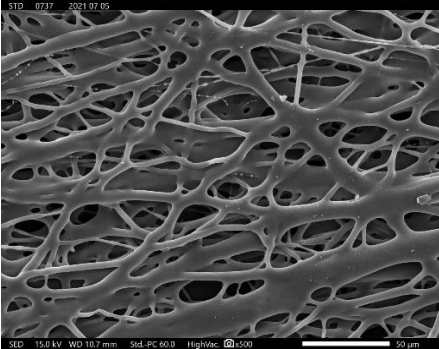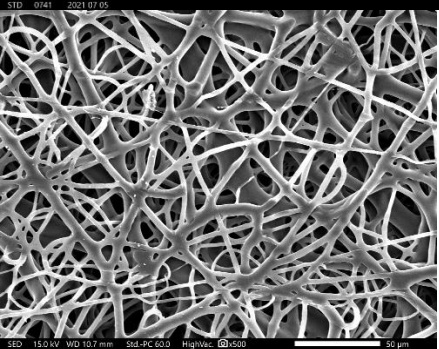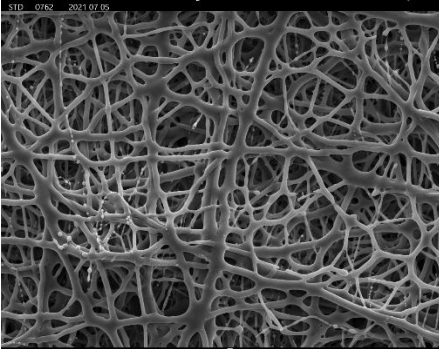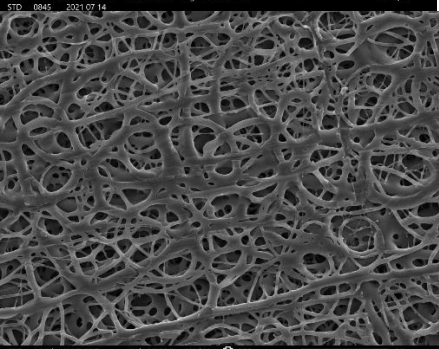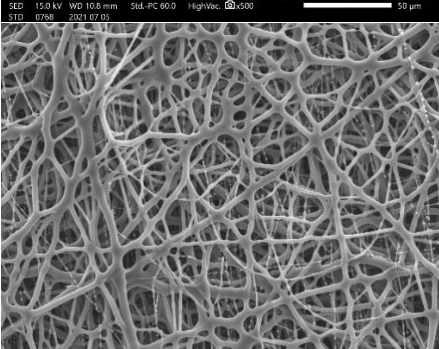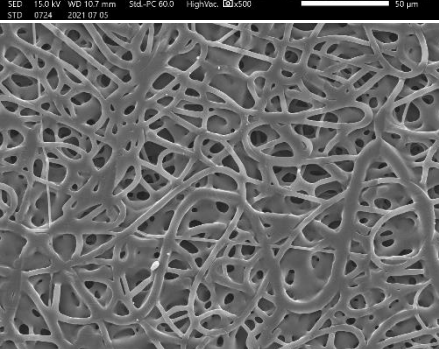
	x500 (abluminal)	x500 (luminal)	Investigated change	Parameters
ix			↑ TCD ↑ -V	rH = 30 TCD = 40 SS = 40 Qs = 2.0 Qc = 0.4 V+ = 14.0 V- = -6.0 Shell A Core A
x			Different core (↑ HepNa$^+$ conc.)	rH = 30 TCD = 40 SS = 40 Qs = 3.0 Qc = 0.3 V+ = 17.5 V- = -7.5 Shell A Core C
xi			Different core (↑ HepNa$^+$ conc. & ↓ PEO conc.)	rH = 33 TCD = 38 SS = 50 Qs = 2.2 Qc = 0.4 V+ = 16 V- = -6 Shell A Core D
xii			↓ TCD	rH = 32 TCD = 27 SS = 50 Qs = 1.8 Qc = 0.3 V+ = 16 V- = -0.5 Shell A Core D
xiii			Different shell (↑ DP30 conc.) ↑ TCD	rH = 32 TCD = 28 SS = 60 Qs = 2.2 Qc = 0.4 V+ = 16 V- = -2.5 Shell B Core D
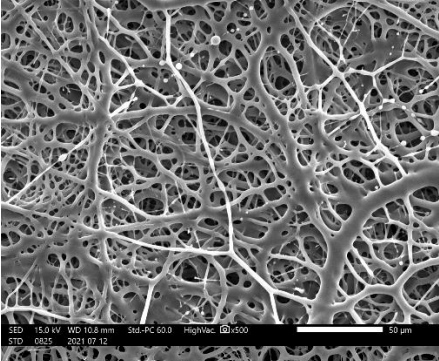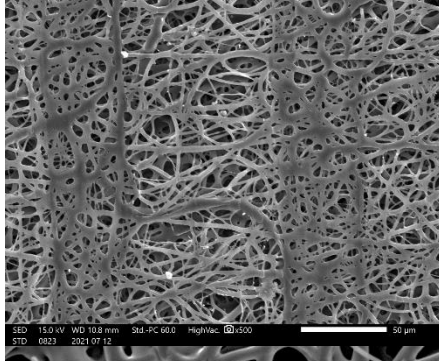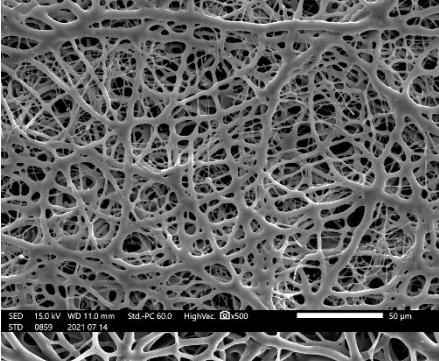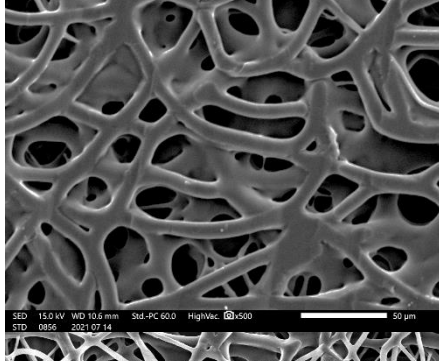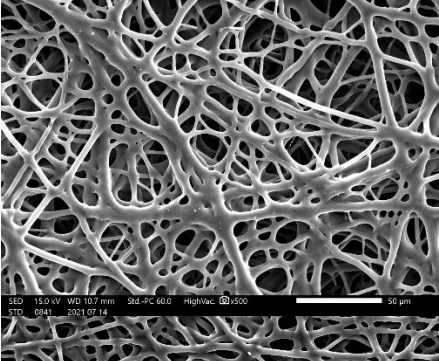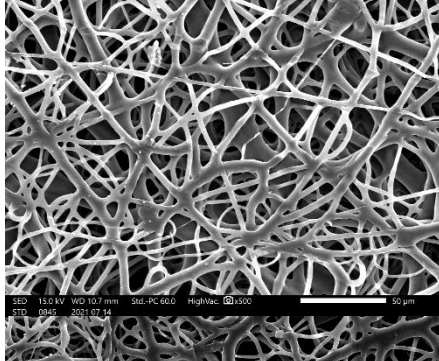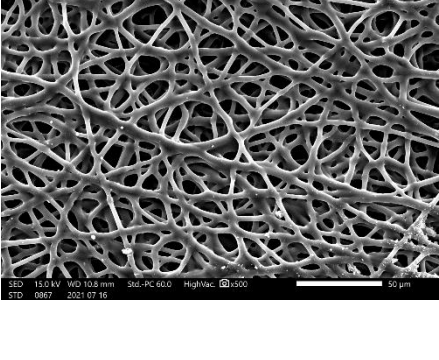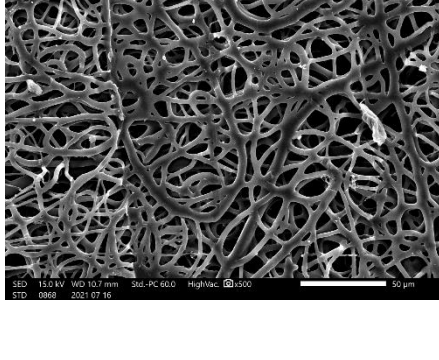
x500 (abluminal)	x500 (luminal)	Investigated change	Parameters
xiv		Different core (↑ HepNa⁺ conc. & ↑ PEO conc.)	rH = 33 TCD = 29 SS = 60 Qs = 2.2 Qc = 0.4 V+ = 16.5 V- = -3 Shell B Core E

Appendix D   Human ethics approval letter

UNIVERSITY OF CAPE TOWN

Faculty of Health Sciences

Human Research Ethics Committee

Room G50- Old Main Building
Groote Schuur Hospital
Observatory 7925
Telephone [021] 406 6492
Email: hrec-enquiries@uct.ac.za
Website: www.health.uct.ac.za/fhs/research/humanethics/forms

06 August 2021

HREC REF: 491/2021

Prof D Bezuidenhout
Cardiovascular Research Unit
Room 3.13 Chris Barnard Building-FHS
Email: Deon.bezuidenhout@uct.ac.za
Student: KRSGER006@myuct.ac.za

Dear Prof Bezuidenhout

PROJECT TITLE: HEPARIN ELUTING SCAFFOLDS FOR CARDIOVASCULAR APPLICATIONS-MASTERS CANDIDATE-MR GERHARD KRAUSE

Thank you for submitting your study to the Faculty of Health Sciences Human Research Ethics Committee (HREC) for review.

It is a pleasure to inform you that the HREC has **formally approved** the above-mentioned study, subject to adding the HREC contact details to the informed consent document and appropriate UCT permission to access staff and students.

This approval is subject to strict adherence to the HREC recommendations regarding research involving human participants during COVID -19, dated 17 March 2020; 06 July 2020 & 01 July 2021.

Approval is granted for one year until the 30 August 2022.

Please submit a progress form, using the standardised Annual Report Form if the study continues beyond the approval period. Please submit a Standard Closure form if the study is completed within the approval period.
(Forms can be found on our website: www.health.uct.ac.za/fhs/research/humanethics/forms)

The HREC acknowledge that the student: Mr Gerhard Krause will also be involved in this study.

Please quote the HREC REF 491/2021 in all your correspondence.

Please note that the ongoing ethical conduct of the study remains the responsibility of the principal investigator.

Please note that for all studies approved by the HREC, the principal investigator **must** obtain appropriate institutional approval, where necessary, before the research may occur.

Yours sincerely

PROFESSOR M BLOCKMAN
CHAIRPERSON, FACULTY OF HEALTH SCIENCES HUMAN RESEARCH ETHICS COMMITTEE
Federal Wide Assurance Number: FWA00001637.
Institutional Review Board (IRB) number: IRB00001938
NHREC-registration number: REC-210208-007

This serves to confirm that the University of Cape Town Human Research Ethics Committee complies to the Ethics Standards for Clinical Research with a new drug in patients, based on the Medical Research Council (MRC-SA), Food and Drug Administration (FDA-USA), International Council for Harmonisation of Technical Requirements for Pharmaceuticals for Human Use: Good Clinical Practice (ICH GCP), South African Good Clinical Practice Guidelines (DoH 2006), based on the Association of the British Pharmaceutical Industry Guidelines (ABPI), and Declaration of Helsinki (2013) guidelines. The Human Research Ethics Committee granting this approval is in compliance with the ICH Harmonised Tripartite Guidelines E6: Note for Guidance on Good Clinical Practice (CPMP/ICH/135/95) and FDA Code Federal Regulation Part 50, 56 and 312.

Appendix E   UCT staff access

HR194	**ACCESS TO UCT STAFF FOR RESEARCH PURPOSES**	**UNIVERSITY OF CAPE TOWN** IYUNIVESITHI YASEKAPA · UNIVERSITEIT VAN KAAPSTAD

NOTES
- Forms must be downloaded from the UCT website: http://www.uct.ac.za/depts/sapweb/forms/forms.htm
- This form must be completed by applicants who are requesting to access UCT staff for the purpose of research.
- A copy of the research proposal as well as the Ethics Committee approval must be attached.
- It is the responsibility of the researcher/s to apply for ethical clearance from the relevant Faculty's Research in Ethics Committee (RiEC).
- If you are requesting staff information, you are required to complete the HR Information Request Form (HR190) and submit it together with all the required documentation.
- The turnaround time for a reply is approximately **10 working days unless specified as urgent.**
- Return the completed application form and all the above documentation to Joy Henry via email: joy.henry@uct.ac.za; or deliver to: For the Attention: Executive Director, Human Resources Department, Bremner Building, Room 214, Lower Campus, UCT.

SECTION A: APPLICANT DETAILS

Title	Mr	Name	Gerhard Jaco Krause
Telephone number	0761555628	Email address	krsger006@myuct.ac.za
Student number	KRSGER006	Staff number	
Visiting researcher ID / passport number			
Faculty Officer contact details			
University or institution at which employed or a registered student		University of Cape Town	
Faculty or department in which you are registered or work		Faculty of Health Sciences	
Address (if not UCT)			

SECTION B. SUPERVISOR DETAILS

	Title and name	Telephone number	Email address
Supervisor	Prof Deon Bezuidenhout	0214066349	deon.bezuidenhout@uct.ac.za
Co-Supervisor			

SECTION C: APPLICANT'S FIELD OF STUDY (if applicable) / TITLE OF RESEARCH PROJECT / STUDY

Degree	MSc in Biomedical Engineering		
Research project or title	Heparin Eluting Scaffolds for Cardiovascular Applications		
Research proposal attached	☒ Yes	☐ No	
Target population (number of UCT staff)	10 (max)		
Amount of time required for an interview and/or questionnaire	5 minutes		
Lead Researcher details	Prof Deon Bezuidenhout (Principal Investigator)		
Proof of ethical clearance status attached	☒ Yes	☐ No	

SECTION D: FOR OFFICE USE (Approval status to be completed by the Executive Director, Human Resources or Nominee)

Support or approval			Role	Signature	Date
Supported?	☑ Yes	☐ No	Zoe Cosmopoulos (Specialist: HR Analytics)		10/08/2021
Approved?	☑ Yes	☐ No	Naeema Brey (Director: HR Analytics, Risk, Systems, Payroll & Administration)		13 August 2021

Appendix F   GSH institutional approval letter

Western Cape Government — Health

GROOTE SCHUUR HOSPITAL
Enquiries: Dr Bernadette Eick
e-mail: GSHReserach.Request@westerncape.gov.za

Professor Deon Bezuidenhout
CARDIOVASCULAR RESEARCH UNIT

E-mail: deon.bezuidenhout@uct.ac.za

Dear Professor Bezuidenhout,

RESEARCH PROJECT: Heparin Eluting Scaffolds For Cardiovascular Applications (Masters – Mr Gerhard Krause)

Your recent letter to the hospital refers.

You are granted permission to proceed with your research, which is valid until 30 August 2022.

Please note the following:

a) Your research may not interfere with normal patient care.
b) Hospital staff may not be asked to assist with the research.
c) Confidentiality must always be maintained.
d) No additional costs to the hospital should be incurred as indicated in your Annexure 2 i.e. Lab, consumables or stationery. If access to TRACK Care/NHLS is required, kindly attach our letter of approval to the application form and approach Information Management to assist with data.
e) No patient folders may be removed from the premises or be inaccessible.
f) Please provide the research assistant/field worker with a copy of this letter as verification of approval.
g) Should you at any time require photographs of your subjects, please obtain the necessary indemnity forms from our Public Relations Office (E45 OMB or ext. 2187/2188).
h) Should you require additional research time beyond the stipulated expiry date, please apply for an extension.
i) Please discuss the study with the HOD before commencing.
j) Please introduce yourself to the person in charge of an area before commencing.
k) On completion of your research, please forward any recommendations/findings that can be beneficial to use to take further action that may inform redevelopment of future policy / review guidelines.
l) Please contact Michelle Riley (Patient Fees) at ext. 2276 to ascertain if there will be charges for conducting the Research and to obtain a quote or to discuss charges
m) Kindly submit a copy of the publication or report to this office on completion of the research.
n) At no time should any posters encouraging patients to partake in research, be displayed within a clinical area.
o) Please adhere to ALL COVID-19 regulations and Groote Schuur Hospital policies.

I would like to wish you every success with the project.

Yours sincerely

DR BERNADETTE EICK
CHIEF OPERATIONAL OFFICER
Date: 9 September 2021

C.C. Mr. L. Naidoo / Dr. S. Peter / Mr A. Mohamed / Professor J. Swanevelder

C-46 Management Suite, Old Main Building,
Observatory 7925
Tel: +27 21 404 6288   fax: +27 21 404 6125

Private Bag X,
Observatory, 7935
www.westerncape.gov.za/health

Appendix G   MATLAB script for interpolating strains from stress-strain curves

```matlab
r_o = 1.645;
r_i = 1.315;
t = r_o - r_i;
Pd = 80/7500.62;
Ps = 120/7500.62;

o_hoop_d_thick = Pd*((r_o^2)+(r_i^2))/((r_o^2)-(r_i^2));
o_hoop_s_thick = Ps*((r_o^2)+(r_i^2))/((r_o^2)-(r_i^2));

o_hoop_d_thin = Pd*r_o/t;
o_hoop_s_thin = Ps*r_o/t;

a = table2array(ComplianceNS9(1:270, 8));
b = table2array(ComplianceNS9(1:270, 7));

x = transpose(a);
y = transpose(b);

y2 = [o_hoop_d_thick, o_hoop_s_thick];
 %y2 = [o_hoop_d_thin, o_hoop_s_thin];

x2 = interp1(y, x, y2, 'linear')
Compliance = 10000*(0.01*(x2(2)-x2(1)))/((120-80)*((0.01*x2(1))+1))

figure(1)
plot(x, y, '-g')
hold on
plot(x2, y2, 'bp')
hold off
grid
legend('Data', 'Interpolated Points', 'Location', 'NW')
```

Appendix H   TEG results